

The Title of your PhD Thesis about the Molecular Outflow of SVS 13

PhD dissertation by
Guillermo Blázquez Calero

Instituto de Astrofísica de Andalucía (IAA-CSIC)

Programa de Doctorado en Física y Matemáticas (FisyMat)
Universidad de Granada

A thesis submitted in fulfillment
of the requirements of the degree of
Doctor of Philosophy

March 14, 2024

PhD thesis supervised by
Dr. Guillem Anglada
Dra. Mayra Osorio



INSTITUTO DE
ASTROFÍSICA DE
ANDALUCÍA



EXCELENCIA
SEVERO
OCHOA



UNIVERSIDAD
DE GRANADA

ACKNOWLEDGEMENTS

Agradecimientos

RESUMEN

Resumen de la tesis

SUMMARY

Summary of the thesis

CONTENTS

1	Introduction	1
1.1	The formation of stars	1
1.1.1	The birthplaces of stars: From molecular clouds to dense cores	1
1.1.2	The formation of a low-mass star	2
1.1.3	Classification and evolution of Young Stellar Objects	5
1.1.4	Multiplicity in star formation	5
1.1.5	Signatures of variable accretion in Young Stellar Objects	6
1.2	Outflow manifestations of Young Stellar Objects	7
1.2.1	A brief historical review	7
1.2.2	Molecular outflows	8
1.2.3	Jets	10
1.2.3.1	Radio jets	11
1.2.3.2	Molecular jets and bullets	11
1.3	Motivation of our work	11
2	Re50 radio jet	15
2.1	Introduction	15
2.2	Observations	15
2.3	Results	15
2.4	Analysis and discussion	15
2.5	Summary and conclusions	15
3	The SVS 13 system	17
3.1	The SVS 13 protobinary	17
3.2	Two circumstellar disks and a circumbinary	17
3.3	The SVS 13 outflow	17
4	ALMA observations of SVS 13 outflow	19
4.1	Introduction	19
4.2	Observations and data reduction	19
4.3	Results	21
4.3.1	Description of the molecular outflow	21
4.3.2	Substructure of the molecular jet	21

4.3.3	Families of rings	26
4.4	Analysis and discussion	26
4.4.1	Identification of the observed line emission as CO at EHV	26
4.4.2	Inclination angle	32
4.4.3	Dynamical times of the heads of the ring families	32
4.4.4	Association of a molecular bullet with an optical/infrared outburst	33
4.4.5	Excitation temperature	33
4.4.6	Column densities	34
4.4.7	Masses	36
4.5	Summary and conclusions	37
5	Modelization of SVS 13 molecular jet	39
5.1	Introduction	39
5.2	Analytical ballistic paraboloid model	39
5.2.1	Model parameters	39
5.2.2	Channel maps	42
5.2.3	Derivation of shell parameters from the observation	44
5.2.4	Application to SVS 13	46
5.3	Ballistic deprojection	46
5.3.1	Mass loss rate in the ballistic model.	49
5.4	Bowshock model	51
5.4.1	Derivation of the density of the ambient gas and mass rates	53
5.4.2	Calculation of the emission of the channel maps	58
5.5	Opacity and ring asymmetry	61
6	Summary and conclusions	67
6.1	Future work	67
A	SVS 13 channel maps from ALMA observations	69
B	Calculation of model spectral cubes	71
C	Determination of flux density at the central frequency of a band	73
List of Figures		75
List of Tables		77

CHAPTER 1

INTRODUCTION

1.1 The formation of stars

In this section we review our current understanding of the process by which gas turns into solar-like stars.

1.1.1 The birthplaces of stars: From molecular clouds to dense cores

Stars are formed within molecular clouds, which are the coldest ($T \approx 10\text{-}30$ K) and the densest ($n \approx 10^2\text{-}10^5$ cm $^{-3}$) regions of the interstellar medium (ISM), composed by a mixture of molecular gas and dust. The molecular gas is responsible of about 99 percent of the total mass of the molecular cloud, and its predominantly composed of H₂. Since H₂ molecules are not capable of emitting at low temperatures, other molecules are used as a proxy for H₂; most importantly, CO, but also other bright molecules as HCN, HCO+, CS, or HNC. The remaining ~ 1 percent of the mass of molecular clouds is attributed to dust grains, which are responsible of the high extinction at optical wavelengths; for this reason, molecular clouds in the solar neighbourhood ($\lesssim 500$ pc) that are seen in silhouette against the background Galactic starlight are called “dark clouds” (Bergin & Tafalla, 2007). Without the presence of dust, molecular clouds would cease to exist, as it protects the molecules from being dissociated by the interstellar UV radiation.

Molecular clouds occupy a small fraction of the volume of the ISM in the Galaxy. Their sizes range from $\sim 2\text{-}100$ pc, with masses $\sim 10^2\text{-}10^6 M_{\odot}$ (Williams et al., 2000; Steven W. Stahler, 2004; Bergin & Tafalla, 2007; McKee & Ostriker, 2007; Hennebelle & Falgarone, 2012). In the Milky Way, it is estimated that 80 percent of the molecular hydrogen is found in the largest (10-100 pc) and most massive ($\sim 10^4\text{-}10^6 M_{\odot}$) molecular clouds called Giant Molecular Clouds (GMCs), where most of the star formation take place (Dobbs et al., 2014; Chevance et al., 2023). Some prototypical examples of GMCs found in the Galaxy are Orion or Perseus clouds.

The internal structure of GMCs presents a complex network of clumps and filaments, the latter being a characteristic of self-gravitating turbulent gas (André et al., 2014). It is estimated that ~ 15 percent of the total mass of molecular clouds are in the form of filamen-

tary structures, whereas filaments host the \sim 60-90 percent of the dense (column densities $N(H_2) > 7 \times 10^{21} \text{ cm}^{-2}$) gas mass (Pineda et al., 2023). They are present in a very wide range of sizes of 0.1-100 pc and masses of $1-10^5 M_\odot$, and show a self-similar hierarchical structure; i.e., filaments may break down into smaller and smaller filaments (Vázquez-Semadeni et al., 2019; Hacar et al., 2023). Filaments are not in equilibrium and are highly dynamical, with accretion flows onto and along them, playing an important role in funneling the gas from the extended cloud to the clumpy overdensities where the physical conditions for the formation of a star are met (e.g. Gómez & Vázquez-Semadeni, 2014).

Filaments may fragment into prestellar cores, gravitationally bound dense clouds with typical sizes of 0.03-0.2 pc, densities of $10^4-10^5 \text{ cm}^{-3}$, and masses of $0.5-5 M_\odot$, which are the precursors of single low-mass ($M_* < 8 M_\odot$) stars or simple stellar systems. The most massive substructures in GMCs, the so-called ridges (high-density filaments, with $n > 10^5 M_\odot$ over $\sim 5 \text{ pc}^3$) and hubs (parsec-size central clumps with several hundreds of M_\odot fed by filaments), are associated with the progenitors of star clusters and high-mass ($M_* > 8 M_\odot$) stars (Motte et al., 2018). As an example, in Fig. 1.1 we show a column density map of the NGC 1333 ridge, which is associated to a young proto-cluster where low-mass stars are forming (Hacar et al., 2017).

Completar: Star formation is relatively an inefficient process: on the cloud scale, only $\sim 5\%$ of the gas is converted into the stars; on the prestellar core scale, the star formation efficiency is about to $\sim 30\% - 50\%$ (Offner et al., 2014; Chevance et al., 2023).

1.1.2 The formation of a low-mass star

As described in the previous section, low-mass stars form through the collapse of prestellar cores, gravitationally bound dense fragments of filaments within the molecular clouds. For a core to undergo gravitational collapse, self-gravity should overcome the opposing internal gas pressure and, secondarily, the opposing forces due to magnetic field and turbulence.

In an infinite sized cloud with no magnetic fields, turbulence nor rotation, Jeans (1902) showed that short-wavelength density perturbations propagates as sound waves that dissipate, but those perturbations that exceed the ‘Jeans length’, λ_J , are gravity dominated and grow exponentially. For a isothermal uniform medium of density ρ_0 and temperature T , $\lambda_J = \pi^{1/2} c (G\rho_0)^{-1/2}$, where $c = (kT/m)^{1/2}$ is the sound speed, being m the average particle mass. This imposes a minimum mass for the gravitational collapse; i.e., the ‘Jeans mass’; for a uniform sphere is $M_J = \pi/6\rho_0\lambda_J^3$.

The first numerical calculations of the gravitational collapse was performed by Larson (1969), that considered a spherically symmetric cloud without taking into account magnetic fields, turbulence, and rotation. For the typical mean properties of cores (with masses of $\sim 1 M_\odot$ and sizes of $\sim 0.1 \text{ pc}$), the collapse can be divided in four phases (Larson, 2003; Estalella & Anglada, 2008; Schulz, 2012):

- Free-fall phase: Density increases isothermally (up to $10^{-13} \text{ g cm}^{-3}$ in the center) and matter falls in on a free-fall timescale. Ignoring pressure gradients, the time needed for the collapse of a uniform sphere of gas is the free-fall time $t_{\text{ff}} = (3\pi/(32G\rho))^{1/2}$,

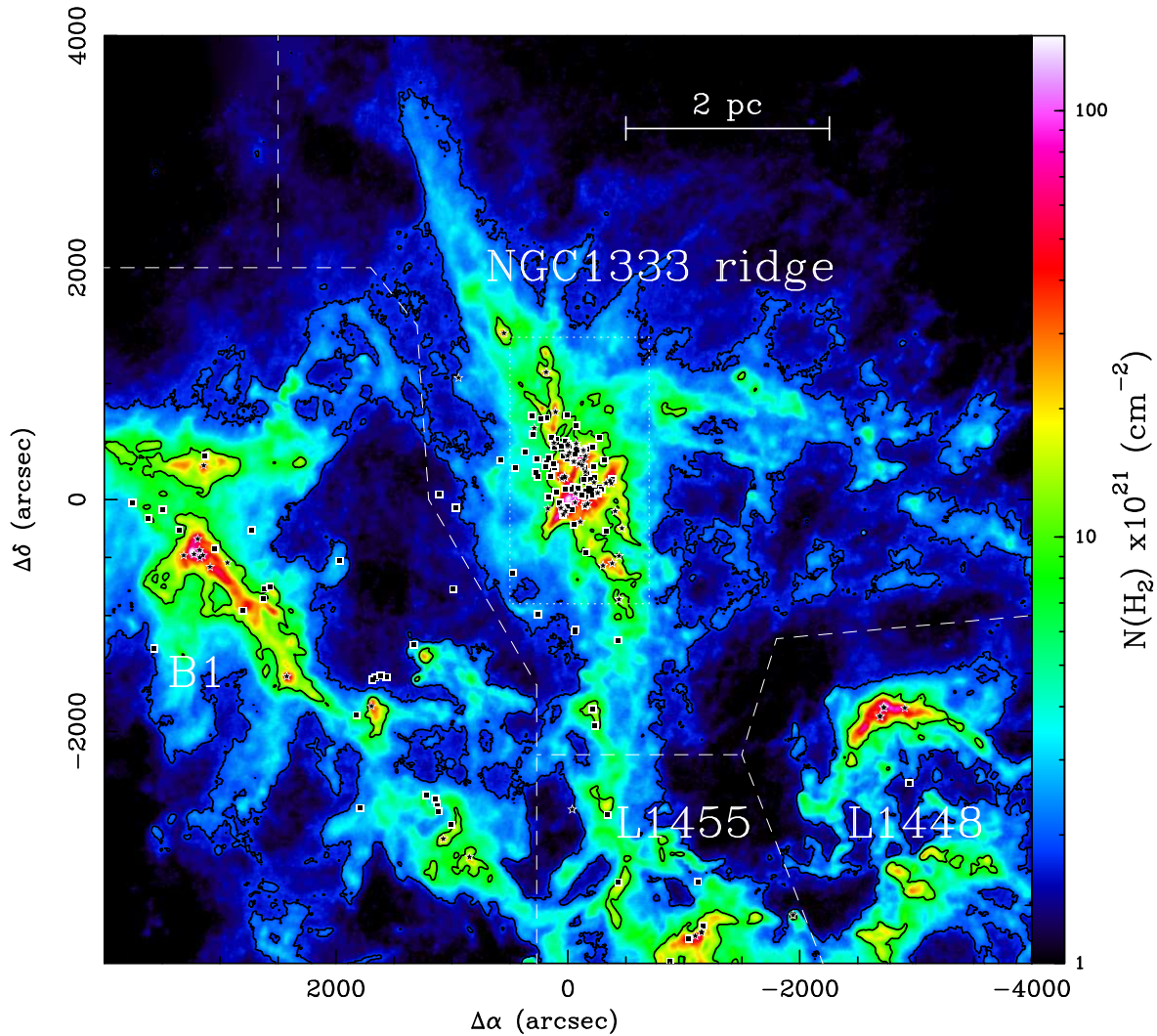


Figure 1.1 Column density map of the NGC 1333 ridge in Perseus, derived using Herschel-Planck maps (taken from Hacar et al., 2017). Offset coordinates are relative to the position RA(J2000)= $03^{\text{h}}29^{\text{m}}08^{\text{s}}.9$, Dec(J2000)= $31^{\circ}15'12''$. The squares and stars symbols represent the positions of the Class 0/I and Flat/ClassII/ClassIII objects, respectively (for more information, see Hacar et al., 2017).

with a density distribution of the form $\rho \propto r^{-2}$.

- First core phase: Central density increases ($> 10^{-13} \text{ g cm}^{-3}$) and some inner layers become optically thick, so the collapse is not isothermal and the contraction is adiabatic. The internal temperature and pressure increases, so the core of a few au and $\sim 0.01 M_{\odot}$ becomes stable; this is the First Hydrostatic Stellar Core, that continues to accrete mass through an accretion shock developed in its surface.
- Opacity phase: Hydrogen molecules start to dissociate as internal temperature reaches

2000 K. Since this process is highly endothermic, the internal pressure gradient is not able to be enough to counter gravity, so this causes a second collapse. When density further increases to $10^{-2} \text{ g cm}^{-3}$ as well as the ionization fraction of the hydrogen. Finally the collapse is permanently halted and a second hydrostatic core about $\sim 0.001 M_{\odot}$ and radius $\sim 1 R_{\odot}$ is formed: this is the ‘embryo’ of the protostar.

- Accretion phase: The second core mass grows rapidly and, within a brief time, the mass of the first core falls into the second core. The main accretion phase starts and now the observations indicate the existence of a protostar.

When rotation is taken into account (Bate, 1998), these collapse phases are still valid, predicting the formation of a second hydrostatic core with similar properties. However, the remaining matter has a significant angular momentum, and an accretion disk will be formed around the protostar. Thus, accretion onto the star is disk mediated (Hartmann et al., 2016). Accretion is intimately related to ejection phenomena, powerful collimated jets and winds along the rotation axis (see Fig. 1.2). This ejections, that are thought to be driven by magnetocentrifugal forces from the disks, play an important role in removing angular momentum, allowing the star to reach its final mass (e.g. Pudritz & Ray, 2019). Observations indicate that these jets and winds are accretion-powered ejections, since mass loss rates strongly correlate with accretion luminosity (Cabrit et al., 1990; Hartigan et al., 1995; Cabrit, 2007; Ellerbroek et al., 2013; Natta et al., 2014; Lee, 2020).

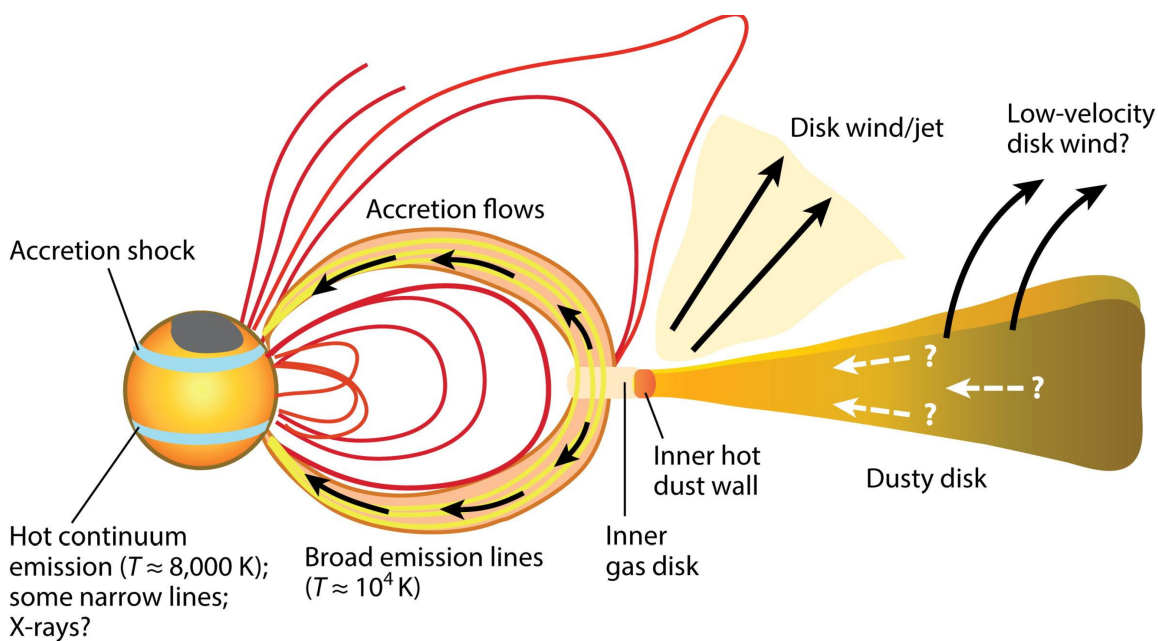


Figure 1.2 Taken from Hartmann et al. (2016)

1.1.3 Classification and evolution of Young Stellar Objects

The evolution of an isolated low-mass Young Stellar Object (YSO) has been traditionally characterized from the shape of the spectral energy distribution (SED), using the IR spectral index between 2.2 and 100 μm (Andre et al., 2000; Dunham et al., 2014):

$$\alpha_{\text{IR}} = \frac{d \log \lambda F_\lambda}{d \log \lambda} \quad (1.1)$$

- Class 0: Protostars in this phase are highly embedded in a cold ($T = 10\text{-}30$ K) and dusty envelope (Andre et al., 2000). Consequently, this type of objects are extremely faint in the optical and near-IR, and are submillimeter sources. The SED resembles to a cold black body, characteristic of the natal cold envelope, which still contains most of the final mass. An accretion disk is already formed, with a mass of $\sim 10\%$ of the mass of the envelope. Accretion processes are high, which is accompanied by powerfull outflow phenomena. These are the youngest YSOs, with ages $\lesssim 10^4$ yr.
- Class I: This protostars are still embedded in the envelope, but most of the mass is contained in the circumstellar disk and the protostar. Thus, this objects are detected in the near infrared, but are not optically visible, and they are characterized by $0 < \alpha_{\text{IR}} \leq 3$. Although still associated with outflow phenomena, since accretion is less important, they are less powerful than Class 0 objects. The age of these objects ranges between $\sim 10^4\text{-}10^5$.
- Class II: These YSO are no longer in the protostellar phase, and are regarded as pre-main-sequence stars. The enveloped is almost cleared out, and are characterized by $-2 < \alpha_{\text{IR}} \leq 0$. Consequently, they can be detected in the optical and in the infrared; they are classical T Tauri stars. Disks can clearly be observed in the submillimeter weavelengths, which presents rings and gaps; the signatures of forming planets. Their ages ranges between $\sim 10^5\text{-}10^6$ yr.
- Class III: At these phases, the disk is almost cleared out, which can host recently formed planets, and there is almost no further accretion to the protostar. Thus, accretion and ejection processes are negligible. The SED resembles to one of a black body at a high temperature, characteristic of the photosphere of the star. The IR spectral index is in the range of $-3 < \alpha_{\text{IR}} \leq -2$. Their ages ranges between $\sim 10^6\text{-}10^7$ yr.

1.1.4 Multiplicity in star formation

Multiplicity: fragmentation of a turbulent core, disk fragmentation. Filament fragmentation, core fragmentation, disk fragmentation, and capture (Offner et al., 2023).

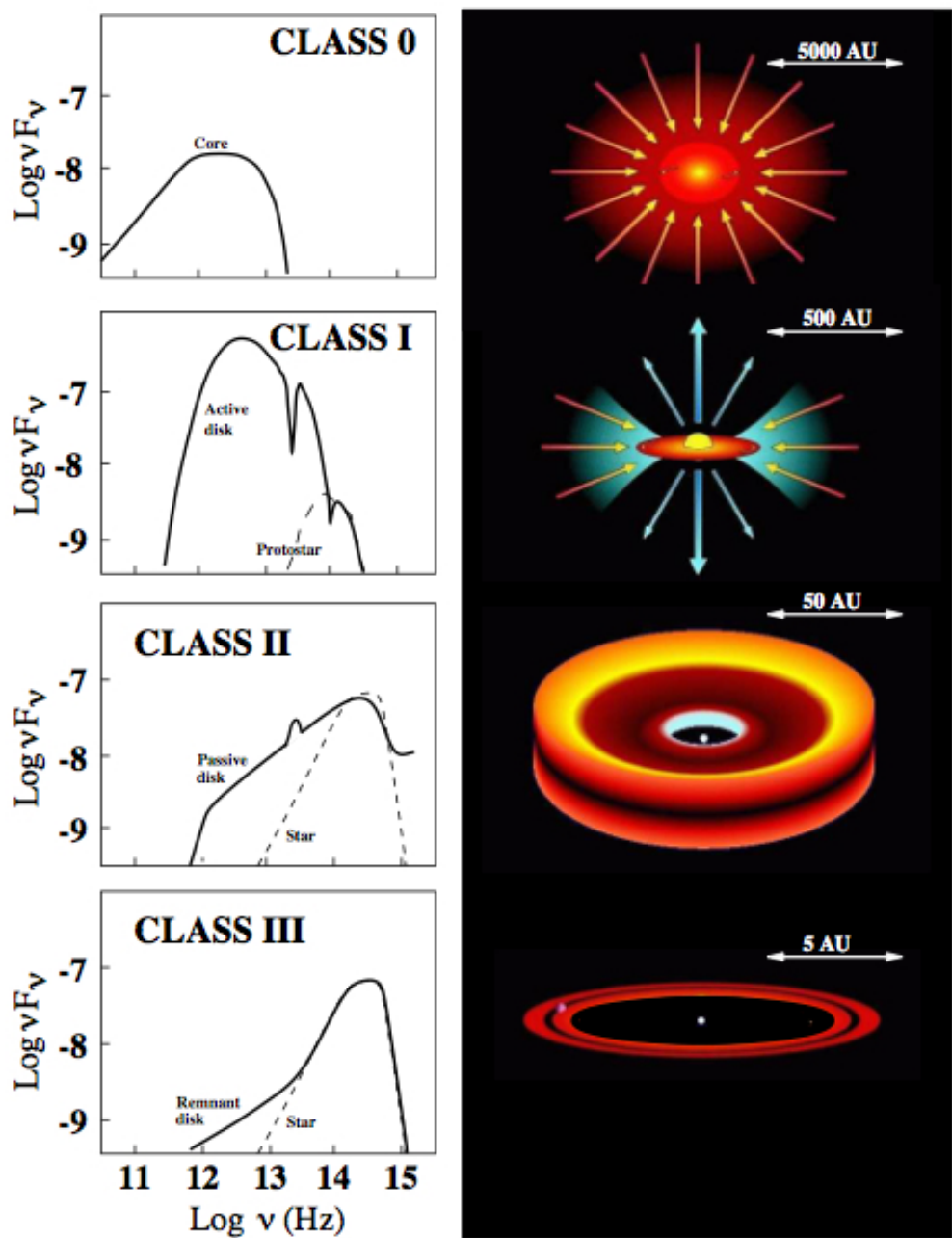


Figure 1.3 Scheme of the classification and evolutionary stages of an isolated YSO.

1.1.5 Signatures of variable accretion in Young Stellar Objects

(Fischer et al., 2023), (Audard et al., 2014)

1.2 Outflow manifestations of Young Stellar Objects

Outflows are an ubiquitous ingredient of the star formation process. Moreover, they are not a mere by-product of the protostar evolution, but they play an important role in the assembly of stars, can alter the properties of the protoplanetary disks and, consequently, they might be able to have an impact also on the planet formation process Frank et al. (2014). Also, comment the role at molecular cloud scale.

1.2.1 A brief historical review

It was not until about 1980 that there was sufficient observational evidence to show that star formation was accompanied by powerful ejections, which were unanticipated by theorists. Thus, the star formation paradigm changed from a infall only scenario into one in which outflow phenomena was a fundamental aspect.

The discovery of outflows from YSOs can be traced back to the first observations the Herbig-Haro (HH) objects, which were independently discovered by George Herbig (Herbig, 1951, 1952) and Guillermo Haro (Haro, 1952). HH objects are nebulae with a size of 20-30'', often found in pairs or strings, detected in the optical, dominated by hydrogen Balmer emission lines and other lines as [O II], [S II], or [FeII] (Schwartz, 1983; Reipurth & Heathcote, 1997; Reipurth & Bally, 2001). Although it was clear that HH objects were related with some aspect of star formation, they were initially interpreted to be nebulae where the formation of a star was taking place (Herbig, 1969). The shock nature of the HH objects was revealed by Schwartz (1975) who, based on the similarity between the HH spectra and the ones of the knots in supernova remnants, suggested that HH objects resulted from the interaction of YSO ejections with the ambient gas. Interestingly, with the development of infrared astronomy in the 1970s, it became clear that the driving sources of the ejections were not located in the nebulae, but the sources appeared at some distance. The interpretation that HH objects resulted from powerful ejections from the protostar was further supported when large proper motion (corresponding to tangencial velocities of $> 100 \text{ km s}^{-1}$) of HH objects were measured (Cudworth & Herbig, 1979; Herbig & Jones, 1981; Jones, 1983).

The first molecular outflow associated to a protostar was dicscovered in CO in the molecular cloud L1551 (Snell et al., 1980) with the Millimeter Wave Observatory (MWO). The emission was bipolar, poorly collimated, with a size of 0.5 pc and velocities of $\sim 15 \text{ km s}^{-1}$, with the presence of two HH objects in the blue lobe. Snell et al. (1980) proposed that the bipolar molecular outflow was material from the stratified molecular environment that was being swept-up by an initially isotropic wind.

In the early 1980, the widespread use of CCD in astronomy allowed much deeper images than photographic plates. From observations with the 2.2 m telescope of the Calar Alto Observator, Mundt & Fried (1983) reported four optical highly-collimated emission (jets), emanating from young stellar objects, with observed velocities $> 100 \text{ km s}^{-1}$, some times connected to HH objects. Thus, it was interpreted that the HH knots were parts of these jets where the interaction with the surrounding medium was taking place.

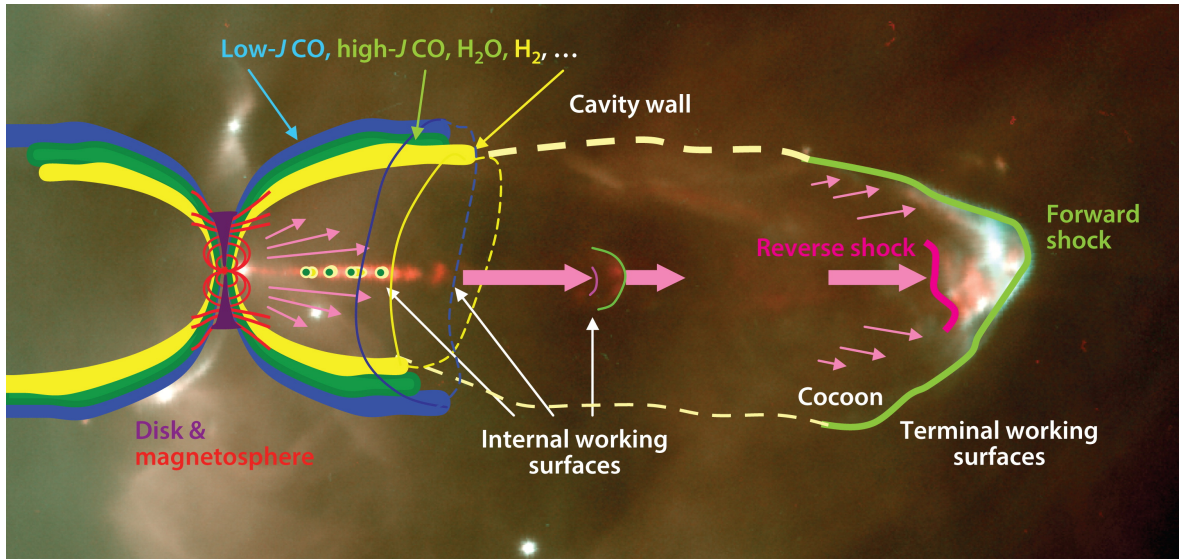


Figure 1.4 Taken from Bally (2016)

Typically, ejections from protostars have been observed as jets and molecular outflows:

- Jets are high collimated structures of gas traveling at velocities of the order of $100\text{--}1000 \text{ km s}^{-1}$. are thought to be launched through magnetohydrodynamic (MHD) mechanisms in the rotating star-disk system. Usually traced in the optical, infrared. Also in the cm, radio jets. The youngest sources have also a molecular component, traced in CO and other molecules in the mm. Usually called “molecular jets”. Molecular bullets.
- Molecular outflows are less collimated than jets, with velocities of $\sim 10 \text{ km s}^{-1}$. Ubiquitously observed in CO and other molecules in the mm. Bipolar. The classical picture is that they consist of gas entrained by a jet or a wide-angle wind. Nevertheless, ALMA is detecting small-scale molecular outflows ($\leq 2000\text{--}20000 \text{ au}$). Rotation. They are thought to be MHD-winds, so they are sometimes called “molecular winds”, to be distinguished from the classical bipolar molecular outflows of swept-up ambient gas at larger scales.

1.2.2 Molecular outflows

Properties (e.g. Lada, 1985; Cabrit et al., 1997; Bally, 2007; Arce et al., 2007; Bally, 2016). Scales. Tracers. Velocities. Hubble-law (Lada & Fich, 1996). Dynamical times? Evolution with source spectral class. Mass law with velocity as $dM/dv \propto v^{-\gamma}$. Large masses: the material can not originate from the YSO, and must consist primarily of ambient material swep-up by a momentum flux emanating from the YSO. Also, they can not be driven by

radiation pressure since the momentum in outflows is several orders of magnitude greater than that which can be supplied by radiation pressure from YSO (Bally & Lada, 1983). Large-scale molecular outflows can be driven by jets or wide-angle winds (Lee et al., 2000, 2001; Arce et al., 2007).

Jet-driven: Description of the jet-driven model. (semi)-analytic models (Raga & Cabrit, 1993; Masson & Chernin, 1993; Ostriker et al., 2001), simulations (Chernin et al., 1994; Smith et al., 1997; Suttner et al., 1997; Downes & Ray, 1999; Downes & Cabrit, 2007; Rabenahary et al., 2022). The collimated jet propagates and interacts with the environment, and a two shock structure (called “working surface”) is created: one shock inside the jet, the “jet shock” (or Mach disk), formed as the fast jet material impacts the slower previously shocked material; and the other shock in the environment, the “bow shock”, formed as the shocked material impacts the quiescent ambient material (Hollenbach, 1997; Raga et al., 2021). Due to the high thermal pressure between the shocks, the material in the jet beam is expelled sideways through the working surface, interacts with the ambient and a swept-up shell is formed surrounding the jet.

The total momentum delivered by jets appears to be consistent with that measured in the associated CO outflows (Hartigan et al., 1994; Eisloffel & Mundt, 1997)

Wide-angle wind-driven: The outflow is produced by a radially expanding wide-angle wind that is sweeping up the surrounding ambient material (Shu et al., 1991, 2000). Extended by (Li & Shu, 1996; Matzner & McKee, 1999). In this scenario, outflows are a purely momentum-driven phenomenon. The angular distribution of the ambient density and wind density, produce a shell geometry that have been compared with molecular outflows. In the “unified model” proposed by Shang et al. (2006), the jet is the central core of a wide-angle wind whose density decreases away from the axis (see also (Shang et al., 2020, 2023)).

Molecular winds New result from submm interferometers, particularly ALMA. Properties. The rotating flow is confined inside of the main swept-up outflow cavity walls. (Pascucci et al., 2023, Review): Scales (≤ 2000 au). Morphology: conical or parabolic shapes, semi-opening angles 10-40°. Tracers. Velocities. Dynamical times? Masses. Rotation, why is important and quantify. They are thought to trace matter directly ejected from the disk by thermal or magnetic processes. Consistent with launching radii XX-XX au. Examples: Class 0: HH212 (Tabone et al., 2017; Lee et al., 2018b; Tabone et al., 2020; Lee et al., 2021), HH211 (Lee et al., 2018a), NGC1333-IRAS4C (Zhang et al., 2018). Class I: CB26 (Launhardt et al., 2009, 2023; López-Vázquez et al., 2023), TMC1A (Bjerkeli et al., 2016), DGTauB (Zapata et al., 2015; de Valon et al., 2020; Garufi et al., 2020; de Valon et al., 2022); Class II: HH30 (Louvet et al., 2018), HD 163296 (Booth et al., 2021).

And also high-mass YSOs: Orion Source I (Hirota et al., 2017; López-Vázquez et al., 2020).

Fig 2 from Pascucci 2023?

free-free emission is produced in the ionized medium where free electrons are slowed down, releasing photons at radio wavelengths with typical spectral index of 0.5. non-thermal, gyrosynchrotron radiation ($\alpha < -0.1$ at > 4 cm)

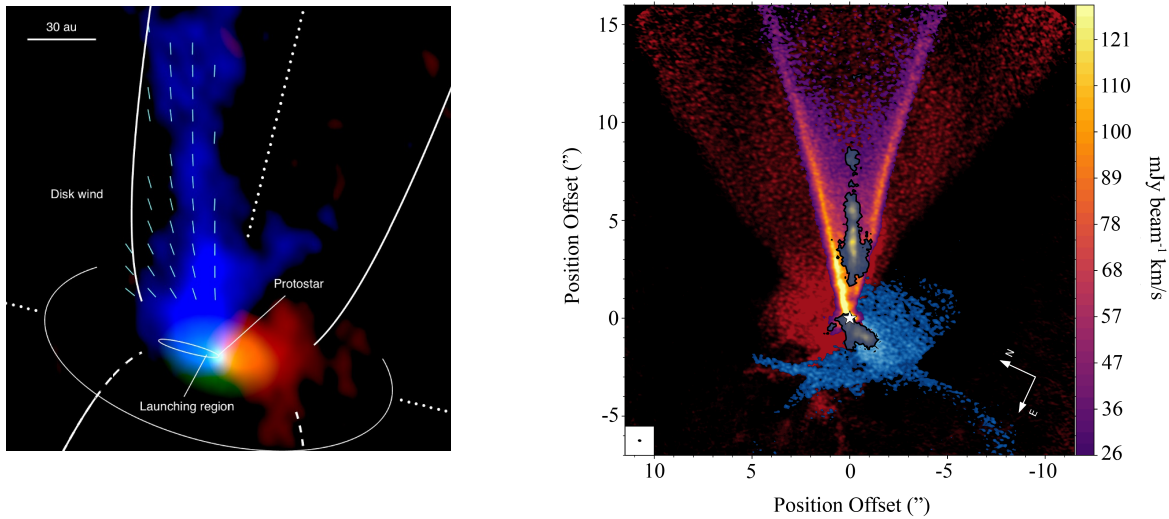


Figure 1.5 Left: Bjerkeli et al. (2016). Right: de Valon et al. (2020); Pascucci et al. (2023)

1.2.3 Jets

Jet observational properties (Reipurth & Bally, 2001; Frank et al., 2014; Anglada et al., 2018; Ray & Ferreira, 2021). Velocities and morphology. Scales: From microjets to pc-scale jets (see HH131, tens of pc, \sim size of a GMC), depends on the evolutionary stage and tracer. Jets can be probed using a very wide range of tracers. Have been observed from the X-ray regime to the radio band, much of the effort on the optical and NIR bands. Most part is characterized by line emission at least from the UV to the sub-millimeter. Different tracers are used for different regions and evolutionary phases. Jets from the youngest sources (class 0/I) can have a molecular component in pure rotational lines, at the (sub)mm, mostly CO, SiO, SO, see Section of molecular winds , and H₂ in the near-infrared. Class I and II mostly detected in the optical and near-IR, (e.g. H α , [FeII], [SII], [OI], [OII], [OIII], and [NII]), trace the atomic and ionized components (enumerate examples of lines). At the ionized jet base, radio jets: Thermal, free-free emission (positive α); non-thermal, gyrosynchrotron radiation (negative α) (Anglada et al., 2018). Correlations cm luminosity with bolometric luminosity and with outflow force. Rotation: Why is important and how is measured. Jet rotation tentatively detected in T-Tauri jets in the optical and NUV (Bacciotti et al., 2002; Coffey et al., 2007), quantify. Rotation also detected in molecular emission in HH212 (the clearest example, I think, since the jet is nearly contained in the plane-of-sky Lee et al., 2017). Detection in jet rotation is difficult, very high angular and spectral resolution are needed, some cases were later discarded (Coffey et al., 2012). Measurements are based on shock tracers, asymmetric shock structure and jet precession can mimick rotation (Erkal et al., 2021).

1.2.3.1 Radio jets

Necessary things to introduce Reipurth 50 (Anglada et al., 2018)

1.2.3.2 Molecular jets and bullets

Molecular jets, high-collimated molecular gas at EHV. Molecular bullets (Bachiller et al., 1990; Bachiller, 1996). Recent observations with high spatial and spectral resolution (mostly with ALMA), are providing revolutionary results (Lee, 2020). Present a table with the known cases of high velocity molecular jets (Table 1.1). Mostly present in Class 0 phase YSO. Recent surveys: Podio et al. (2021) and Dutta et al. (2023). Tracers: mostly CO, SiO, and SO (others as H₂CO and CH₃OH (Tafalla et al., 2010)). Chemical differentiation with the slower regimes and implications (Tafalla et al., 2010). Evolution of molecular component in jets.

Velocity gradient in the EHV knots: higher velocity upstream and lower velocity in the downstream side, suggesting lateral ejections. When the jet is close to be contained in the plane-of-the-sky, “sawtooth pattern”. Examples: IRAS 04166+2706 (Santiago-García et al., 2009; Tafalla et al., 2017), L1448C (Hirano et al., 2010), HH212 (Lee et al., 2015). Interpretations: Internal working surfaces in the jet (IWS) vs. axial density enhancements in a spherical wind model: Tafalla et al. (2017) vs Wang et al. (2019). Since the knots and bow shocks are well detected in shock tracers as SiO and H₂, they are not merely axial density enhancements. Thus, this gradients are naturally explained by lateral ejections from IWS. The model is similar to the one explaining the jet-driven scenario for large-scale outflows: variations in ejection velocities makes the fast jet material catches up with the slow jet material, forming an internal shocks propagating along the jet and producing sideways ejections. But, where do the molecules come from? Recent result with ALMA, along the recent observation of molecular winds explained in Section of molecular winds Disk winds around molecular jets: HH212 (Tabone et al., 2017; Lee et al., 2018b, 2021), HH211 (Lee et al., 2018a). This inspired Tabone et al. (2018) model.

Mention Ray et al. (2023).

1.3 Motivation of our work

In this thesis ...

This thesis is structured as follows:

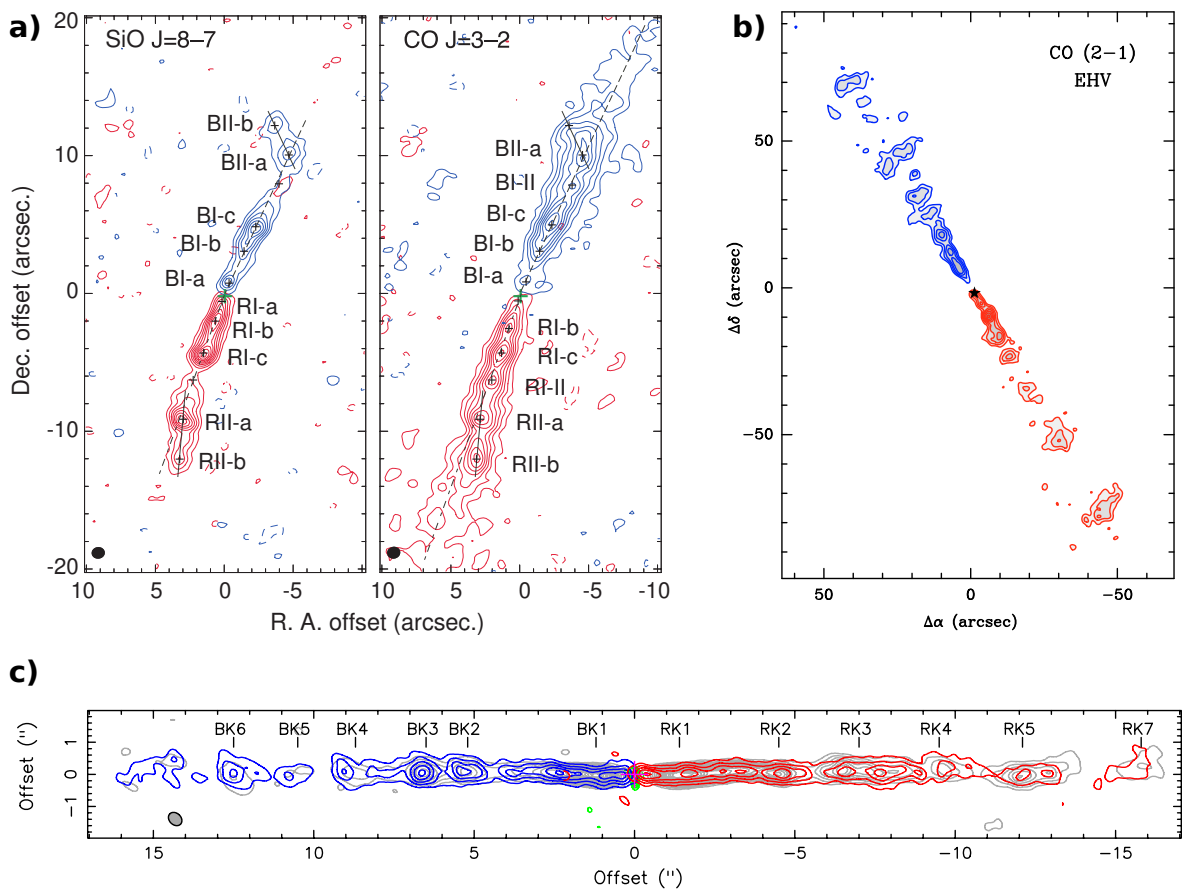


Figure 1.6 a) L1448C (Hirano et al., 2010). b) IRAS04166 (Santiago-García et al., 2009). c) HH211 (Lee et al., 2010; Moraghan et al., 2016)

Table 1.1. Young stellar objects with molecular jets.

Source	Class	Molecules	Distance (pc)	M_* (M_\odot)	L_{bol} (L_\odot)	v_j (km s $^{-1}$)	\dot{M}_j (M_\odot yr $^{-1}$)	\dot{M}_{acc} (M_\odot yr $^{-1}$)	Refs.
L1448C
SVS 13
SVS 13B
L1157
HH211
HH212
HH111
Cep E
IRAS 04166 :
IRAS4A2
IRAS 17233
C7
HH80-81
VLA 1624
SMM1-a
SMM1-b
Ser-emb8(N)
MMS5/OMC3
OMC2/FIR6b
B335
HOPS373?

Note. — Add some sources from (Podio et al., 2021) and (Dutta et al., 2023). IRAS2A monopolar molecular jet? (Codella et al., 2014a). Ser-emb 15 (Sato et al., 2023).

References. — L1448C: Bachiller et al. (1990), Hirano et al. (2010), Tafalla et al. (2010), Toledano-Juárez et al. (2023). SVS 13: Chen et al. (2016), Lefèvre et al. (2017), Blazquez-Calero et al. (submitted). L1157: Kwon et al. (2015), James et al. (2020). HH211: Gueth & Guilloteau (1999), Nisini et al. (2002), Hirano et al. (2006), Lee et al. (2009), Lee et al. (2010), Jhan & Lee (2016), Moraghan et al. (2016), Jhan & Lee (2021). HH212: Codella et al. (2014b), Lee et al. (2017), Lee et al. (2018b), Lee et al. (2021). HH 111: Cep E: Lefloch et al. (1996), Hatchell et al. (1999), Lefloch et al. (2015), Gómez-Ruiz et al. (2015), de A. Schutzer et al. (2022). I04166: Tafalla et al. (2004), Santiago-García et al. (2009), Wang et al. (2014), Tafalla et al. (2017), Wang et al. (2019). NGC1333 IRAS4A2: Choi et al. (2006), Choi et al. (2010), Choi et al. (2011), Ching et al. (2016). IRAS 17233-3606: Leurini et al. (2009). C7: Plunkett et al. (2015). Hatchell et al. (1999), Lefloch et al. (2007). HH80-81: Qiu & Zhang (2009), Cheng et al. (2019), Qiu et al. (2019). VLA 1624: Hara et al. (2021). SMM1-a: Hull et al. (2016), Hull et al. (2017), Tychoniec et al. (2019) SMM1-b: Hull et al. (2016), Hull et al. (2017), Tychoniec et al. (2019) Ser-emb 8(N): Tychoniec et al. (2019) MMS 5/OMC-3: Matsushita et al. (2019). OMC 2/FIR 6b: Matsushita et al. (2021). B335: Yen et al. (2010), Bjerkeli et al. (2019). HOPS 373: Yoon et al. (2022).

CHAPTER 2

RE50 RADIO JET

2.1 Introduction

2.2 Observations

2.3 Results

2.4 Analysis and discussion

2.5 Summary and conclusions

CHAPTER 3

THE SVS 13 SYSTEM

3.1 The SVS 13 protobinary

Introduction to SVS 13. Young binary located in NGC1333. HH7-11 (Hartigan et al., 2019). Palomar images. Outburst Eisloeffel. Protobinary discovery.

3.2 Two circumstellar disks and a circumbinary

Two circumstellar disks and a circumbinary disk (Diaz-Rodriguez et al., 2022) (Díaz Rodríguez, 2021)

3.3 The SVS 13 outflow

HH7-11, CARMA molecular outflow, H₂ arcs and Fe jet, HST arcs, molecular bullets Bachiller and Chen. Lefevre. Radio jet.

CHAPTER 4

ALMA OBSERVATIONS OF SVS 13 OUTFLOW

4.1 Introduction

Introduction to SVS 13. Young binary located in NGC1333. HH7-11 (Hartigan et al., 2019). Large-scale molecular outflow. SVS 13 large scale outflow was between the first ones (the sixth), and was associated to the HHs (Snell & Edwards, 1981). Bullets. Two circumstellar disks and a circumbinary disk (Díaz-Rodríguez et al., 2022) (Díaz Rodríguez, 2021).

4.2 Observations and data reduction

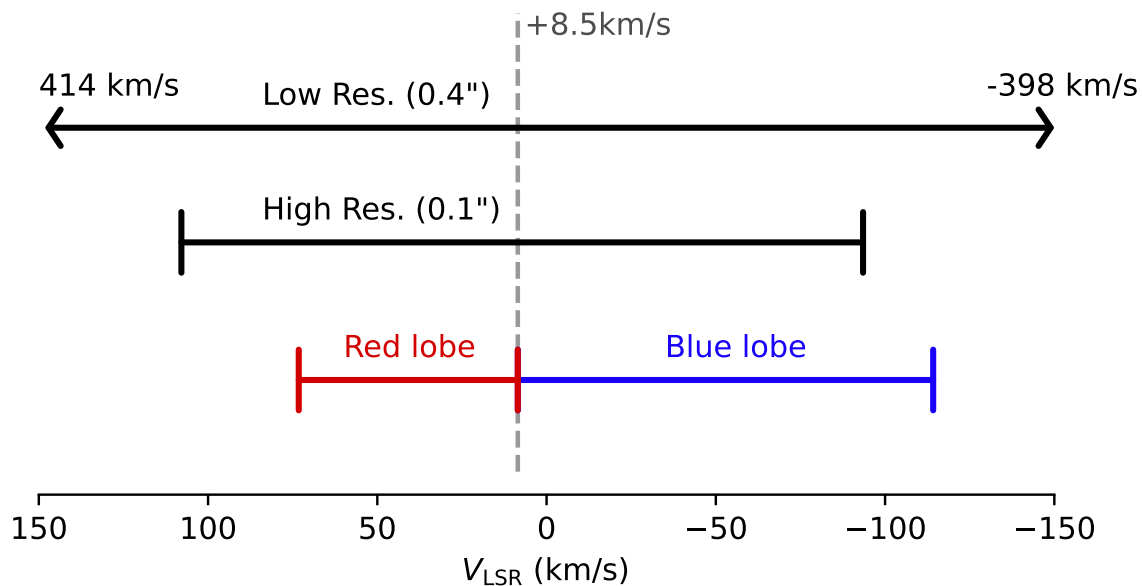


Figure 4.1 Graphical description of the spectral setup of the ALMA observations

The CO($J=3-2$) ALMA observations were carried out in band 7 (0.9 mm), during Cycle 3 (program 2015.1.01229.S; PI: G. Anglada) and Cycle 4 (program 2016.1.101305.S; PI: G. Anglada). Here, we present a summary of the observations focused on the CO($J=3-2$) data.

The Cycle 3 ALMA 12-m array observations were carried out during two runs on 2016 September 9 and 10, using 42 antennas with baselines in the range of 15–3225 m, providing an angular resolution of $\sim 0.^{\prime\prime}1$ and a maximum recoverable scale of $\sim 12.^{\prime\prime}$ (strict upper limit, obtained from the shortest baseline) and of $\sim 3.^{\prime\prime}$ (good quality imaging, obtained from the 5th percentile shortest baseline). The channel width was 122 kHz, corresponding to 0.106 km s⁻¹ at 345.795990 GHz, the assumed rest frequency of the CO($J=3-2$) transition. The total bandwidth was 234.375 MHz, covering an LSR velocity range from −93.32 to 109.47 km s⁻¹.

The Cycle 4 ALMA 12-m array data were obtained on 2016 November 24, using 43 antennas with baselines in the range of 15–704 m, providing an angular resolution of $\sim 0.^{\prime\prime}4$ and a maximum recoverable scale of $\sim 12.^{\prime\prime}$ (from the shortest baseline) and of $\sim 3.^{\prime\prime}$ (from the 5th percentile baseline). The channel width was 244 kHz, corresponding to 0.211 km s⁻¹, and the total bandwidth was 937.500 MHz, covering an LSR velocity range from −398.34 to 414.25 km s⁻¹.

In both cycles, the calibrators J0237+2848, J0238+1636, and J0336+3218 were used for the 12-m array bandpass, absolute flux, and complex gain calibration, respectively.

Cycle 4 observations with the 7-m Atacama Compact Array (ACA) were carried out on 2016 November 15, and 2017 July 7 and 26, with an angular resolution of $\sim 4.^{\prime\prime}$ and a maximum recoverable scale of $\sim 35.^{\prime\prime}$. The channel width was 122 kHz (0.106 km s⁻¹) with a total bandwidth of 250 MHz, covering an LSR velocity range from −100.00 to 116.64 km s⁻¹. The bandpass calibrator was J0510+1800 for the November 15 and July 7 observations, and J0522-3627 for the 26 July observations. The absolute flux calibrator was Ceres for the November 15 observations, and Uranus for the remaining observations. The complex gain calibrator was J0319+4130 for all the observations.

The phase center of all the observations was set at RA(ICRS)=03^h29^m03^s.75, Dec(ICRS)=31°16'04".00, within $\sim 0.3.^{\prime\prime}$ of the position of VLA4B. The FWHM of the 12-m primary beam is 18'', and that of the 7-m array is 32''. The images presented in this paper have not been corrected by the primary beam response, except when indicated.

The observations were pipeline calibrated using CASA versions 4.7.01 and 4.7.2, for Cycle 3 and 4, respectively. Additionally, the 12-m array Cycle 3 data (1.6 h on-source with $\sim 0.1.^{\prime\prime}$ resolution) were phase self-calibrated. Self-calibration was unsuccessful for the Cycle 4 data (only 4.15 min on-source with $\sim 0.4.^{\prime\prime}$ resolution).

Because of the small primary beam of the ALMA 12-m array, only Bullet 1 has been imaged with these data. The larger size of the ACA primary beam allows us to detect Bullet 2 in CO($J=3-2$), but at low angular resolution (see Extended Data Fig. 9).

4.3 Results

4.3.1 Description of the molecular outflow

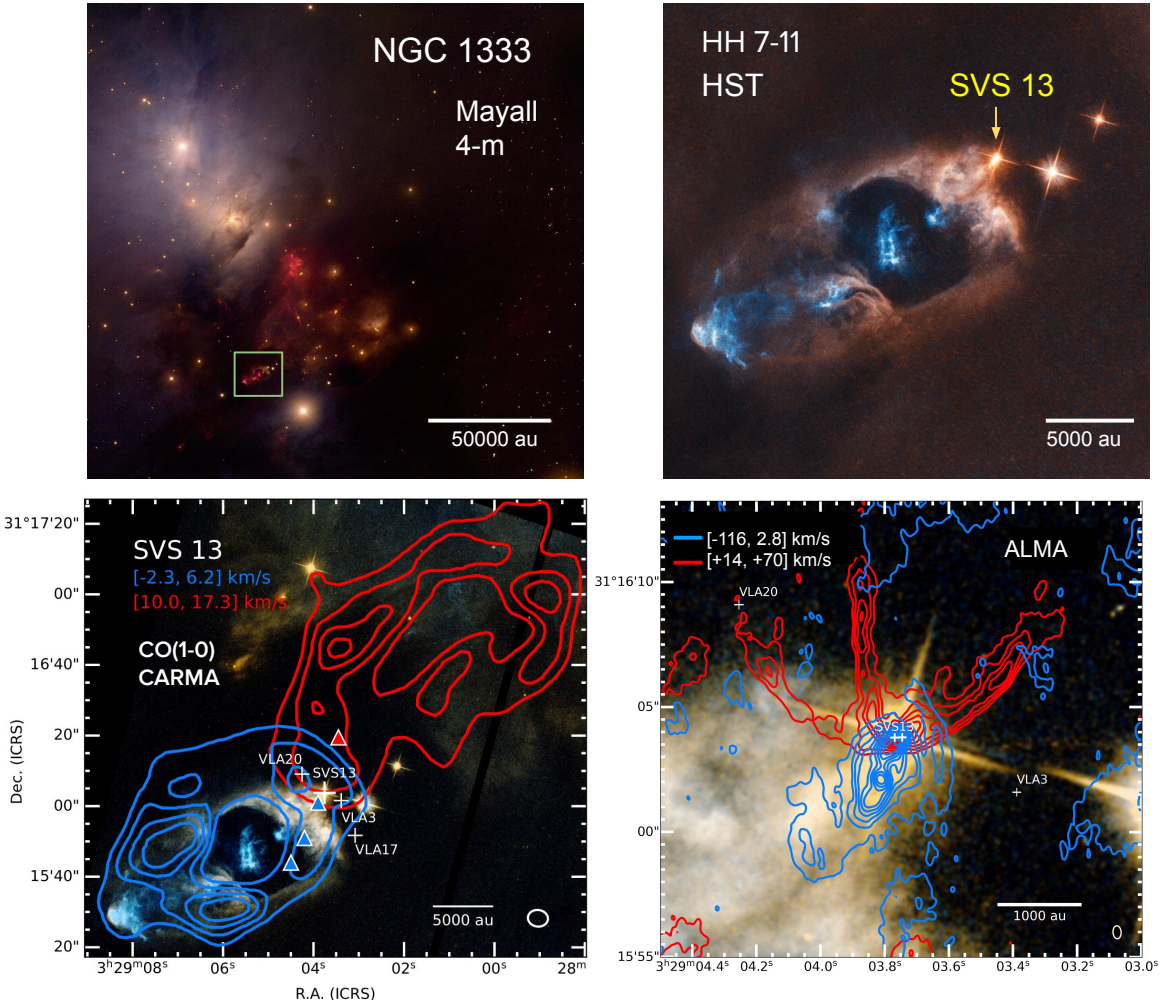


Figure 4.2 NGC1333, HH7-11, SVS 13 large-scale molecular outflow, ALMA view of the molecular outflow.

Broad description of the outflow. Description of the blue and red lobes. Outflow cavities. EHV emission. Nebulosities?. Molecular bullet 1 and 2 with ACA. Rich substructure in bullet 1 with ALMA.

4.3.2 Substructure of the molecular jet

Moments. Correspondance of the maxima with the arcs of Hodapp. Channel maps. Identification of the observed line emissionsas CO.

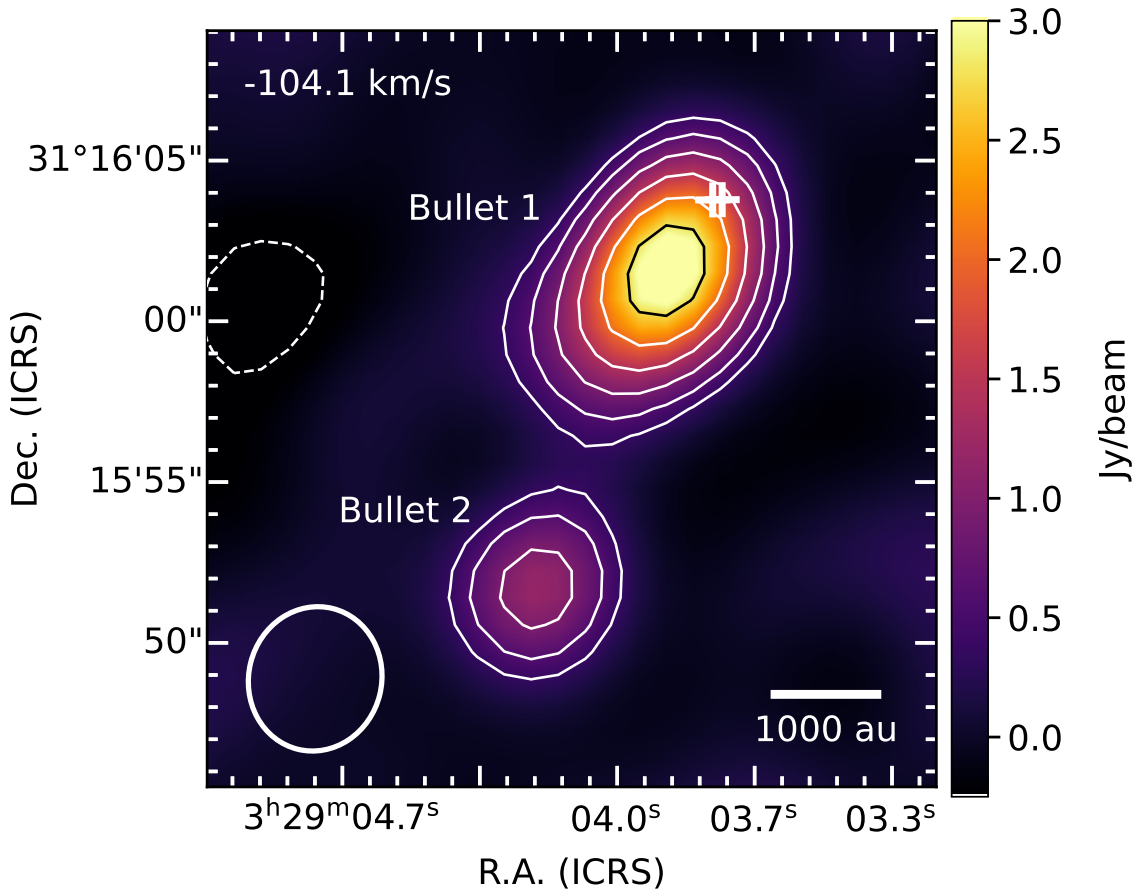


Figure 4.3 Extended Data Fig. 9: Detection of Bullet 2 with ACA. Image of the CO($J=3-2$) line emission of the blueshifted bullets 1 and 2 in SVS 13, obtained with the 7-m ACA array, at an LOS velocity of -104 km s $^{-1}$ relative to VLA 4B ($v_{\text{LSR}} = +9.3$ km s $^{-1}$) Diaz-Rodriguez et al. (2022), where the emission of Bullet 2 peaks. The synthesized beam is $4''.51 \times 4''.13$ (PA = -13.90°), and the channel width is 0.44 km s $^{-1}$. Contour levels are -3, 3, 5, 8, 12, 17, 23, and 30 times 0.12 mJy beam $^{-1}$, the rms of the map. The position of the SVS 13 binary is indicated with white plus signs. The image has not been corrected for the primary beam response. Bullet 2 appears unresolved in the ACA image, with a flux density is 1.9 Jy, after correction for the primary beam response. This second bullet is not detected with the ALMA 12-m array because of a lack of sensitivity at the distances where it is located, due to the smaller size of the 12-m array primary beam. The second bullet was previously detected only at longer wavelengths Bachiller et al. (2000); Chen et al. (2016); Lefèvre et al. (2017).

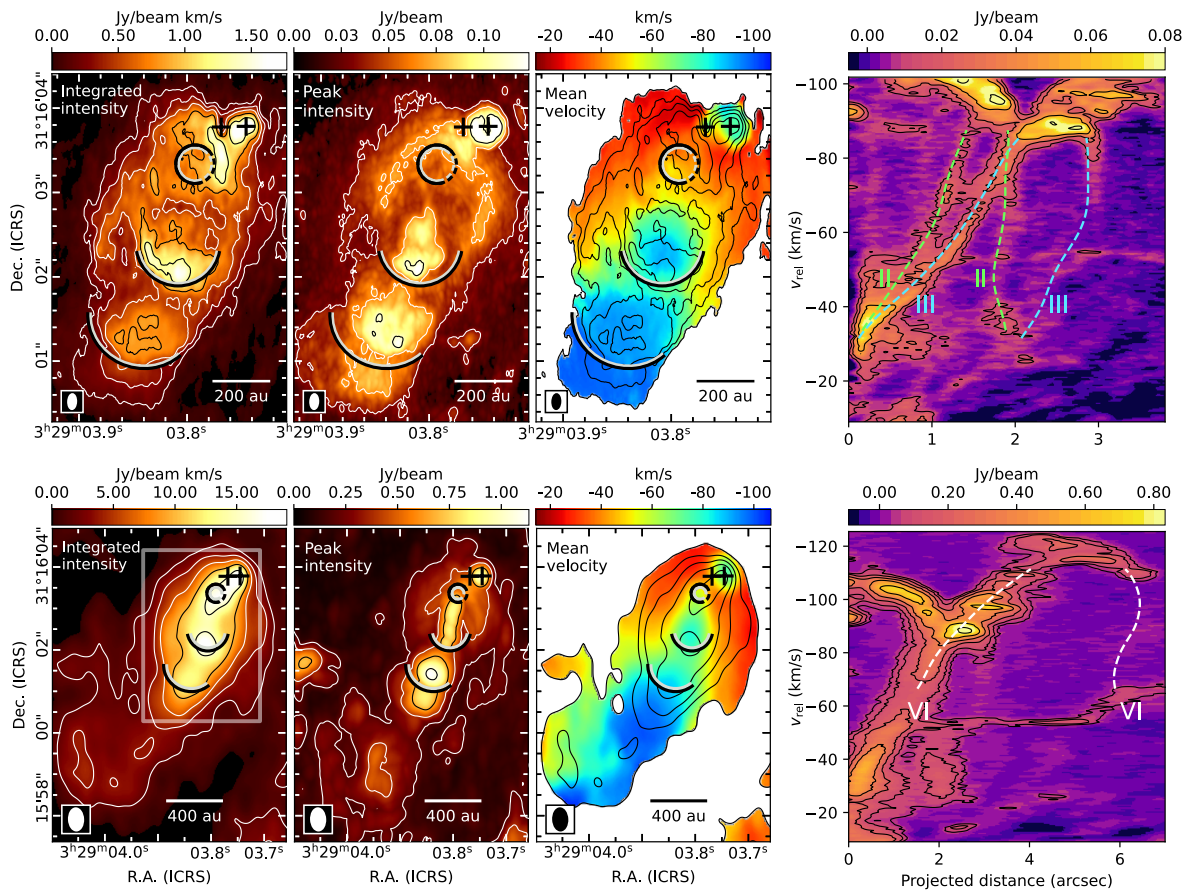


Figure 4.4 Observed CO($J=3-2$) images and position-velocity diagrams of the blueshifted Bullet 1 in SVS 13. Panels in the top row have been obtained from the high-angular resolution ALMA CO($J=3-2$) data (beam = $0''.173 \times 0''.091$, PA = -2.2°) covering the velocity range from -9.3 to -102.7 km s $^{-1}$. Panels in the bottom row have been obtained from lower angular resolution ALMA data (beam = $0''.527 \times 0''.333$, PA = 2.7°) that cover a wider velocity range, from -9.3 to -126.4 km s $^{-1}$. **First column:** Images of the velocity-integrated intensity (zeroth-order moment of the spectral cube). Contour levels are 3, 6, 10, 16 and 25 times 0.05 Jy beam $^{-1}$ km s $^{-1}$ (top) and 0.61 Jy beam $^{-1}$ km s $^{-1}$ (bottom). **Second column:** Images of the peak intensity of the spectral cubes. Contour levels are 3, 6, 10, and 16 times 0.011 Jy beam $^{-1}$ (top) and 0.066 Jy beam $^{-1}$ (bottom). **Third column:** Images of the mean velocity field (first-order moment, or intensity-weighted average velocity), in color scale, overlaid on the integrated intensity (in contours). **Fourth column:** Position-velocity diagrams (width = $0.1''$ and $0.4''$ for top and bottom panels, respectively) along the longitudinal axis of the bullet (PA = 160°), and origin in VLA 4B, with the emission of the families of rings II, III, and VI (defined in Fig. 4.7) indicated with green and cyan (top row) and white (bottom row) dashed lines, respectively. Contour levels are 5, 10, 20, 35, 60 and 90 times 0.0025 Jy beam $^{-1}$ (top) and 0.010 Jy beam $^{-1}$ (bottom). The positions of the two protostars of the SVS 13 binary, VLA 4A (west) and VLA 4B (east), near the top right corner of the images, are indicated by plus signs. All velocities are LOS velocities relative to that of VLA 4B ($V_{\text{LSR}} = +9.3$ km s $^{-1}$). The images have been corrected by the decrease in sensitivity due to the primary beam response. For the high-resolution data (top images) a clipping of 14 mJy beam $^{-1}$ ($4-\sigma$ before primary beam correction) has been applied to the individual channel maps (with the native channel width of 0.106 km s $^{-1}$) before constructing the moments. The H $_2$ arcuate features are plotted as arcs using double, black and white, lines for better visibility; their positions have been obtained from the infrared images, adopting the Gaia coordinates for the star ($\sim 0.07''$ south-east from the radio position of VLA 4B), and correcting for the estimated proper motions of the arcs relative to the star. Synthesized beams are plotted as ellipses at the bottom left corner of the images.

The velocity centroid map (third column in Fig. 4.4) shows a clear apparent acceleration with distance from SVS 13, confirming previous lower resolution results. The velocity field is roughly symmetric with respect to the jet axis. This is in contrast with early claims for large transverse velocity gradients which probably resulted from an insufficient angular resolution and/or centroid calculation over very specific velocity ranges. A more revealing and striking view of the kinematics is obtained by looking at individual line channels in the CO($J=3-2$) image cube (see Fig. 4.5, Extended Data Fig. 1, Supplementary Figs. 1 and 2, and Supplementary Videos 1 and 2). The channel images (specially the data of $\sim 0.1'' = 30$ au resolution) show several sequences of rings whose positions and sizes change smoothly as a function of the line-of-sight (LOS) velocity. The rings are narrow, until they abruptly transform into a bright filled circle that we call the “head”. We call each of these sequences of rings (and its head) a “family”. The rings are detected at LOS velocities from approximately -9 to -125 km s $^{-1}$ relative to the cloud, have radii in the range $0.2''$ to $2.5''$ (60 to 750 au) and extend southeast up to $\sim 5''$ (~ 1500 au), in projection, from SVS 13. In general, the brightest part of a ring is that closest in projection to SVS 13 and, in some cases, the rings appear incomplete, as arcs. Assuming that the heads of the families are moving approximately along the symmetry axis, at an inclination angle $i = 25^\circ$ (except for Rings I, for which we assume $i = 22^\circ$) (see Methods), we can estimate their dynamical times from the ratio of their deprojected positions and mean velocities. We obtain dynamical times of 25 ± 5 , 56 ± 6 , 91 ± 9 , 100 ± 9 , and 134 ± 15 yr for families I-IV and VI, respectively (see bottom right panels of Fig. 4.7). For family V, the head is not identified in our data and we obtain an upper limit of 102 yr from the positions and velocities of the rings. The typical separation in dynamical time between consecutive families is a few tens of years, suggesting a relationship with episodic mass ejection events separated this timescale. Interestingly, the epoch of the most recent ejection (family I, associated with a change in the orientation of the outflow) is 1992 ± 5 , consistent with the epoch of the strong optical/infrared outburst of the visible component of SVS 13 (VLA 4B), which occurred in 1990 ± 1 , suggesting an association between these phenomena. To our knowledge, this is the first time that such a close association between an optical/infrared outburst and an EHV molecular bullet has been demonstrated. To illustrate the direction changes in the SVS 13 outflow, we plot in the bottom right panels of Fig. 4.7 the PA relative to VLA 4B, measured at the head of each family, as a function of the estimated dynamical time.

Families of rings.

Ellipse fitting.

The ellipse fitting to the rings in the channel maps has been carried out using an interactive program written in Python. This program finds the geometrical parameters (center coordinates, semimajor-axis, ellipticity, and PA) that maximize the mean intensity that falls within an elliptical annulus (we chose a width of a few pixels, $\sim 1/3$ of the beam size). The program takes as initial guess the geometrical parameters of an ellipse that visually fits a targeted ring, calls the function “minimize” from the Python’s package SciPy, and returns the best-fit parameters. The fitting method L-BFGS-B was chosen, which allows bound-constrained minimizations. It is crucial to constrain the parameter-space to ensure that the fitting is performed to the targeted ring of a given family. In this manner, we avoid that

additional emission affects the fit, whether the additional emission comes from a ring of a different family or from other kind of structure.

We note that, when two rings of different families intersect in a given channel map, the inner region common to both rings often appears enclosed within the arcs (one from each ring) that connect the intersection points (see the middle row of panels in Fig. 4.5); these connected arcs simulate a (fake) third small ring, which must be excluded from the fit. This means that the classification of rings into families has to be performed previously to the fitting, once it is clear which are the true rings that should be fitted. To better ensure the correct identification of rings in families, we perform the fitting on a channel by channel basis, using as initial parameters the solution of the previous channel fit. This usually gives good solutions, since the rings of a given family vary smoothly with velocity. We note that the elliptical fits of the heads of the families, which appear as filled emission, are visual estimates.

In Supplementary Figs. 1 and 2 we present the whole set of channel maps, with the elliptical fits superimposed on the rings (see also Supplementary Video 3, where we show how the elliptical fits change with the channel maps).

4.3.3 Families of rings

4.4 Analysis and discussion

4.4.1 Identification of the observed line emission as CO at extremely high velocities.

It is known that there is line emission associated with the SVS 13 disks corresponding to transitions of other molecular species, with different rest frequencies. For several of these transitions the difference in frequency with respect to the CO($J=3-2$) transition is similar to the Doppler shift corresponding to the range of velocities observed in the bullet. Therefore, in principle, it could occur that the emission that we attribute to EHV blueshifted CO in the bullet is indeed emission from other molecular transitions with higher rest frequencies arising from material moving at much lower velocities. We argue that this is not the case. Since CO is the most abundant detectable molecule, if the emission observed in some channels corresponds to other molecules, then we would expect to detect a CO “replica” of this emission in the velocity channels corresponding to the difference in frequency with respect to CO, which is not observed. In addition, we identified SO(8_8-7_7) emission in the bullet from a spectral window dedicated to continuum observations, with a low spectral resolution of 27.2 km s^{-1} . Considering the rest frequency of this transition, 344.310612 GHz, the emission reaches velocities about -120 km s^{-1} (relative to the LSR velocity of VLA 4B), the same as the CO in the bullet. In Figure Extended Data Fig. 2, we show the integrated SO emission in the bullet. With a spatial resolution of $0.^{\circ}54 \times 0.^{\circ}36$, we can distinguish the main morphological substructure we found in the CO channel maps. Thus, we confirm that the main substructure observed in the bullet is traced by different molecular transitions, and that the

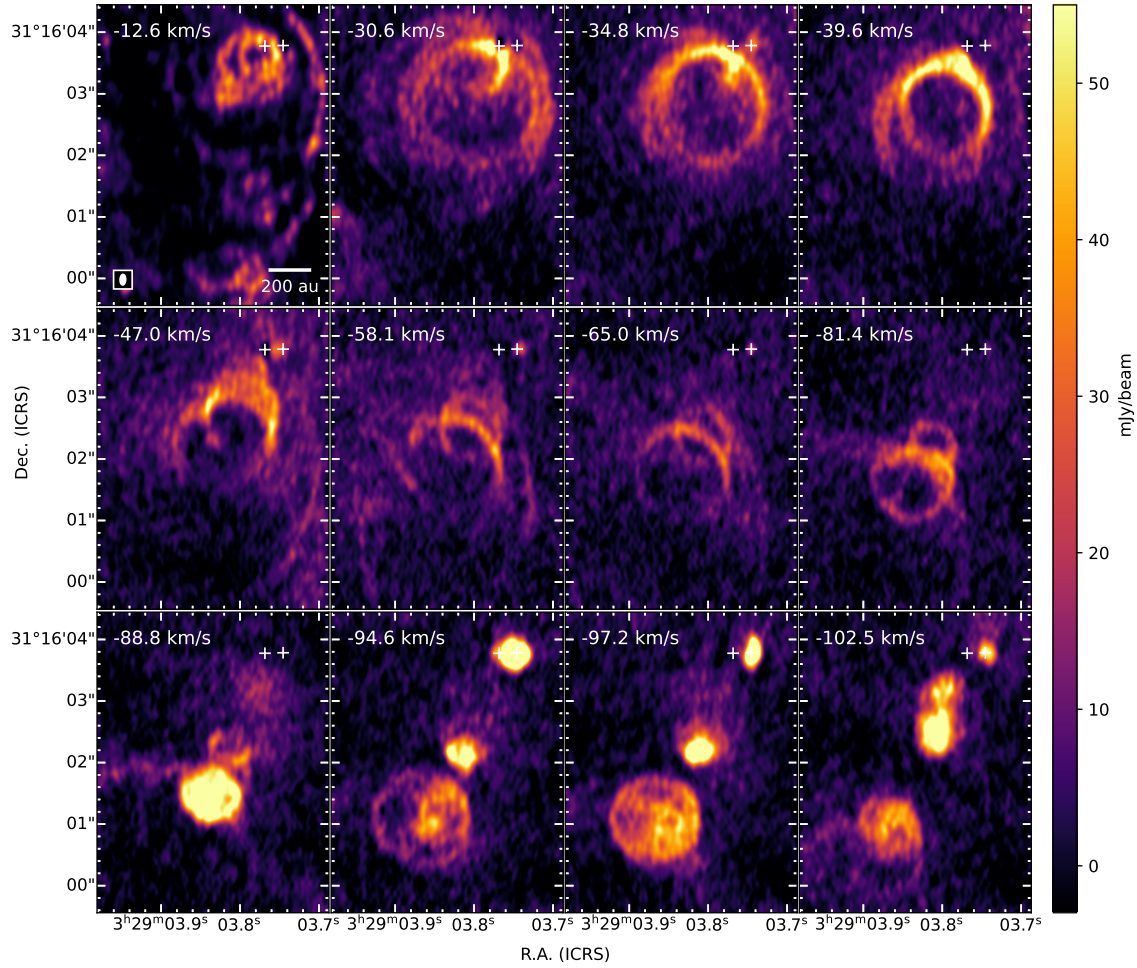


Figure 4.5 Observed CO($J=3-2$) spectral channel images at high angular resolution. A sample of high angular resolution channel maps of the CO($J=3-2$) emission observed by ALMA, which illustrate the ringed kinematic structure of the bullet. The synthesized beam is $0.^{\circ}173 \times 0.^{\circ}091$ (PA = -2.2°), and is plotted as an ellipse in the bottom left corner of the first image. The full set of observed channel maps is shown in Supplementary Fig. 1 and Supplementary Video 1. The positions of the two protostars of the SVS 13 binary are indicated by plus signs. The LOS velocity relative to VLA 4B is shown in the top left corner of each image. The width of each of the channels shown in the figure is 0.53 km s^{-1} , which corresponds to the average of five native channels. The rms of the images is $2.6 \text{ mJy beam}^{-1}$. Images have not been corrected by the primary beam response. Lower angular resolution channel maps, covering a wider range of velocities, are shown in Extended Data Fig. 1, Supplementary Fig. 2 and Supplementary Video 2.

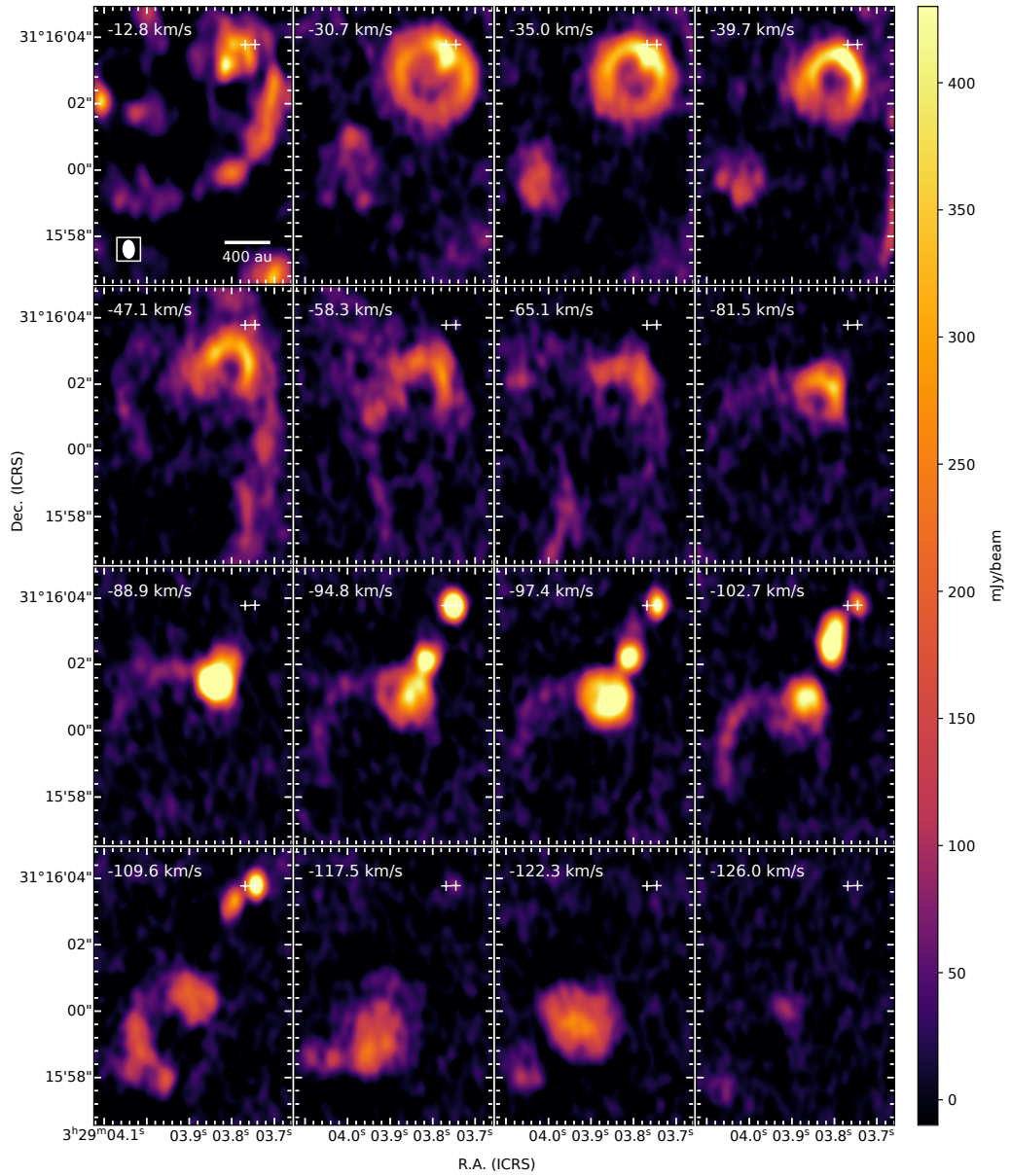


Figure 4.6 Observed CO spectral channel images of Bullet 1 at low angular resolution. A sample of spectral channel images of the CO($J=3-2$) emission observed by ALMA with a synthesized beam of $0''.527 \times 0''.333$ (PA = 2.7°). The obtained data cover a range of velocities wider than the high angular resolution data shown in Fig. 4.5. The positions of the two protostars of the SVS 13 binary (Anglada et al., 2000) are indicated by plus signs. The LOS velocity, relative to the velocity of VLA 4B ($V_{\text{LSR}} = +9.3 \text{ km s}^{-1}$; Diaz-Rodriguez et al., 2022), is shown in the top left corner of each image. The width of each of the spectral channels is 0.53 km s^{-1} . The rms of the images is 10 mJy beam^{-1} . Images have not been corrected by the primary beam response. The synthesized beam is plotted as an ellipse in the bottom left corner of the first image.

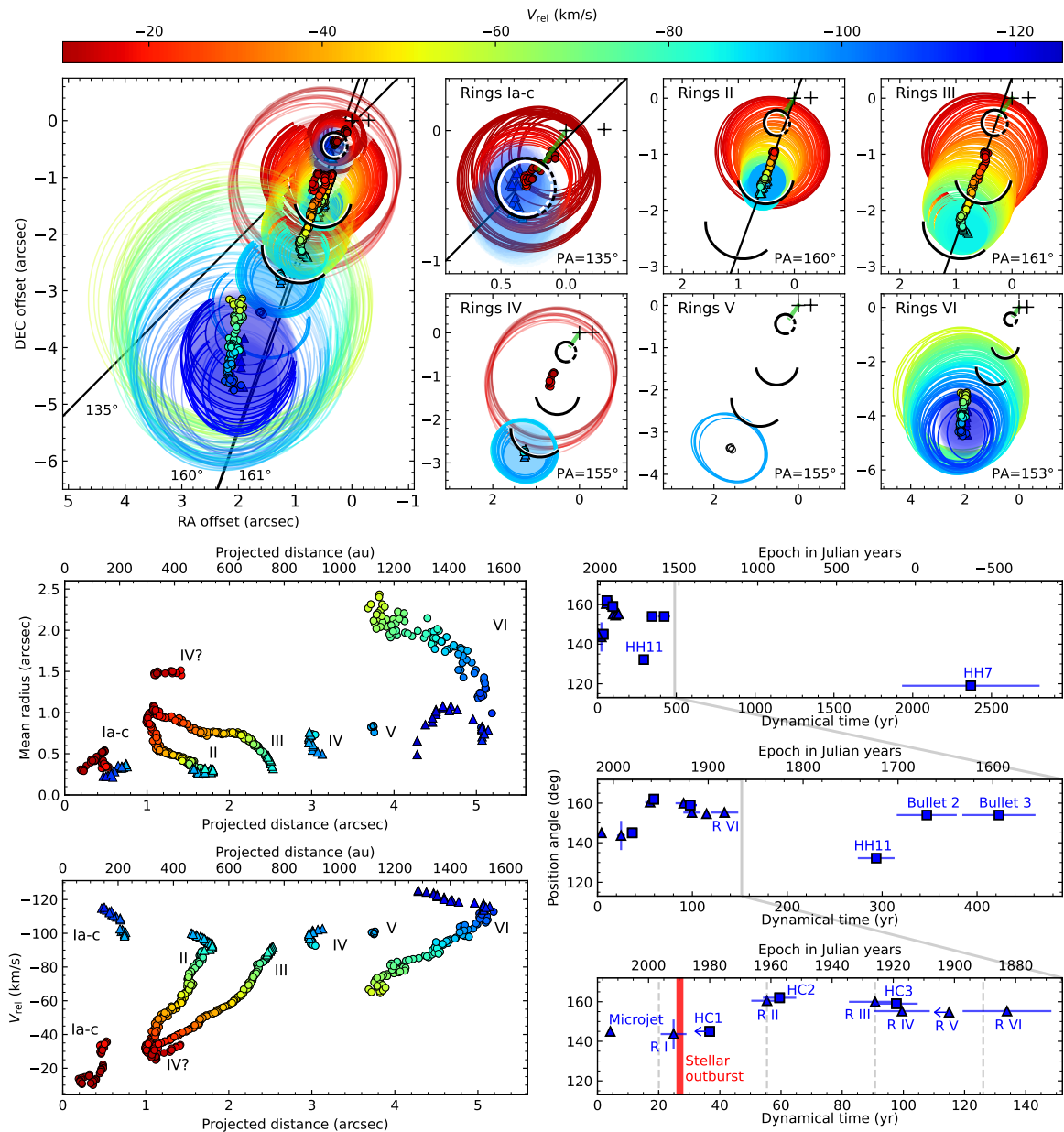


Figure 4.7 Decomposition of the ringed emission through elliptical fits. **Top left panel:** Color-coded plot of elliptical fits to the observed CO($J=3-2$) spectral channel images (see Methods for fitting procedure). Rings are represented by the ellipses that best-fit their emission, and filled emission regions are represented by shaded areas. Some ellipses have been drawn with increased transparency to improve the visualization. Color dots and triangles indicate the centers of the rings and of the regions of filled emission, respectively. The color represents the LOS velocity relative to VLA 4B. We note a trend of the rings to group in sequences that we call “families”. In each family, the absolute value of the velocity of the rings increases and their size decreases with distance to the stars (indicated as black plus signs), ending in a filled region of emission (the “head”). Several “families” of rings (labeled I to VI) are identified. The centers of the rings in each family appear rather well aligned, and linear regression fits to these positions for families I, II, and III are plotted as black **Top right panels:** Separate plots of each of the identified families of rings. The green segment in the **Bottom left panels:** Plots of the mean radius (mean of the semimajor and semiminor axes of the ellipses) and the LOS velocity of the fitted rings, as a function of the distance (projected on the plane of the sky) of their centers to VLA 4B. The plots illustrate the general trends (except for the heads) for the radius to decrease with distance, and for the velocity to linearly increase with distance (a “Hubble-Lemaître type” law). The different families of rings are easily identified in the plots. **Bottom right panels:** PA as a function of the dynamical time for the heads of the families of rings (plotted as triangles and labeled R I to R VI; see Methods for details on the calculations), as well as for other features associated with the SVS 13 outflow, such as HH objects (plotted as squares and labeled HH7, HH11), [FeII] jet (triangle labeled as Microjet), and H₂ arcs (squares labeled as HC1, HC2, HC3). We assumed inclination angles from 22° to 25° (see Methods). Epoch is given in Julian years, with epoch 2000 corresponding to the standard definition of Julian epoch J2000.0. Dynamical times are relative to the date of our high-angular resolution ALMA observations (epoch 2016.69).

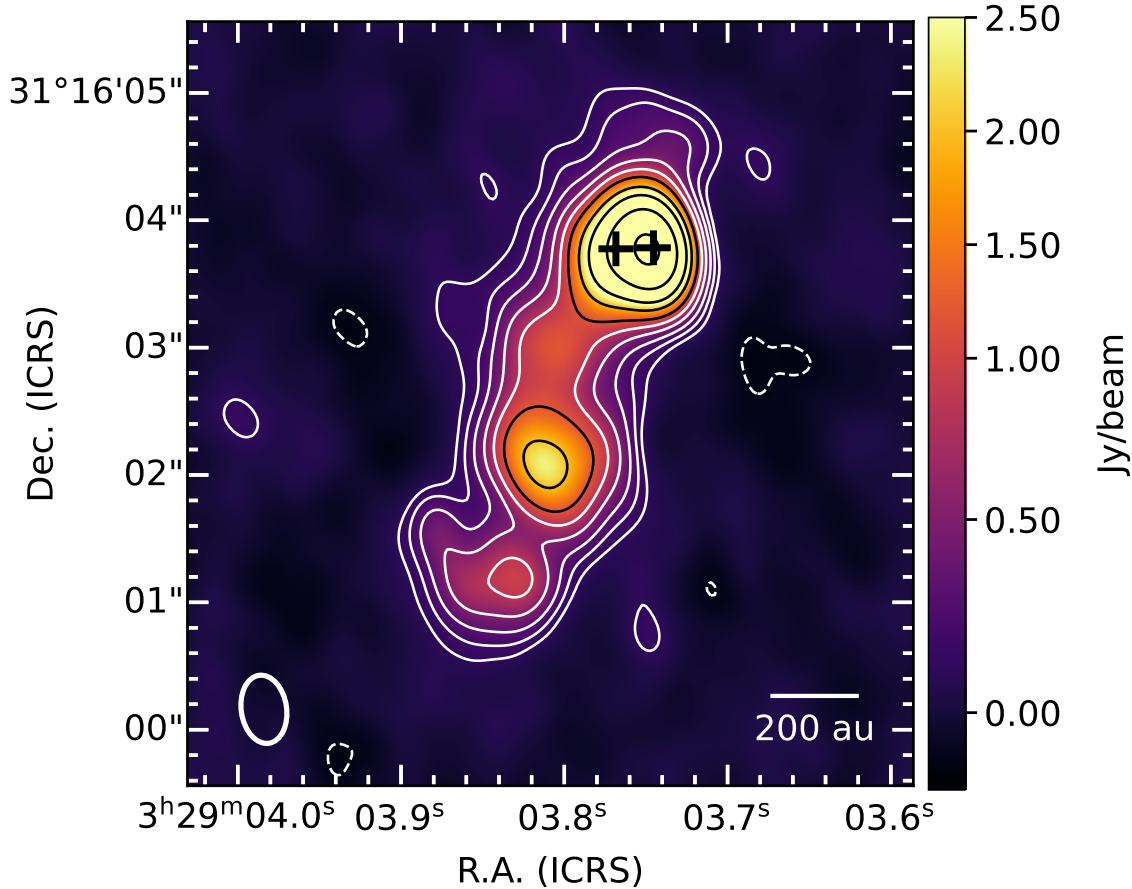


Figure 4.8 Observed SO image of Bullet 1. Image of the velocity-integrated intensity of the $\text{SO}(8_8-7_7)$ line observed with the ALMA 12-m array using a low spectral resolution spectral window dedicated to continuum observation, with a channel spacing of 13.6 km s^{-1} . The emission has been integrated in the LOS velocity range from -9.8 to -118.6 km s^{-1} relative to the velocity of VLA 4B ($+9.3 \text{ km s}^{-1}$). The positions of the two protostars of the SVS 13 binary (Anglada et al., 2000) are indicated by plus signs. The synthesized beam, shown in the bottom left corner, is $0.^{\prime\prime}54 \times 0.^{\prime\prime}36$ (PA = 8.37°). Contours are $-3, 3, 5, 8, 13, 20, 30, 50, 80, 140, 260$ times $0.04 \text{ Jy beam}^{-1} \text{ km s}^{-1}$. The image has not been corrected by the primary beam response.

substructure reported in the CO does not arise from the overlapping of different molecular lines in the same channel maps. Moreover, the main kinematical features of the bullet we have observed in CO(3-2) were already present, with the same velocities, in (lower resolution) CO(2-1) data, as well as in other molecular transitions, such as SiO(5-4) and SO(6₅-5₄) lines. This coincidence in velocity is obviously highly unlikely if it were just the result of contamination from other species.

4.4.2 Inclination angle

From the high-angular resolution H₂ S(1) results(Hodapp & Chini, 2014) we can obtain a rough estimate of the inclination angle of the flow with respect to the LOS. For the farthest H₂ arc (HC3), a proper motion of ~ 30 mas yr⁻¹ (~ 43 km s⁻¹) relative to VLA 4B was measured(Hodapp & Chini, 2014). This arc is positionally associated with the head of family III, that has a LOS velocity of -90 km s⁻¹ relative to the velocity of VLA 4B ($V_{\text{LSR}} = +9.3$ km s⁻¹)(Diaz-Rodriguez et al., 2022). Thus, combining the proper motion of this H₂ arc and the LOS velocity of the head, we obtain an inclination angle $i = 25^\circ \pm 2^\circ$. However, a proper motion for the second H₂ arc (HC2) could not be measured by Hodapp & Chini (2014), so we derive its dynamical time assuming the same proper motion as HC3. Combining proper motion and LOS velocities, an inclination angle $i = 22^\circ \pm 3^\circ$ for the H₂ bubble (HC1) and the [FeII] jet was inferred (Hodapp & Chini, 2014). Since HC1 is positionally associated with the head of family I, we assume the same inclination angle of $22^\circ \pm 3^\circ$ for this family. Moreover, inclination angles of $i = 24^\circ \pm 2^\circ$ for the Herbig-Haro object HH 11 and $i = 25^\circ \pm 5^\circ$ for HH 7C (a substructure of HH 7) were reported (Hartigan et al., 2019). Thus, in order to estimate the dynamical times of the outflow features of SVS 13 (see bottom right panels in Fig. 4.7), we have adopted the inclination angles determined above. We note that the range of inclination angles mentioned above is compatible with our independent estimate of $i \simeq 20^\circ$ obtained from our bowshock modeling (see “Bowshock model” section below in these Methods).

4.4.3 Dynamical times of the heads of the ring families

We have obtained the dynamical times of the heads of the families of rings (see bottom right panel in Fig. 4.7), assuming they have traveled with constant velocity in a straight direction along the jet axis, so

$$t_{\text{head}} = \frac{x'_{\text{head}}}{v'_{\text{head}} \tan i}, \quad (4.1)$$

where x'_{head} is the projected distance (on the plane of the sky) from the source to the head, v'_{head} is its LOS velocity relative to VLA 4B, and i is the inclination angle of the flow with respect to the LOS (we use $i = 22^\circ \pm 2^\circ$ for Rings I and $i = 25^\circ \pm 2^\circ$ for the rest of the families, see “On the inclination angle” section in Methods). Both x'_{head} and v'_{head} are obtained by locating the maximum emission of each family of rings. For this, we first obtain several estimates of x'_{head} by locating the positions of the local maxima of emission near the jet

axis in the peak intensity images (see second column of Fig 4.4). Toward each of these positions we obtain spectra within a box with size of the order of the synthesized beam, and take v'_{head} as the LOS velocity of the emission peak. We then estimate the dynamical time of the head, t_{head} , as the mean value of the dynamical times calculated using every measured pair of x'_{head} and v'_{head} values. The standard deviation of the dynamical times obtained in this way for a given head is of a few years (as indicated in the error bars of the bottom right panel of Fig. 4.7).

Using this procedure, we obtain dynamical times $t_{\text{head}} = 25 \pm 5, 56 \pm 6, 91 \pm 9, 100 \pm 9, < 102$, and 134 ± 15 yr, for ring families I to VI, respectively. We note that we could not find a clear maximum associated with the rings V head, which is expected to be located somewhere between the positions of rings IV and rings VI, but in a velocity range only available in the lower resolution images. Hence, we give only an upper limit for the dynamical time of rings V, obtained by substituting x'_{head} and v'_{head} in equation (4.1) by the central position and the LOS velocity, respectively, of the ring observed in the highest velocity channel map of our high-angular resolution data.

4.4.4 Association of a molecular bullet with an optical/infrared outburst

4.4.5 Excitation temperature

An estimate of the excitation temperature can be obtained from the observation of two rotational molecular transitions, $J \rightarrow J-1$ and $J' \rightarrow J'-1$. From Boltzmann's equation, and using equations (4.6) and (4.7) to obtain the ratio of populations between the J and J' levels, we get:

$$\frac{J'}{J} \frac{e^{h\nu_{J',J'-1}/k_B T_{\text{ex}}} - 1}{e^{h\nu_{J,J-1}/k_B T_{\text{ex}}} - 1} \frac{\ln \left\{ 1 - \frac{I_{\nu}(J \rightarrow J-1, v_z)}{f_b [B_{\nu}(\nu_{J,J-1}, T_{\text{ex}}) - B_{\nu}(\nu_{J,J-1}, T_{\text{bg}})]} \right\}}{\ln \left\{ 1 - \frac{I_{\nu}(J' \rightarrow J'-1, v_z)}{f'_b [B_{\nu}(\nu_{J',J'-1}, T_{\text{ex}}) - B_{\nu}(\nu_{J',J'-1}, T_{\text{bg}})]} \right\}} = e^{-(E_J - E_{J'})/k_B T_{\text{ex}}}, \quad (4.2)$$

where $\nu_{J,J-1}$ and $\nu_{J',J'-1}$ are the frequencies, $I_{\nu}(J \rightarrow J-1, v_z)$ and $I_{\nu}(J' \rightarrow J'-1, v_z)$ the intensities, and E_J and $E_{J'}$ the upper energy levels of the two transitions, $B_{\nu}(\nu, T)$ is the Planck function at frequency ν and temperature T , and f_b and f'_b the beam-filling factors at the native angular resolution of the $J \rightarrow J-1$ and $J' \rightarrow J'-1$ observations, respectively.

Assuming the solid angle of the source is the same in both transitions, equation (4.2) can be written in terms of the intensity of one of the transitions (e.g., the $J \rightarrow J-1$ transition) and the ratio $R_{J/J'} \equiv I'_{\nu}(J \rightarrow J-1, v_z)/I_{\nu}(J' \rightarrow J'-1, v_z) = (f'_b/f_b) I_{\nu}(J \rightarrow J-1, v_z)/I_{\nu}(J' \rightarrow J'-1, v_z)$, where $I'_{\nu}(J \rightarrow J-1, v_z)$ is the intensity of the $J \rightarrow J-1$ transition when convolved to the

$J' \rightarrow J'-1$ beam, resulting:

$$\frac{J'}{J} \frac{e^{h\nu_{J',J'-1}/k_B T_{\text{ex}}} - 1}{e^{h\nu_{J,J-1}/k_B T_{\text{ex}}} - 1} \frac{\ln \left\{ 1 - \frac{I_\nu(J \rightarrow J-1, v_z')}{f_b [B_\nu(v_{J,J-1}, T_{\text{ex}}) - B_\nu(v_{J,J-1}, T_{\text{bg}})]} \right\}}{\ln \left\{ 1 - \frac{I_\nu(J \rightarrow J-1, v_z')}{f_b R_{J/J'} [B_\nu(v_{J',J'-1}, T_{\text{ex}}) - B_\nu(v_{J',J'-1}, T_{\text{bg}})]} \right\}} = e^{-h\nu_{J,J-1}/k_B T_{\text{ex}}}. \quad (4.3)$$

In this way, only the filling factor of the (unconvolved) $J \rightarrow J-1$ transition, f_b , is needed. This approach is particularly useful when this transition is observed at very high angular resolution, so $f_b \simeq 1$. This equation can be solved numerically to obtain T_{ex} .

For the particular case of the $J=3 \rightarrow 2$ and $J'=2 \rightarrow 1$ transitions we have:

$$\frac{2}{3} \frac{e^{h\nu_{21}/k_B T_{\text{ex}}} - 1}{e^{h\nu_{32}/k_B T_{\text{ex}}} - 1} \frac{\ln \left\{ 1 - \frac{I_\nu(3 \rightarrow 2, v_z')}{f_{32} [B_\nu(v_{32}, T_{\text{ex}}) - B_\nu(v_{32}, T_{\text{bg}})]} \right\}}{\ln \left\{ 1 - \frac{I_\nu(3 \rightarrow 2, v_z')}{f_{32} R_{3/2} [B_\nu(v_{21}, T_{\text{ex}}) - B_\nu(v_{21}, T_{\text{bg}})]} \right\}} = e^{-h\nu_{32}/k_B T_{\text{ex}}}. \quad (4.4)$$

CO($2 \rightarrow 1$) line observations of the SVS 13 bullets, with a synthesized beam of $2.\prime\prime 8 \times 2.\prime\prime 6$, where carried out with the SMA (Chen et al., 2016). From the contour levels in the channel maps presented in Chen et al. (2016), we estimated the CO($2 \rightarrow 1$) intensity at different positions and LOS velocities. After convolution of our CO($3 \rightarrow 2$) data to match the SMA beam, we estimated the intensity ratio $R_{3/2}$ at these positions and velocities. Then, solving equation (4.4) we obtained T_{ex} using the $R_{3/2}$ ratios and the measured CO($3 \rightarrow 2$) intensities toward the same positions in our high-angular resolution ALMA observations, with a native resolution of $0.173'' \times 0.091''$, for which we assume a beam-filling factor $f_b \simeq 1$. We obtained typical values of the ratio $R_{3/2} \gtrsim 4$, and CO($3 \rightarrow 2$) intensities in our high-angular resolution ALMA observations of $I_\nu(3 \rightarrow 2) \simeq 1 \text{ Jy arcsec}^{-1}$, resulting in excitation temperatures $T_{\text{ex}} \gtrsim 100 \text{ K}$. We note that, unfortunately, for the parameter space corresponding to our data, the inferred T_{ex} is very sensitive to uncertainties in the intensity ratio $R_{3/2}$, especially if overestimated (e.g., an overestimate of 15% in $R_{3/2}$ yields an overestimate of T_{ex} by a factor of 2.4). We note that these temperatures are significantly higher than the value of $T_{\text{ex}} = 25 \text{ K}$ previously obtained from much lower resolution ($20''$ - $30''$) data (Masson et al., 1990). This value was likely underestimated since our CO($3 \rightarrow 2$) images show intensity peaks of 80 mJy beam^{-1} , corresponding to brightness temperatures of $\sim 60 \text{ K}$. Since the CO($3 \rightarrow 2$) emission is not necessarily optically thick and/or does not completely fill the beam, this sets a lower limit of $\sim 60 \text{ K}$ to the excitation temperature, in agreement with the value inferred from the ratio of CO($3 \rightarrow 2$)/CO($2 \rightarrow 1$) intensities. Therefore, we adopt $T_{\text{ex}} = 100 \text{ K}$ in our calculations.

4.4.6 Column densities

The molecular column density can be obtained from the observation of a molecular transition following simple procedures. From the radiative transfer equation, the line intensity

towards a given position in the sky, and for a given LOS velocity, $I_\nu(x', y', v_{z'})$, is given by,

$$I_\nu(v_{z'}) = [B_\nu(T_{\text{ex}}) - B_\nu(T_{\text{bg}})] [1 - e^{-\tau_\nu(v_{z'})}], \quad (4.5)$$

where $B_\nu(T_{\text{ex}})$ is the source function, assumed to be constant along the LOS, $B_\nu(T_{\text{bg}})$ is the background intensity, and $\tau_\nu(v_{z'})$ is the LOS integrated optical depth as a function of the LOS velocity. For simplicity in the nomenclature, the explicit dependence on the position (x', y') has been omitted in this and the following equations.

From equation (4.5) we obtain:

$$\tau_\nu(v_{z'}) = -\ln \left[1 - \frac{I_\nu(v_{z'})}{B_\nu(T_{\text{ex}}) - B_\nu(T_{\text{bg}})} \right]. \quad (4.6)$$

The optical depth of a transition between the rotational levels $J \rightarrow J-1$ is related to the column density of molecules in the J level, as:

$$\frac{dN_J(v_{z'})}{dv_{z'}} = \frac{8\pi\nu_{J,J-1}^3}{c^3 A_{J,J-1}} \left(e^{h\nu_{J,J-1}/k_B T_{\text{ex}}} - 1 \right)^{-1} \tau_\nu(v_{z'}), \quad (4.7)$$

where c is the speed of light, h and k_B are the Planck's and Boltzmann's constants, $A_{J,J-1} = (64/3)\pi^4 c^{-3} h^{-1} J (2J+1)^{-1} \mu_{\text{mol}}^2 \nu_{J,J-1}^3$ is the Einstein spontaneous emission coefficient, μ_{mol} is the dipole moment of the molecule, $\nu_{J,J-1}$ is the frequency of the transition, $dN_J(v_{z'})$ is the column density of molecules in the upper level J per LOS velocity bin $dv_{z'}$, and $\tau_\nu(v_{z'})$ is given by equation (4.6).

To obtain the total column density of the molecular species considered, we have to add the populations of all the rotational levels, $N_{\text{mol}}(v_{z'}) = \sum_{j=0}^{\infty} N_j(v_{z'})$, that in LTE is given by:

$$N_{\text{mol}}(v_{z'}) = \frac{N_J(v_{z'})}{2J+1} e^{(J+1)h\nu_{J,J-1}/2k_B T_{\text{ex}}} Q(T_{\text{ex}}), \quad (4.8)$$

where $Q(T_{\text{ex}}) = \sum_{j=0}^{\infty} (2j+1) e^{-(j+1)h\nu_{j,j-1}/2k_B T_{\text{ex}}}$ is the partition function. Therefore, using equations (4.7) and (4.8), we obtain:

$$dN_{\text{mol}}(v_{z'}) = \frac{3hQ(T_{\text{ex}})}{8\pi^3 J \mu_{\text{mol}}^2} \frac{e^{(J+1)h\nu_{J,J-1}/2k_B T_{\text{ex}}}}{e^{h\nu_{J,J-1}/k_B T_{\text{ex}}} - 1} \tau_\nu(v_{z'}) dv_{z'}, \quad (4.9)$$

where $\tau_\nu(v_{z'})$ is given by equation (4.6). In practice, the observations are made with a finite angular resolution, so the measured intensities and, therefore, the derived column densities are indeed beam-averaged quantities. Note that beam dilution, because of a small beam filling factor, cannot be distinguished from a small optical depth. If the emission is truly optically thin a possible beam dilution does not affect the derived beam-averaged column density, but beam dilution would result in an underestimate of the column density if the emission is optically thick, since the opacity will be underestimated. In our analysis, we assume that the beam filling factor is ~ 1 in the $0.1''$ resolution observations, which we think is a good approximation except perhaps in the lower part of the rings where the emission can have a large optical depth and a small beam filling factor (see below).

If the emission is optically thin, we are in Rayleigh-Jeans regime, the background is negligible ($T_{\text{ex}} \gg T_{\text{bg}}$), and the partition function is approximated as $Q(T_{\text{ex}}) \simeq 2k_B T_{\text{ex}} / h\nu_{J,J-1}$, equation (4.9) simplifies as:

$$dN_{\text{mol}}(v_{z'}) \simeq \frac{3c^2 k_B T_{\text{ex}}}{8\pi^3 h\nu_{J,J-1}^4 \mu_{\text{mol}}^2} I_\nu(v_{z'}) e^{(J+1)h\nu_{J,J-1}/2k_B T_{\text{ex}}} dv_{z'}. \quad (4.10)$$

Although in our observations the emission is mostly optically thin, we will use in our calculations the complete equation (4.9).

Thus, from the CO ($J=3 \rightarrow 2$) observations, and using equation (4.9), we can obtain the beam-averaged CO column density, $N_{\text{CO}}(x', y', v_{\text{ch}}, \Delta v_{\text{ch}})$, associated with a given pixel with position (x', y') , in a channel map with central LOS velocity $v_{\text{ch}} = -v_{z'}$, and channel width $\Delta v_{\text{ch}} = |\Delta v_{z'}|$ as:

$$N_{\text{CO}}(x', y', v_{\text{ch}}, \Delta v_{\text{ch}}) = -\frac{hQ(T_{\text{ex}})}{8\pi^3 \mu_{\text{CO}}^2} \frac{e^{2h\nu_{32}/k_B T_{\text{ex}}}}{e^{h\nu_{32}/k_B T_{\text{ex}}} - 1} \ln \left[1 - \frac{I_\nu(\text{CO}(3-2); x', y', v_{\text{ch}})}{B_\nu(T_{\text{ex}}) - B_\nu(T_{\text{bg}})} \right] \Delta v_{\text{ch}}, \quad (4.11)$$

where μ_{CO} is the dipole moment of the CO molecule, and $I_\nu(\text{CO}(3-2); x', y', v_{\text{ch}})$ is the observed intensity of the CO ($J=3 \rightarrow 2$) transition toward the position considered.

4.4.7 Masses

We can estimate the mass associated to each pixel (x', y') in a given channel image of velocity v_{ch} as:

$$\Delta m(x', y', v_{\text{ch}}) = \mu_{\text{H}_2} m_{\text{H}} X_{\text{CO}}^{-1} D^2 N_{\text{CO}}(x', y', v_{\text{ch}}) \Delta x' \Delta y', \quad (4.12)$$

where X_{CO} is the CO abundance relative to molecular hydrogen, assumed to be 8.5×10^{-5} (Frerking et al., 1982), $\mu_{\text{H}_2}=2.8$ is the mean molecular mass per hydrogen molecule, and takes into account helium and metals that are heavier but less abundant than H₂ (Kauffmann et al., 2008), m_{H} is the mass of the hydrogen atom, D is the distance to the source, and $\Delta x'$ and $\Delta y'$ are the angular dimensions of a pixel in the image. $N_{\text{CO}}(x', y', v_{\text{ch}})$ is the column density of CO molecules that can be obtained from equation (4.11) using $T_{\text{ex}} = 100$ K, as inferred in the above section. The mass of a given family is obtained by adding the masses of the pixels identified as belonging to that family (in case of intersection of rings in a pixel, the mass is split between the corresponding families).

Using equation (4.12) we derived the masses of the ring families, obtaining 6.7×10^{-5} , 2.4×10^{-4} , 3.1×10^{-4} , 9.5×10^{-5} , and $4.0 \times 10^{-4} M_\odot$, for families I, II, III, IV, and VI, respectively. For family V, only a lower limit of $5.0 \times 10^{-7} M_\odot$ is given, corresponding to the mass of the rings that could be identified in the high resolution data. The head, that should appear at higher velocities, only available in the low resolution data, could not be identified in these data. We present these values of the mass, along with other properties of features associated with the SVS 13 outflow in Supplementary Information Table 1.

4.5 Summary and conclusions

Table 4.1. Compilation of properties of outflow features associated with SVS 13.

Object	Distance to VLA 4B ^a (arcsec)	Position angle ^b (deg)	LOS velocity ^c (km s ⁻¹)	Proper motion ^d (km s ⁻¹)	Inclination angle ^e (deg)	Dynamical time ^f (yr)	Ejection epoch ^g (Julian yr)	Mass ^h (M _⊙)	Refs.
Fe[II] jet	~ 0.2 ⁱ	145	-145 ± 5	...	22±3	4.2	2007.8	...	1
[OI]+[SII] jet	~ 0.3	145	2
H ₂ arc 1 (bubble)	0.654 ^j	145	...	19	22±3	< 32	> 1980	...	1
Rings I	0.94±0.08 ^k	144 ± 8	-104.7	25±5	1992±5	6.7×10 ⁻⁵	3
H ₂ arc 2	~ 1.5	162	~ 1950	...	1
Rings II	1.76±0.03 ^k	160.5±0.7	-96.7	...	25±2	56±6	1961±6	2.4×10 ⁻⁴	3
I-band cavity 1	1.9±0.1	162±2	2
Rings III	2.68±0.06 ^k	160.0±1.1	-89.9	...	25±2	91±9	1926±9	3.1×10 ⁻⁴	3
I-band cavity 2	2.8±0.1	156 ± 2	2
H ₂ arc 3	2.87	159	...	44	...	93±7	1919±7	...	1
Rings IV	3.19±0.01 ^k	155.2±0.4	-97.9	...	25±2	100±9	1917±9	9.5×10 ⁻⁵	3
Rings V	> 3.69 ^l	154.7±0.5	< -110.6	...	25±2	< 102	> 1915	> 5.0×10 ⁻⁷	3
CO clump 1	4.3	122.9	-15	...	25±2	860±80	1160±80	1.0×10 ⁻⁵	4
SiO knot	4.8	140	-36	5
CO clump 2	4.8	144.2	-33	...	25±2	440±40	1580±40	8.1×10 ⁻⁵	4
Rings VI	5.19±0.3 ^k	155.3±1.4	-117.2	...	25±2	134±15	1883±15	4.0×10 ⁻⁴	3
CO clump 3	7	150.2	-72	...	25±2	330±30	1690±30	4.3×10 ⁻⁵	4
Bullet 1	0.9-7	122.9-160.5	-125	...	19-27	20-940	1987-1080	1.2×10 ⁻³	3
Bullet 2	13.5	154	-141	350±30	1670±30	3.8×10 ⁻⁴	6, 7
Red bullet	16	14	+128	360±80	1660±80	3.1×10 ⁻⁴	6, 7
HH 11	17.7	132.2	-200	91±6	24±2	285±20	1733	...	2
Bullet 3	22	154	-162	420±40	1590±40	...	6, 7
HH 10	28.5	133.3	-77	< 6	2, 8
HH 9	36	107.7	-110	~ 0	2, 9
HH 8	43	130.0	-70	< 6	2, 8
HH 7	68	119.9	-80	38±7 ^m	25±5	2360±440	-342±440	...	2, 8
CO outflow blue lobe	122	120	~ -30	~ 10 ⁴	~ -10 ⁴	~ 1	10, 11
CO outflow red lobe	163	-40	~ +16	~ 10 ⁴	~ -10 ⁴	~ 2	10, 11

Note. — Parameters have been scaled to the assumed distance to the region of 300 pc (Ortiz-León et al., 2018).

^a Projected distance on the plane of the sky from VLA 4B to the object.

^b Position angle of the direction defined by the position of the object and VLA 4B.

^c Highest observed line-of-sight velocity relative to VLA 4B, for which a LSR velocity of +9.3 km s⁻¹ (Díaz-Rodríguez et al., 2022) has been assumed.

^d Plane-of-the-sky velocity derived from multiepoch observations.

^e Angle with respect to the line of sight. An inclination angle of 25 ± 2° has been assumed when its value is unknown.

^f Estimated from the deprojected speed and distance.

^g Epoch of the ejection, estimated from the dynamical time and the epoch of observation.

^h Estimated total mass of the object.

ⁱ Distance from VLA 4B to the end of the brightest part of the jet. The jet is detected up to a distance of ~0.36''.

^j Distance from VLA 4B to the apex of the bubble in 2012.

^k Distance from VLA 4B to the head of the family of rings.

^l Upper limit, corresponding to the more distant ring because the head has not been detected.

^m Corresponds to HH 7C.

References. — (1) Hodapp & Chini (2014); (2) Hartigan et al. (2019); (3) this work; (4) Blázquez-Calero et al., in preparation; (5) Lefèvre et al. (2017); (6) Bachiller et al. (2000); (7) Chen et al. (2016); (8) Solf & Boehm (1987); (9) Movsessian et al. (2000); (10) Snell & Edwards (1981); (11) Plunkett et al. (2013).

CHAPTER 5

MODELIZATION OF SVS 13 MOLECULAR JET

5.1 Introduction

Introduction to the modelization.

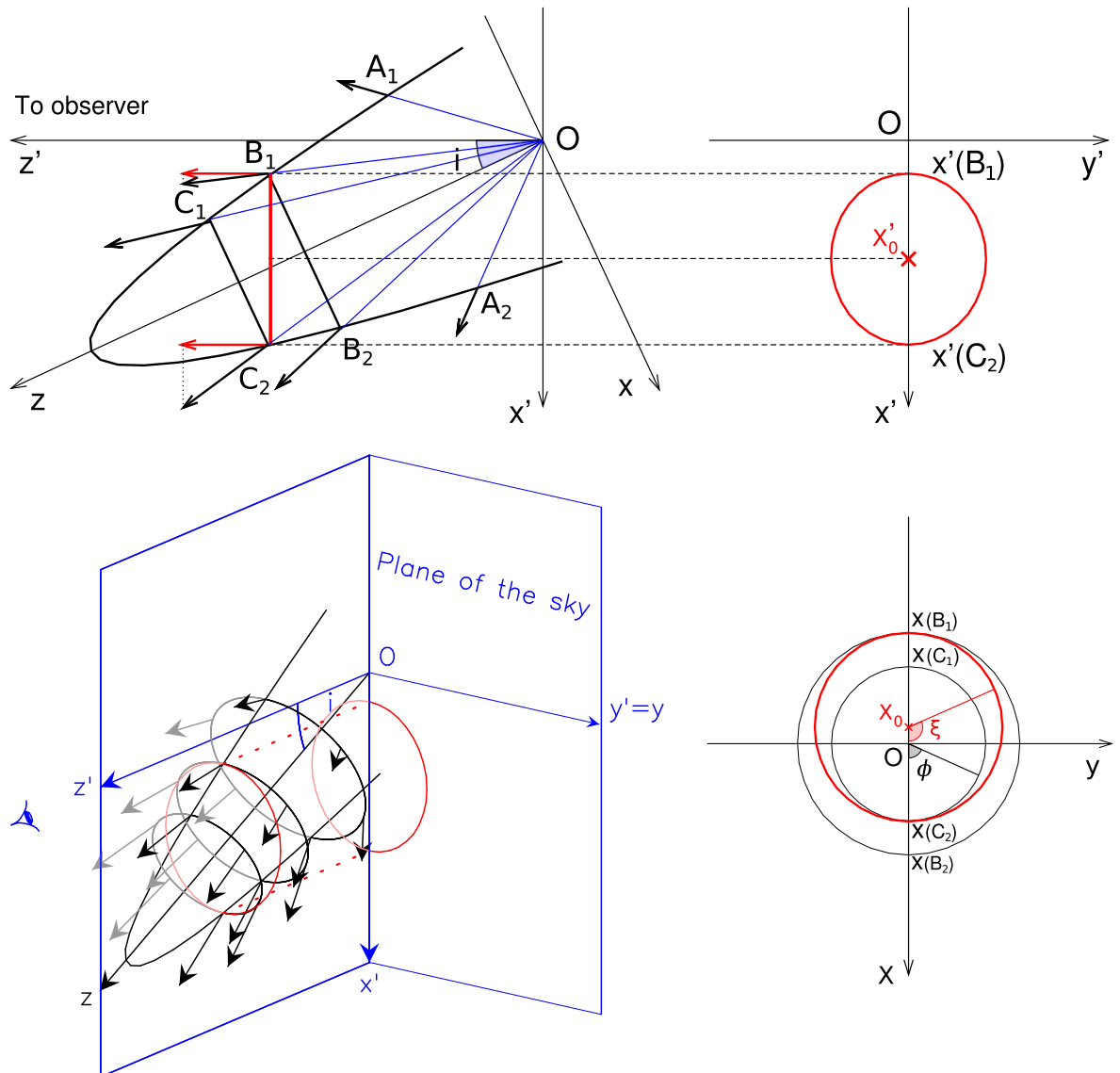
5.2 Analytical ballistic paraboloid model

A simple, purely geometrical model was developed to interpret the shape, size, and position of the rings observed in the velocity channel maps of the shells ejected by the young stellar object SVS 13. The model assumes two hypothesis: i) all the material in a given shell is ejected from the star (or from very near to it) at the same time, and moves ballistically in a purely radial direction, with a constant velocity equal to the velocity of ejection; and ii) the shape of the shell can be approximated by a paraboloid of revolution, symmetric about the flow axis.

5.2.1 Model parameters

We are considering the shell reference frame, with its origin at the position of the YSO, the z axis along the shell axis, the y axis perpendicular to z and on the plane of the sky, and the x axis perpendicular to both z and y . The shell axis has an inclination i with respect to the LOS. The observer reference frame has the same origin, with the z' axis along the LOS, toward the observer, the x' axis along the projection of the shell axis on the plane of the sky, and the y' axis coinciding with the y axis, so that the plane $x'y'$ is the plane of the sky (see Extended Data Fig. 3). Thus, the two coordinate systems are related by a rotation of angle i around the $y(=y')$ -axis, and the transformation between the two sets of coordinates is

$$\begin{cases} x' = x \cos i + z \sin i, \\ y' = y, \\ z' = z \cos i - x \sin i. \end{cases} \quad (5.1)$$



Extended Data Fig. 3: Geometry of the ballistic model. Geometrical scheme of a shell of ejected material and of the reference coordinate systems. The Cartesian coordinate system associated with the shell is (x, y, z) , where z is its symmetry axis. The coordinate system of the observer is (x', y', z') , where the z' -axis is the LOS, oriented at an inclination angle i from the z -axis, and the axes y and y' are coincident. The $x'y'$ -plane is the plane of the sky. The origin of coordinates for both systems is the position of the star. Thus, the two coordinate systems are related by a rotation of angle i around the $y(=y')$ -axis. **Top left:** Side view, where the coplanar axes x , x' , z , and z' -axes are contained in the plane of the page, while the $y(=y')$ -axis is perpendicular to it, coming out of the page. Because of the axial symmetry, the points with the same z have the same speed, which increases with z . The velocity vectors are represented by black arrows, where the pairs of points A_1 - A_2 , B_1 - B_2 , and C_1 - C_2 have the same speed (proportional to the arrow length). The plot illustrates the case of a paraboloidal shell. Due to projection and velocity gradient effects, points with different speeds can have the same LOS velocity component (e.g., points B_1 and C_2 , whose LOS velocity components are shown as red arrows). The set of points of the shell with a given LOS velocity component define an iso-LOS velocity curve (the one containing points B_1 and C_2 is shown in red). In the case of a paraboloidal shell formed by material ejected radially and simultaneously, the iso-LOS velocity curves are ellipses parallel to the plane of the sky (see Methods). **Top right:** Projection (shown in red) of the iso-LOS velocity curve onto the plane of the sky ($x'y'$ -plane). The projections of points B_1 and C_2 are labeled as $x'(B_1)$ and $x'(B_2)$. The point x'_0 is the center of the observed ring and corresponds to the projection of the center of the iso-LOS curve. In this plot, both the iso-LOS curve and its projection are ellipses. Note that the center of the iso-LOS curve does not fall on the symmetry axis of the shell (the z -axis) but slightly above it. **Bottom left:** Three-dimensional scheme of the ejected shell. The intersection of the shell with the $x'z'$ plane is shown as a black curve. Several cross-sections of the shell and their velocity vectors are plotted as black/gray ellipses and arrows, according to the positions of the points relative to the $x'z'$ -plane (black for points with $y'>0$ and gray for $y'<0$). An iso-LOS velocity curve and its projection onto the plane of the sky are shown in red. **Bottom right:** Projection of transverse sections of the shell onto the xy -plane, at two different heights (black circles), corresponding to the points B_1 , B_2 and C_1 , C_2 defined in the top left panel. The red curve is the projection onto the xy -plane of the iso-LOS velocity curve (a circle in the case of the aforementioned paraboloidal model, with center at $(x_0, 0)$; see Methods). The angle ϕ is the azimuthal angle in the shell coordinate system, with its origin in the star, while ξ is the angle measured from x , also contained in the xy -plane, but centered on x_0 .

The equation of the paraboloid can be written as

$$x^2 + y^2 = a^2 z_{\text{apex}} (z_{\text{apex}} - z), \quad (5.2)$$

for $0 \leq z \leq z_{\text{apex}}$, where z_{apex} is the location of the apex of the paraboloid, and a is a dimensionless parameter such that the radius of the paraboloid at $z = 0$ is $a z_{\text{apex}}$. The degree of collimation of the ejection increases with decreasing values of a . The shape of the shell depends on two parameters, the distance of the paraboloid apex from the YSO, z_{apex} , and the collimation parameter, a . A third parameter of the model is the time elapsed from the ejection, or dynamical time of the shell, t_{dyn} , which gives the relationship between velocities and distances from the YSO. In particular, the maximum ejection velocity, along the axis of the shell, v_{apex} , is given by

$$v_{\text{apex}} = \frac{z_{\text{apex}}}{t_{\text{dyn}}}. \quad (5.3)$$

5.2.2 Channel maps

The velocity of a channel map, v_{ch} , is the LOS velocity relative to the YSO as measured by the observer, and is defined positive when the motion is away from the observer (redshifted). However, the system of coordinates used has the z' axis directed toward the observer and, thus, positive $v_{z'}$ velocities are directed toward the observer (blueshifted). Therefore, there is a change of sign between v_{ch} and $v_{z'}$:

$$v_{\text{ch}} = -v_{z'} = -\frac{z'}{t_{\text{dyn}}}. \quad (5.4)$$

The observed image of the emission of the shell in a spectral channel with LOS velocity $v_{\text{ch}} = -v_{z'}$ will be an elliptical ring, corresponding to the projection onto the plane of the sky of the intersection of the shell with the iso-LOS velocity plane $z' = -v_{\text{ch}} t_{\text{dyn}}$. Since the iso-LOS velocity plane is parallel to the plane of the sky, the ellipse remains unchanged in this projection. The size of the elliptical rings decreases with increasing $v_{z'}$, and becomes zero for v_{tip} , the maximum value of $v_{z'}$, near (but not coinciding with) the apex of the shell. The centroid of the rings is located along the x' axis, at a distance x'_0 from the origin, increasing with increasing $v_{z'}$ (see Extended Data Fig. 3). In the following we will derive the shape, size, and position of these elliptical rings.

By using equation (5.1), the iso-LOS velocity plane $z' = -v_{\text{ch}} t_{\text{dyn}}$ transforms in

$$z = x \tan i - \frac{v_{\text{ch}} t_{\text{dyn}}}{\cos i}. \quad (5.5)$$

By substitution in the paraboloid equation, we obtain

$$(x - x_0)^2 + y^2 = r_c^2, \quad (5.6)$$

with

$$x_0 = -\frac{a^2 z_{\text{apex}}}{2} \tan i, \quad (5.7)$$

$$r_c^2 = a^2 z_{\text{apex}} \left[\frac{v_{\text{ch}} t_{\text{dyn}}}{\cos i} + z_{\text{apex}} \left(1 + \frac{a^2}{4} \tan^2 i \right) \right]. \quad (5.8)$$

Equations (5.5) and (5.6) are the equations of the iso-LOS velocity curve in the shell reference frame. Note that equation (5.6), which gives the projection onto the xy plane of this curve, is a circumference of center $(x_0, 0)$ and radius r_c . The parametric equations of the 3D coordinates of the intersection of the paraboloid and the iso-LOS plane can be obtained by using $x = x_0 + r_c \cos \xi$, $y = r_c \sin \xi$ (where $0 \leq \xi < 2\pi$ is the polar angle in the xy plane with respect to the x -axis), and equation (5.2), resulting:

$$\begin{cases} x = x_0 + r_c \cos \xi, \\ y = r_c \sin \xi, \\ z = z_{\text{apex}} - \frac{x^2 + y^2}{a^2 z_{\text{apex}}} = z_{\text{apex}} - \frac{x_0^2 + r_c^2}{a^2 z_{\text{apex}}} + r_c \tan i \cos \xi. \end{cases} \quad (5.9)$$

By using equation (5.1), the above equations can be transformed to the observer reference frame, obtaining their projection on the plane of the sky:

$$\begin{cases} x' = x'_0 + f r_c \cos \xi, \\ y' = r_c \sin \xi, \end{cases} \quad (5.10)$$

where r_c is given by equation (5.8) and

$$x'_0 = -v_{\text{ch}} t_{\text{dyn}} \tan i - \frac{a^2 z_{\text{apex}}}{2} \frac{\tan i}{\cos i}, \quad (5.11)$$

$$f = \frac{1}{\cos i} > 1. \quad (5.12)$$

Equations (5.10) are the parametric equations of an ellipse centered on $(x'_0, 0)$, with a semi-axis in the x' direction $f r_c$, a semi-axis in the y' direction r_c , and a longitudinal to transverse axial ratio $f = 1/\cos i$, which is a measure of the elongation factor of the ellipse. Since $f > 1$, the ellipse is elongated along the x' direction.

The maximum absolute value of the LOS velocity occurs at the tip of the shell, the point closest to the observer, near the apex. At this position the ring has zero size, $r_c = 0$, with a channel velocity

$$v_{\text{tip}} = -\frac{z_{\text{apex}} \cos i}{t_{\text{dyn}}} \left(1 + \frac{a^2}{4} \tan^2 i \right). \quad (5.13)$$

In terms of v_{tip} , the semi-minor axis of the elliptical ring can be given as

$$r_c^2 = a^2 z_{\text{apex}} \left(\frac{v_{\text{ch}} - v_{\text{tip}}}{\cos i} t_{\text{dyn}} \right). \quad (5.14)$$

5.2.3 Derivation of shell parameters from the observation

Let us assume that we measure, for several channel maps at different velocities v_{ch} , the position of the center of the rings, x'_0 , and their semi-minor axis, r_c . As can be seen from equations (5.11) and (5.14), there are linear relationships of x'_0 and r_c^2 with v_{ch} ,

$$x'_0 = p_x v_{\text{ch}} + q_x, \quad (5.15)$$

$$r_c^2 = p_r v_{\text{ch}} + q_r, \quad (5.16)$$

where the coefficients are

$$p_x = -t_{\text{dyn}} \tan i, \quad (5.17)$$

$$q_x = -b \frac{\tan i}{2 \cos i}, \quad (5.18)$$

$$p_r = b \frac{t_{\text{dyn}}}{\cos i}, \quad (5.19)$$

$$q_r = -b \frac{t_{\text{dyn}}}{\cos i} v_{\text{tip}}, \quad (5.20)$$

and, for simplicity, we used $b \equiv a^2 z_{\text{apex}}$. For a given inclination, there are four parameters (p_x , p_r , q_x , and q_r), but the independent parameters that define the shape and kinematics of the shell are three, t_{dyn} , v_{tip} , and b (equivalent to t_{dyn} , z_{apex} , and a).

A simple way of fitting the three independent parameters is to note that the independent term q_x is much smaller than the others. Its physical interpretation is the position of the center of the rings extrapolated to $v_{\text{ch}} = 0$, and should be near zero. Thus, an iterative procedure, can be performed, beginning with $q_x = 0$. At each step, the fits $x'_0 - q_x = p_x v_{\text{ch}}$ (with q_x fixed) and $r_c^2 = p_r v_{\text{ch}} + q_r$ (equations (5.15) and (5.16)) are calculated, and q_x is recalculated (using equations (5.17)-(5.19)) as $q_x = (p_r/2p_x) \tan^2 i$. The process converges easily to values of p_x , p_r , and q_r consistent with q_x . Once the best fit values of p_x , p_r , and q_r are obtained, the shell parameters are derived (equations (5.11) and (5.14)) as

$$t_{\text{dyn}} = -\frac{p_x}{\tan i}, \quad (5.21)$$

$$v_{\text{tip}} = -\frac{q_r}{p_r}, \quad (5.22)$$

$$b = -\frac{p_r}{p_x} \sin i. \quad (5.23)$$

The rest of parameters of the shell are derived (equation (5.13)) as

$$z_{\text{apex}} = -\frac{v_{\text{tip}} t_{\text{dyn}}}{\cos i} - \frac{b}{4} \tan^2 i = -\frac{p_x q_r}{p_r \sin i} + \frac{p_r}{4p_x} \sin i \tan^2 i, \quad (5.24)$$

$$a = \sqrt{\frac{b}{z_{\text{apex}}}}, \quad (5.25)$$

$$v_{\text{apex}} = \frac{z_{\text{apex}}}{t_{\text{dyn}}}. \quad (5.26)$$

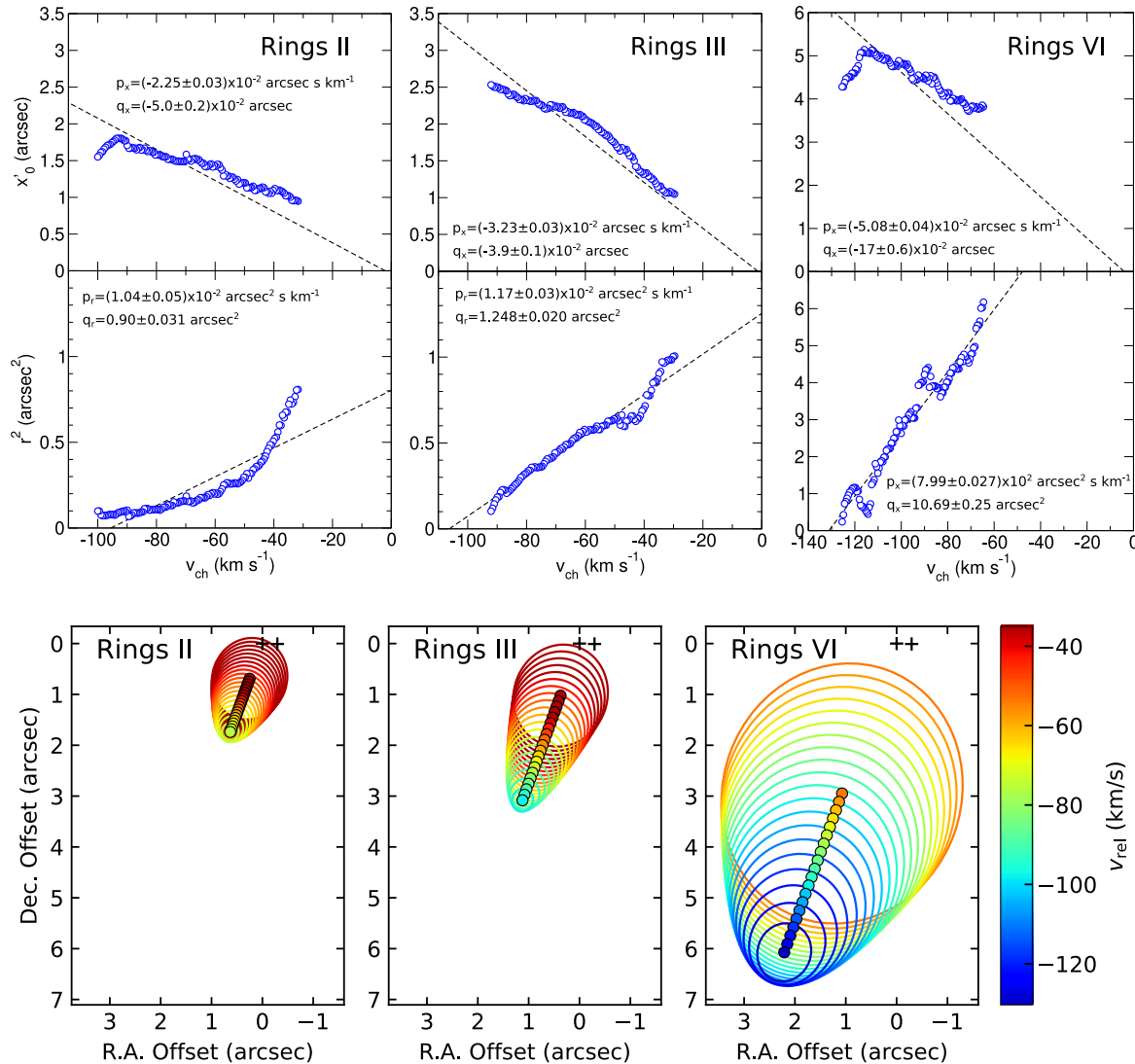


Figure 5.1 Results of the paraboloidal shell model fitting. Plots of the results of the fitting of a geometrical model consisting of a paraboloidal shell of material ejected simultaneously from the source, moving radially at constant velocity (see Methods). An inclination angle $i = 25^\circ$ is adopted (see Methods). **Top:** Position of the center, x'_0 , and radius squared, r^2 , of the rings as a function of the velocity relative to the source of the channel map, v_{ch} , for families of rings II, III, and VI. **Bottom:** Projection of the (elliptical) iso-LOS velocity curves onto the plane of the sky, for different color-coded LOS velocities (relative to the source), corresponding to the best-fit model parameters. We obtain deprojected velocities at the apex $v_{\text{apex}} = 95.3 \pm 5.8, 116.9 \pm 4.0, 146.3 \pm 6.2 \text{ km s}^{-1}$; dynamical times $t_{\text{dyn}} = 68.5 \pm 0.8, 98.4 \pm 0.8$, and $155.2 \pm 1.1 \text{ yr}$; and values of the parameter that controls the degree of collimation (see equation (5.2)) $a = 0.206 \pm 0.008, 0.138 \pm 0.003$, and 0.204 ± 0.006 , for families of rings II, III, and VI, respectively.

5.2.4 Application to SVS 13

Top panels of Extended Data Fig. 4 show the plots of the positions of the center of the rings, x'_0 , and square of radii, r_c^2 , versus the LOS velocity relative to the source, v_{ch} , for the families of Rings II, III, and VI. The rings are almost circular, implying that the inclination is small. For the inclination angle adopted, $i = 25^\circ$, the axial ratio expected is $f = 1/\cos i = 1.10$, compatible with the values measured for the rings. It is remarkable that, in general, the position of the rings and the square of their radii depend roughly linearly on the channel velocity, as predicted by the model. The plot also shows the consistent linear fits to the data, which fit pretty well the observations. The fit parameters obtained (p_x , p_r , q_x , and q_r) are shown in the top panels of Extended Data Fig. 4. The parameters of the paraboloid shell for each family have been obtained from the fit parameters in the way explained above, and are listed in the caption of Extended Data Fig. 4. We obtain deprojected velocities at the apex, $v_{\text{apex}} = 95.3 \pm 5.8$, 116.9 ± 4.0 , and $146.3 \pm 6.2 \text{ km s}^{-1}$, and dynamical times of the shell, $t_{\text{dyn}} = 68.5 \pm 0.8$, 98.4 ± 0.8 , and $155.2 \pm 1.1 \text{ yr}$, for Rings II, III, and VI, respectively.

5.3 Ballistic deprojection

Here we describe a procedure to obtain the 3D morphology and kinematics of an arbitrarily shaped axisymmetric ballistic shell from the observed sizes, positions and LOS velocities of the respective ring family.

Let us consider a one-sided, relatively collimated, ejection of particles distributed in a thin shell observed at an inclination angle i (see Extended Data Fig. 3). We assume that the shell of ejected material is axisymmetric, but with an arbitrary smooth shape. We further assume that all the material has been ejected radially from the proximity of the protostar, over a range of time and velocity, and that each particle moves ballistically with a constant velocity. Therefore, the position and velocity vectors of each particle in the shell are proportional, where the proportionality factor is the time elapsed since its ejection, t_{dyn} . We adopt the same shell and observer reference frames than in the “Paraboloid-shell model” section (see Extended Data Fig. 3), so the transformation between the two frames is given by equations (5.1), where $x'y'$ is the plane of the sky, the z' axis is along the LOS, and z along the shell axis.

Because the shell is geometrically thin and with axial symmetry, all the points with a given value of z are located at the same distance, r , from the z -axis. Other geometrical and kinematical properties of the shell can also be written as a function only of z . Therefore, for the deprojection, it is convenient to relate the Cartesian coordinates (x', y', z') of the points of the shell in the observer reference frame and their Cylindrical coordinates (r, ϕ, z) in the shell reference frame, where $\phi = \arctan(y/x)$ is the azimuthal angle with origin in the x -axis. From equations (5.1), and taking into account that $x = r \cos \phi$ and $y = r \sin \phi$,

we obtain:

$$x' = x \cos i + z \sin i = r \cos \phi \cos i + z \sin i, \quad (5.27)$$

$$y' = y = r \sin \phi, \quad (5.28)$$

$$z' = z \cos i - x \sin i = z \cos i - r \cos \phi \sin i. \quad (5.29)$$

Note that, in practice, the only directly measurable lengths are the coordinates x' and y' , in the plane of the sky, but not z' , along the LOS.

We can also use equations (5.1) to relate the Cartesian components of the velocity in the reference frames of the observer and the shell. Furthermore, given that the velocity and the position vector for any point of the shell have the same direction (and, therefore, they transform in the same way), we can write:

$$v_{x'} = v_x \cos i + v_z \sin i = v \sin \theta \cos \phi \cos i + v \cos \theta \sin i, \quad (5.30)$$

$$v_{y'} = v_y = v \sin \theta \sin \phi, \quad (5.31)$$

$$v_{z'} = v_z \cos i - v_x \sin i = v \cos \theta \cos i - v \sin \theta \cos \phi \sin i, \quad (5.32)$$

where v is the speed, and $\theta = \arctan(r/z)$ and ϕ (defined above) are the polar and azimuthal angles, respectively, of the position vector in the shell reference frame (see Extended Data Fig. 3). Note that the only measurable velocity in our spectral line observations is $v_{z'}$, the velocity projected onto the LOS z' (i.e., $v_{z'} = -v_{\text{ch}}$, where v_{ch} is the velocity of the channel map). Nevertheless, a second epoch of observation could potentially provide measurements of $v_{x'}$ and $v_{y'}$ through proper motions in the plane of the sky.

Therefore, equations (5.27), (5.28), and (5.32) relate the measurable parameters in the channel maps and the parameters of the shell. For a given value of z , these equations are simplified when $\phi = \pi/2$ (the same result is obtained taken $\phi = 3\pi/2$, because of symmetry), resulting:

$$z = \frac{x'_{\pi/2}}{\sin i}, \quad (5.33)$$

$$r = y'_{\pi/2}, \quad (5.34)$$

$$v = \frac{v_{z'} \sqrt{r^2 + z^2}}{z \cos i}, \quad (5.35)$$

where $x'_{\pi/2}$ and $y'_{\pi/2}$ are the Cartesian coordinates in the observer reference frame of the point of the shell with $\phi = \pi/2$ and projected velocity $v_{z'}$.

For a given value of z , the point $(x'_{\pi/2}, y'_{\pi/2})$ is the one with the largest value of y' , which coincides with the radius, r , of the cross-section of the shell at z , as this transverse distance remains unaffected by the projections. However, it should be noted that an observed channel map is the image of the points of the shell that have the same projected LOS velocity $v_{z'} = -v_{\text{ch}}$, where v_{ch} is the central velocity of the channel map, and these points correspond to a range of values of v and z in the 3D shell. Since the radius of the shell changes with z (in general, increases as z decreases), the point in a channel map with the largest value of y' , in general does not correspond exactly to $\phi = \pi/2$ and $z = x'_{\pi/2}/\sin i$.

Therefore, in general, the observations only provide approximate coordinates of the point with $\phi = \pi/2$, and equations (5.33) and (5.34) are only used approximately. In general, the agreement will be better the smaller the variation of the shell radius with z , i.e., it would be a good approximation for a well-collimated shell. For the paraboloid-shell with a single ejection time discussed before (see ‘Paraboloid-shell model’ section) the curves of equal LOS velocity are ellipses contained in planes parallel to the plane of the sky. However, the centers of these ellipses do not fall exactly onto the z axis (see Extended data Fig. 3) but, at a position $(x'_0, 0)$ with $x'_0 < z \sin i$. For the paraboloidal shell case, x'_0 can be calculated (equation (5.11)) and it can be shown that the shift is $\ll r/2$, except for points very close to the apex ($z_{\text{apex}} - z \lesssim r$). In the general case discussed here, the shell is axisymmetric but the ejection of the whole shell does not necessarily occur simultaneously, thus the iso-LOS velocity curves are not necessarily contained in planes perpendicular to the LOS axis z' , and the projections of the iso-LOS velocity curves onto the $x'y'$ -plane (the plane of the sky) are symmetric with respect to the x' -axis, but not necessarily elliptical. Nevertheless, our observations show that the observed rings in the channel maps can be fitted pretty well as ellipses, and we use the fitted positions of the centers of the ellipses, x'_0 , their transverse semi axes, $r_{y'}$, and the velocity of the observed channel maps, $-v_{\text{ch}}$, as our estimates for $x'_{\pi/2}$, $y'_{\pi/2}$, and v_z in equations (5.33), (5.34), and (5.35). We expect the degree of accuracy to be similar to the paraboloid case, and therefore that the deprojection is accurate, except very close to the head of the shell. Therefore, by fitting ellipses to the observed rings in the channel maps the deprojected structure of the shell, $r(z)$ and $v(z)$, can be obtained and tabulated as a function of z . We can also obtain the polar angle of the points in the shell reference system as:

$$\theta(z) = \arctan\left(\frac{r}{z}\right). \quad (5.36)$$

Finally, since the particles are assumed to move in straight lines and with constant velocity, we can obtain the dynamical time as:

$$t_{\text{dyn}}(z) = \frac{\sqrt{r^2 + z^2}}{v}, \quad (5.37)$$

where $r(z)$ and $v(z)$, can be taken from the tabulated values that are obtained using equations (5.34) and (5.35). Since all points with a given value of z have the same values of r and v , all will also have the same dynamical time.

In order to relate the derived properties of the ejected shell with the observed emission, additionally to the global shell structure, we will derive the z -coordinate corresponding to every pixel of the observed rings. In this way, we will be able to relate the intensity of the observed CO(3-2) emission in the channel maps with the 3D kinematical and geometrical properties (e.g., $v(z)$, $r(z)$, $t_{\text{dyn}}(z)$) of the location in the shell where this emission was originated. From equation (5.32), assuming $i \neq 0$, the azimuthal angle ϕ and z are related by the following equation:

$$\cos \phi = \frac{1}{\tan \theta \tan i} + \frac{v_{\text{ch}}}{v \sin \theta \sin i}. \quad (5.38)$$

Substituting equation (5.38) into equation (5.27), we obtain:

$$x' = r \left(\frac{1}{\tan \theta \tan i} + \frac{v_{\text{ch}}}{v \sin \theta \sin i} \right) \cos i + z \sin i. \quad (5.39)$$

And, after some algebra, we get

$$x' = \frac{z}{\sin i} + \frac{v_{\text{ch}} \sqrt{r^2 + z^2}}{v \tan i}, \quad (5.40)$$

or, as a function of the dynamical time,

$$x' = \frac{z}{\sin i} + t_{\text{dyn}} \frac{v_{\text{ch}}}{\tan i}. \quad (5.41)$$

Given a value of x' measured in a ring image observed in a channel map with LOS velocity $v_{z'} = -v_{\text{ch}}$, we can use the tabulated function $t_{\text{dyn}}(z)$ to obtain the values of z and t_{dyn} that satisfies equation (5.41). Once the value of z is obtained, all the properties of this point of the shell can be obtained from the tabulated values derived from the global deprojection of the shell.

We note that the deprojection procedure described above is valid for a geometrically thin axisymmetric shell, and is useful for deprojecting the emission over most of the shell extent. For points far enough from the source or that lie very close to the z -axis (e.g., near the head of the shell), so $\theta(z) \approx 0$, the deprojection can be performed simply in terms of the inclination angle i (see also the section on dynamical times of the heads in Methods),

$$v_{\text{head}}(z) \approx -\frac{v_{\text{ch}}}{\cos i}, \quad (5.42)$$

and then,

$$z \approx \frac{x'_{\text{head}}}{\sin i}. \quad (5.43)$$

In this way, the emission near the head, which spreads over filled circles and cannot be treated as geometrically thin rings, can be approximately deprojected using these equations.

5.3.1 Mass loss rate in the ballistic model.

In the framework of the ballistic model (Extended Data Fig. 3) we assume that the observed emission corresponds to material directly ejected from the disk or the close environment of the star. We assume that the ejected material is distributed in a thin shell with axial symmetry around the outflow axis z . The direction of the velocity is radial from the origin. Therefore, the points with the same magnitude of the velocity, v , have the same polar angle, θ , and they are located at the same distance from the origin, $z/\cos \theta$. Thus, they are distributed as circles perpendicular to the outflow direction. These circles would have the same dynamical time. However, these circles of common total velocity do not directly correspond to the elliptical rings observed in images of velocity channels, which correspond to points with the same projected velocity along the LOS ($v_{z'}$). A ring with the same

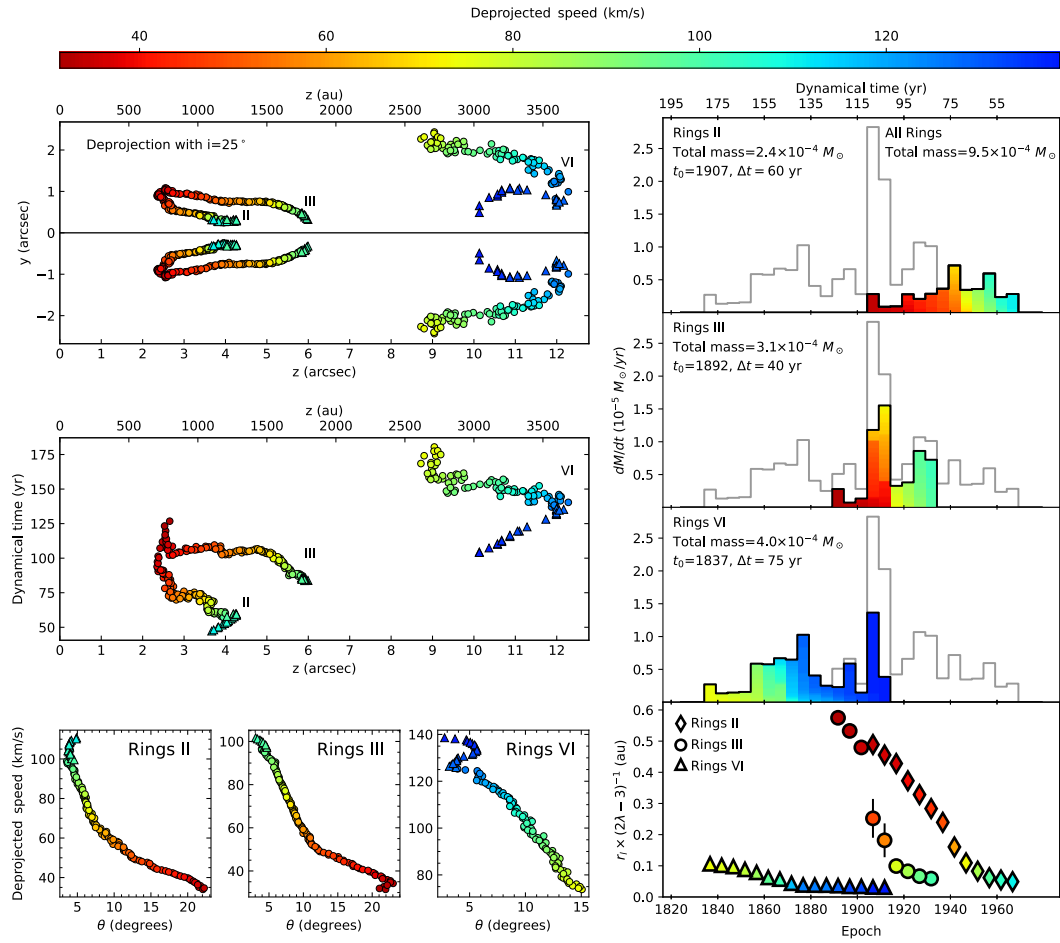


Figure 5.2 Results of the ballistic deprojection of the observations. Plots resulting from the morphological and kinematical deprojection of the observed families of rings II, III, and VI, assuming an inclination angle $i = 25^\circ$ (see Methods). In all panels, the color represents the deprojected velocity. In the left panels color dots indicate the centers of the rings and triangles the regions of filled emission (heads). **Top left panel:** Deprojected morphology of the shells, showing the cylindrical radius, y , as a function of distance to the origin along the symmetry axis, z . **Middle left panel:** Dynamical time as a function of z . **Bottom left panels:** Deprojected velocity as a function of the polar angle θ , defined as the angle of the position vector with respect to the symmetry axis of the shell. **Right panels:** Mass loss history of SVS 13 from epoch 1830 to 1970 in Julian years, with epoch 2000 corresponding to the standard definition of Julian epoch J2000.0. The first three panels (from top to bottom) show the mass-loss rate separated in three ejection events, with a similar pattern of increasing mean speed with time, that are associated with three of the observed families of rings. Data are binned in 5 yr intervals. The color scale indicates the velocity range of the material included in each bin. The bottom right panel shows the estimated launch radius, in the context of a magneto-centrifugal disk wind, as a function of time for every event (see Methods).

projected velocity is actually composed of points with different total velocities. Above we developed a procedure to deproject the ring images in the observed channel maps. Equation (5.41) relates the x' coordinate of a point in the ring image in a given channel map (with $v_{z'} = -v_{\text{ch}}$) with its corresponding z -coordinate and dynamical time in the ejecta, while equation (4.12) provides an estimate of the mass corresponding to every pixel in the image. So, in principle, we can obtain a mass and a dynamical time for every pixel in the observed images. Because of the finite angular resolution, the rings in the observed images will have a finite width, with emission extending over several pixels. Since we are assuming that the shell is geometrically thin, these rings are narrow and, in practice, we built an annular mask around the observed ring images and will add the masses of all the pixels in the selected region that have the same value of x' , and assign to all of them the same dynamical time using equation (4.12). In this way, after scanning all the observed velocity channels, and splitting in dynamical time bins, we can obtain the mass loss history as the accumulated mass in each bin as a function of dynamical time, as shown in Extended Data Fig. 5. In these plots, the color code of the temporal bins indicates the mass-weighted mean velocity of the particles within that bin. We note that, in the high angular resolution data, it is possible that the mass of the highest velocity rings is incomplete, since the emission of some parts could have LOS velocities falling outside the observed bandwidth.

5.4 Bowshock model

The shape of the bowshock wings is determined by the interaction of the material ejected sideways by the working surface (with a velocity v_0 and mass rate \dot{m}_0) with the streaming ambient material (which impinges on the jet head with a density ρ_{amb} and velocity $v_{\text{jet}} - v_{\text{amb}}$, see Extended Data Fig. 7). We assume that the jet material (ejected sideways by the working surface) and the entrained ambient material form a stationary, well mixed thin shell. This shell has a locus $r_b(x^*)$ (see Extended Data Fig. 7) that results from the mass and (x^*, r) -momentum conservation equations:

$$\dot{m} = \dot{m}_0 + \pi r_b^2 \rho_{\text{amb}} (v_{\text{jet}} - v_{\text{amb}}) = 2\pi r_b \sigma v_t , \quad (5.44)$$

$$\dot{\Pi}_{x^*} = \pi r_b^2 \rho_{\text{amb}} (v_{\text{jet}} - v_{\text{amb}})^2 = \dot{m} v_{x^*} , \quad (5.45)$$

$$\dot{\Pi}_r = \dot{m}_0 v_0 = \dot{m} v_r , \quad (5.46)$$

where \dot{m} , $\dot{\Pi}_{x^*}$ and $\dot{\Pi}_r$ are the mass, x^* -momentum and r -momentum rates flowing along the thin shell up to a given value of x^* , and v_t , v_{x^*} and v_r are the components of the velocity of the well mixed material within the shell along the shell surface, and along the x^* - and r -axes, respectively. Finally, σ (see the last term of equation (5.44)) is the surface density of the thin shell.

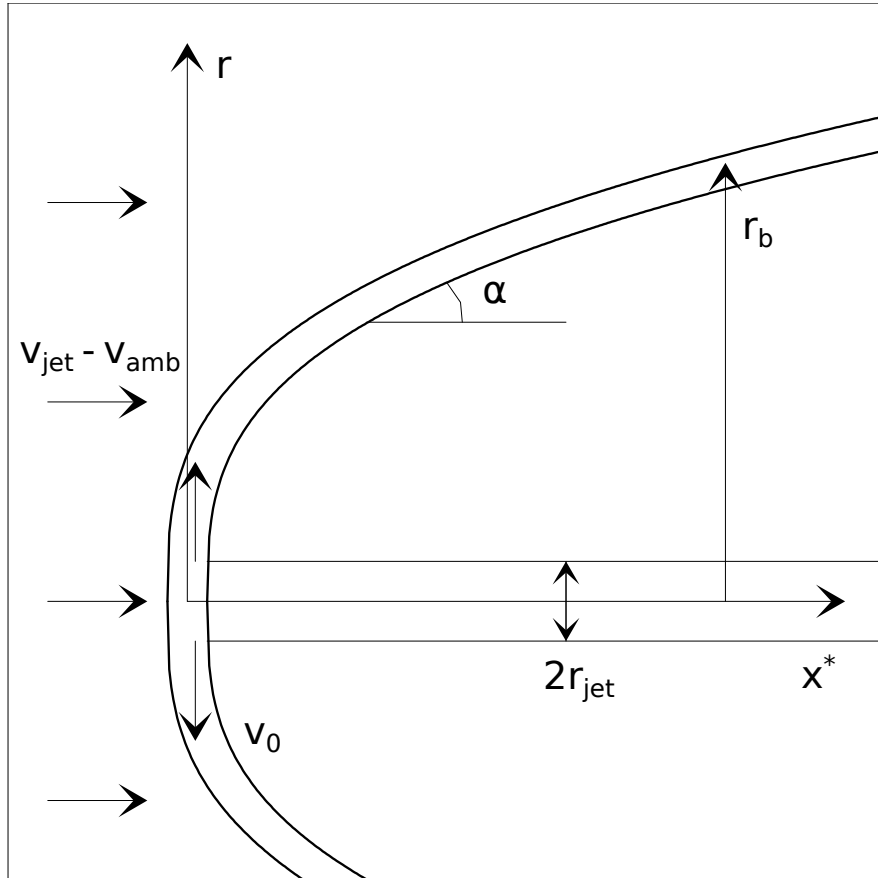


Figure 5.3 Extended Data Fig. 7: Schematic diagram of the thin shell bowshock model. The bowshock is seen in a reference system moving at the velocity v_{jet} of the working surface. The cylindrical jet beam (of diameter $2r_{\text{jet}}$) stops in the working surface, as it interacts with the impinging ambient gas (moving to the right at a velocity $v_{\text{jet}} - v_{\text{amb}}$). We show a cylindrical coordinate system (x^*, r) , where r is the cylindrical radius and x^* the distance measured from the head of the working surface towards the outflow source. The working surface ejects material sideways at a velocity v_0 (which is approximately equal to the post-cooling region sound speed of $\sim 10 \text{ km s}^{-1}$). This sideways ejection interacts with the impinging ambient gas, forming a thin shell bowshock that has a well defined locus $r_b(x^*)$, and locally has a slope $\tan \alpha = dr_b/dx^*$.

$$v_{x^*} = \frac{\pi r_b^2 \rho_{\text{amb}} (v_{\text{jet}} - v_{\text{amb}})^2}{\dot{m}_0 + \pi \rho_{\text{amb}} (v_{\text{jet}} - v_{\text{amb}}) r_b^2}, \quad (5.47)$$

$$v_r = \frac{\dot{m}_0 v_0}{\dot{m}_0 + \pi \rho_{\text{amb}} (v_{\text{jet}} - v_{\text{amb}}) r_b^2}. \quad (5.48)$$

One then combines these two equations to obtain the differential equation:

$$\frac{dr_b}{dx^*} = \tan \alpha = \frac{v_r}{v_{x^*}} = \frac{\dot{m}_0 v_0}{\pi r_b^2 \rho_{\text{amb}} (v_{\text{jet}} - v_{\text{amb}})^2}, \quad (5.49)$$

where α is the angle between the jet axis and the local tangent to the bow surface. Equation (5.49) can be directly integrated to obtain the shape of the bowshock wings:

$$r_b(x^*) = (L_0^2 x^*)^{1/3}, \quad (5.50)$$

with

$$L_0 \equiv \sqrt{\frac{3 \dot{m}_0 v_0}{\pi \rho_{\text{amb}} (v_{\text{jet}} - v_{\text{amb}})^2}}. \quad (5.51)$$

The free parameters of the model are: (i) the size scale L_0 of the bowshock (see equation (5.51)), (ii) v_{jet} and v_{amb} (the velocities of the jet head and of the medium into which it is travelling), (iii) v_0 (the velocity at which the jet material is ejected sideways by the internal working surface), and (iv) the inclination angle i of the outflow direction with respect to the LOS.

Each family of rings is assumed to trace a bowshock whose parameters are obtained as those of the model that best matches the properties of the elliptical fits to the observed rings in the channel maps, in terms of mean ring radius and relative LOS velocity as a function of projected distance to the source on the plane of the sky, x' . For the best defined families of rings, we obtain $L_0 = 0.38''$, $v_0 = 20 \text{ km s}^{-1}$, $v_{\text{jet}} = 110 \text{ km s}^{-1}$ (Rings II); $L_0 = 0.50''$, $v_0 = 17 \text{ km s}^{-1}$, $v_{\text{jet}} = 109 \text{ km s}^{-1}$ (Rings III); and $L_0 = 1.80''$, $v_0 = 25 \text{ km s}^{-1}$, $v_{\text{jet}} = 133 \text{ km s}^{-1}$ (Rings VI). In all cases, $i = 20^\circ$ and $v_{\text{amb}} \approx 0 \text{ km s}^{-1}$ (see Fig. 5.4 and Extended Data Table 1).

5.4.1 Derivation of the density of the ambient gas and mass rates

The density of the ambient gas, ρ_{amb} , can be estimated from the mass of the bowshock shell, M (i.e., the mass of a given family of rings), which can be measured from the observations (see “Determination of the mass” in Methods). Once ρ_{amb} is known, the mass rate of jet material initially ejected sideways by the working surface, \dot{m}_0 , and the mass rate of ambient material being incorporated, \dot{m}_{amb} , can be derived.

In the narrow jet regime ($r_{\text{jet}} \ll L_0$), the mass of the shell can be obtained by integrating the mass rate flowing along the shell, $\dot{m} = \dot{m}_0 + \dot{m}_{\text{amb}}$ (equation (5.44)), over the whole

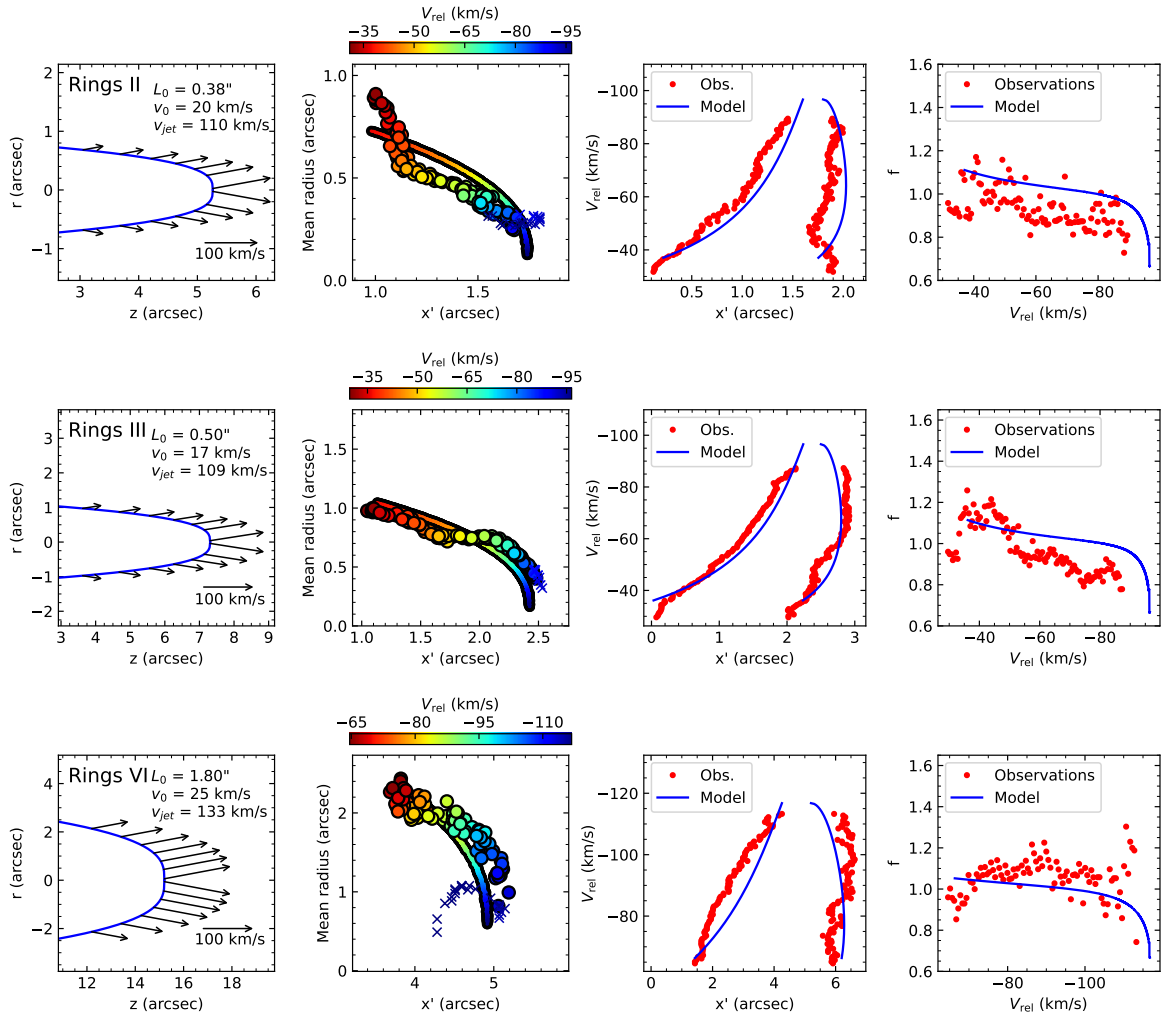


Figure 5.4 Comparison of the bowshock model results with the elliptical fits to the observations. The rows correspond to families II, III and VI, respectively, from top to bottom. **First column:** Depiction of the shape and velocity field of the bowshock model, where z is the symmetry axis (whose origin is VLA 4B) and r is the cylindrical radius of the bowshock. The main parameters of the model, the characteristic scale (L_0), the velocity at which the jet material is initially ejected sideways by the working surface (v_0), and the velocity of the internal working surface along the z -axis (v_{jet}), are listed in the top right corner of the panels. The distance from the source to the internal working surface (z_{ws}) is taken as the position of the head of the family. In all cases, the inclination angle is $i = 20^\circ$, and the velocity of the medium into which the jet is traveling is $v_{amb} \approx 0 \text{ km s}^{-1}$ (see Methods and Extended Data Table 1). **Second column:** Observed (dots indicate rings and x symbols indicate filled emission of the head) and model (continuum line) bowshock radius as a function of the projected distance to VLA 4B. Velocities are indicated in a color scale. **Third column:** Observed (red dots) and model (blue line) position-velocity diagram for the rings (excluding the heads). **Fourth column:** Observed (red dots) and model (blue line) elongation factor of the rings (f), taken as the ratio of the ring axes along the longitudinal and transverse directions. All velocities are LOS velocities relative to the velocity of VLA 4B. Additional plots of the angle between the position vector and the symmetry axis predicted by the models are shown in Extended Data Fig. 6.

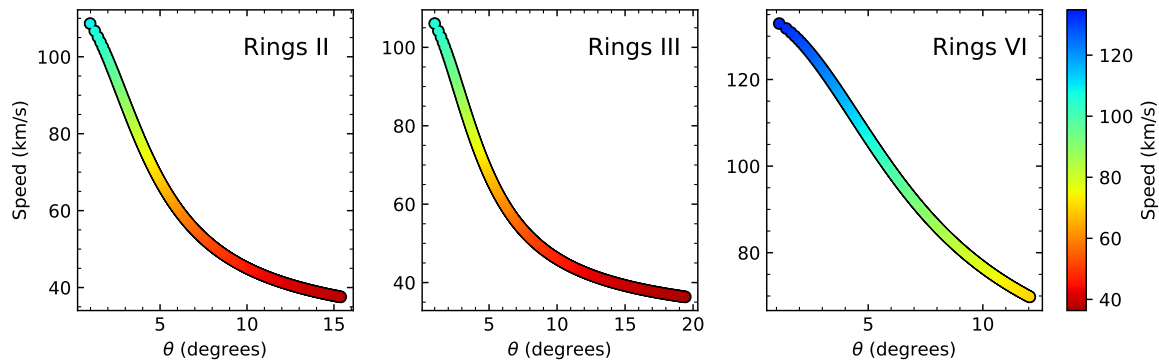


Figure 5.5 Extended Data Fig. 6: Velocity as a function of polar angle for the bowshock model. Speed of the bowshock material as a function of the polar angle, θ , defined as the angle of the position vector with respect to the symmetry axis of the shell, z , for families II, III, and VI. An inclination angle $i = 20^\circ$ is assumed for all the plots. The model parameters for families II, III, and VI are presented in Extended Data Table 1. Note that the bowshock model naturally explains the increase of velocity near the symmetry axis.

lifetime of the bowshock:

$$M = \int_{t_0}^{t_f} \dot{m} dt = \int_0^{r_f} \dot{m} \frac{dr_b}{v_r}, \quad (5.52)$$

where $t_f - t_0$ is the time elapsed since the bowshock was originated, $v_r = dr_b/dt$, and $r_f \equiv r_b(t_f)$ is the observed maximum radius, corresponding to the outer edge of the bowshock shell.

From the conservation of r -momentum, given by equation (5.46), we have

$$v_r = \frac{\dot{m}_0 v_0}{\dot{m}}, \quad (5.53)$$

and substituting in equation (5.52), we obtain

$$M = \int_0^{r_f} \frac{\dot{m}^2}{\dot{m}_0 v_0} dr_b. \quad (5.54)$$

From the definition of L_0 (equation (5.51)), the mass conservation equation (equation (5.44)) can be written as:

$$\dot{m} = \dot{m}_0 \left[1 + \frac{3}{\gamma} \left(\frac{r_b}{L_0} \right)^2 \right], \quad (5.55)$$

with

$$\gamma \equiv \frac{v_{\text{jet}} - v_{\text{amb}}}{v_0}, \quad (5.56)$$

and substituting in equation (5.54),

$$M = \int_0^{r_f} \frac{\dot{m}_0}{v_0} \left[1 + \frac{3}{\gamma} \left(\frac{r_b}{L_0} \right)^2 \right]^2 dr_b. \quad (5.57)$$

Using the change of variable $u = (3/\gamma)^{1/2}(r_b/L_0)$ and resolving the integral:

$$M = \frac{\dot{m}_0 L_0}{v_0} \left(\frac{\gamma}{3} \right)^{1/2} \int_0^{u_f} (1+u^2)^2 du = \frac{\dot{m}_0 L_0}{v_0} \left(\frac{\gamma}{3} \right)^{1/2} \left(\frac{u_f^5}{5} + \frac{2u_f^3}{3} + u_f \right), \quad (5.58)$$

where $u_f = (3/\gamma)^{1/2}(r_f/L_0)$.

Combining equation (5.51) and (5.56), we can calculate the density of the ambient medium, ρ_{amb} , as a function of the mass of the shell, M , as:

$$\rho_{\text{amb}} = M \left[3\pi \left(\frac{\gamma}{3} \right)^{5/2} L_0^3 \left(\frac{u_f^5}{5} + \frac{2u_f^3}{3} + u_f \right) \right]^{-1}. \quad (5.59)$$

Note that, when $r_f \gg L_0$ ($u_f \gg 1$), ρ_{amb} can be approximated as:

$$\rho_{\text{amb}} \simeq M \left[3\pi \left(\frac{\gamma}{3} \right)^{5/2} L_0^3 \left(\frac{u_f^5}{5} \right) \right]^{-1} = \frac{5}{3\pi} \frac{M L_0^2}{r_f^5}. \quad (5.60)$$

Once we have an estimate of ρ_{amb} , we can calculate from equation (5.55) the mass rate contribution of the jet to the bowshock, \dot{m}_0 , as:

$$\dot{m}_0 = \rho_{\text{amb}} \frac{\pi(v_{\text{jet}} - v_{\text{amb}})^2 L_0^2}{3v_0}, \quad (5.61)$$

and the contribution of the ambient gas, \dot{m}_{amb} , to the mass rate of mixed jet+ambient material flowing along the bowshock up to a radius r_b , is given by:

$$\dot{m}_{\text{amb}} = \pi\rho_{\text{amb}}(v_{\text{jet}} - v_{\text{amb}})r_b^2. \quad (5.62)$$

Note that, from equations (5.61) and (5.62), the ratio of the jet mass rate to the ambient mass rate up to a given radius r_b is given by

$$\frac{\dot{m}_0}{\dot{m}_{\text{amb}}} = \frac{\gamma}{3} \left(\frac{L_0}{r_b} \right)^2, \quad (5.63)$$

so only the tip of the bowshock, where $r_b < L_0(\gamma/3)^{1/2}$, is dominated by ejected jet material.

Evaluating equation (5.62) at the maximum radius of the shell, r_f , we can obtain the mass rate of ambient material incorporated to the whole bowshock:

$$\dot{M}_{\text{amb}} = \pi\rho_{\text{amb}}(v_{\text{jet}} - v_{\text{amb}})r_f^2. \quad (5.64)$$

From the bowshock parameters and the observed mass of each family, M (see above section in Methods and extended Data Table 1), ρ_{amb} , \dot{m}_0 , and \dot{M}_{amb} can be obtained from equations (5.59), (5.61), and (5.64), respectively. The results are shown in Extended Data Table 1. We obtain densities $\rho_{\text{amb}} = 4.6 \times 10^{-19}$, 2.2×10^{-19} , and 2.2×10^{-20} g cm⁻³ for Rings II, III, and VI, respectively. Thus, we derive decreasing values of ρ_{amb} with distance from the source (Rings II are the closest to the source of the three families, and Rings VI are the farthest), which is physically consistent with the source being an embedded object, located in the central, denser region of a molecular core.

We obtain $\dot{m}_0 = 1.4 \times 10^{-6}$, 1.2×10^{-6} , and 1.7×10^{-6} M_{\odot} yr⁻¹ for Rings II, III, and VI. Taking \dot{m}_0 as a good estimate of the mass-loss rate of the jet, we infer $\dot{M}_{\text{jet}} = 1-2 \times 10^{-6}$ M_{\odot} yr⁻¹. It is worth noting that, since the mass accretion rate inferred for VLA 4B is $\dot{M}_{\text{acc}} = 0.8-1.3 \times 10^{-5}$ M_{\odot} yr⁻¹ (see Methods), we obtain an ejection to accretion ratio of $\dot{M}_{\text{jet}}/\dot{M}_{\text{acc}} \simeq 0.1$, consistent with the typical value in outflows.

Regarding the mass rate of ambient material that is incorporated into the bowshock, we obtain $\dot{M}_{\text{amb}} = 2.9 \times 10^{-6}$, 2.4×10^{-6} , and 1.6×10^{-6} M_{\odot} yr⁻¹ for Rings II, III, and VI, respectively. Also, we see that, while for Rings II and III $\dot{M}_{\text{amb}} \simeq 2\dot{m}_0$, for Rings VI we obtain $\dot{M}_{\text{amb}} \simeq \dot{m}_0$. Since Rings VI are the most distant, it seems possible that this decrease in the relative contribution of the ambient gas to the bowshock mixed material is a consequence of the observed decrease in the surrounding ambient density, ρ_{amb} , with distance. Nonetheless, for Rings VI, the rings with largest radii are faint and difficult to identify, so we could be missing a significant part of the mass that is predominantly composed by ambient material.

5.4.2 Calculation of the emission of the channel maps

Finally, we consider that the velocity along the thin shell can be written as $v_t = v_{x^*} \cos \alpha + v_r \sin \alpha$, and use equations (5.44) and (5.47)-(5.49) to calculate the surface density of the shell as

$$\sigma = \frac{1}{2} \rho_{\text{amb}} \cos \alpha (\gamma \tan \alpha + 1)^2 r_b , \quad (5.65)$$

with

$$\cos \alpha = \left(1 + \frac{L_0^4}{9r_b^4} \right)^{-1/2} , \quad (5.66)$$

$$\tan \alpha = \frac{1}{3} \left(\frac{L_0}{r_b} \right)^2 , \quad (5.67)$$

We then have a full solution giving the shape (equation (5.50)), velocity (equations (5.47) and (5.48)) and surface density (equation (5.65)) for a thin shell bowshock flow. In practice, a thermal+turbulent velocity dispersion, v_T , is expected to be present so that the surface density is spread over a range of velocities, which is taken into account when calculating the distribution in velocity channels. In our case, we find a 3D velocity dispersion $v_T \simeq 2 \text{ km s}^{-1}$, which corresponds to a LOS velocity dispersion of $\simeq 1.2 \text{ km s}^{-1}$.

Once we know the shape of the bowshock shell, with the velocity and surface density at all its points, we can obtain their projected positions on the plane of the sky and their LOS velocities. In this way, we can assign each point of the shell to a pixel in a given channel map of width Δv_{ch} , obtaining the mass and column density for each of the pixels of the model channels. From the CO column density, obtained through its abundance relative to H₂, we can derive the CO optical depth and intensity predicted by the model using equations (4.9) and (4.5), respectively. Finally, channel maps directly comparable with observations can be simulated by convolving the intensities with the appropriate beam.

Family	L_0 (arcsec)	v_0 (km s $^{-1}$)	v_{jet} (km s $^{-1}$)	z_{ws} (arcsec)	M (M_\odot)	ρ_{amb} (g cm $^{-3}$)	\dot{m}_0 (M_\odot yr $^{-1}$)	\dot{M}_{amb} (M_\odot yr $^{-1}$)
II	0.38	20	110	5.26	2.4×10^{-4}	4.6×10^{-19}	1.4×10^{-6}	2.9×10^{-6}
III	0.50	17	108	7.31	3.1×10^{-4}	2.2×10^{-19}	1.2×10^{-6}	2.4×10^{-6}
VI	1.80	25	132	14.61	4.0×10^{-4}	2.2×10^{-20}	1.7×10^{-6}	1.6×10^{-6}

Table 5.1 **Bowshock model parameters for families of Rings II, III, and VI.** L_0 is the characteristic scale, v_0 the initial velocity at which jet material is ejected sideways, v_{jet} the velocity of the working surface, z_{ws} the position of the head of the family, M the mass measured from the observations, ρ_{amb} the density of medium into which the jet is traveling, \dot{m}_0 the mass-rate of jet material ejected sideways by the internal working surface, and \dot{M}_{amb} the mass-rate of ambient material that is incorporated into the bowshock shell. In all cases, the inclination angle is $i = 20^\circ$, and the velocity of the ambient medium is $v_{\text{amb}} \simeq 0$ km s $^{-1}$. The adopted distance is $D = 300$ pc (Ortiz-León et al., 2018; Gaia Collaboration et al., 2023).

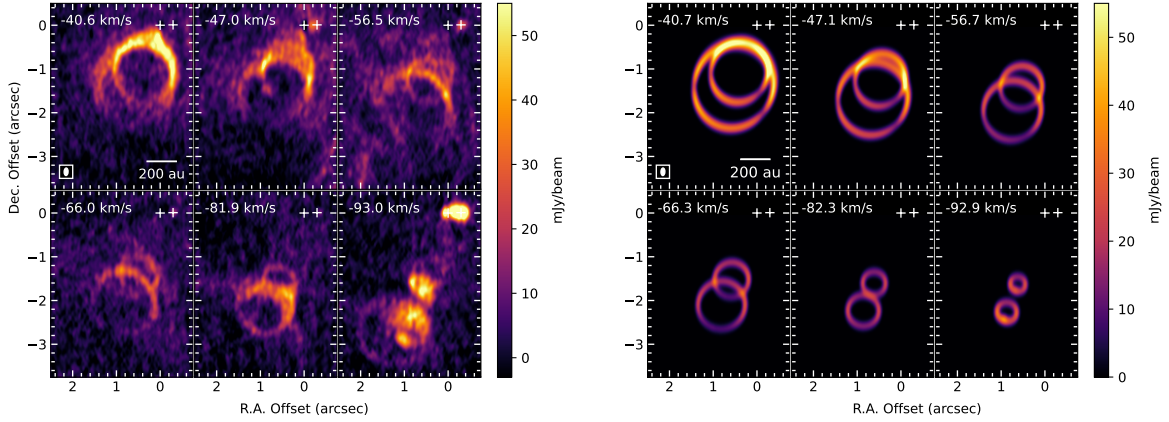


Figure 5.6 Comparison of observed and bowshock model spectral channel images. Comparison of a set of observed (left) and bowshock model (right) spectral channel images corresponding to ring families II (the northernmost) and III (the southernmost), which are the two families with the best observational data. The model parameters are given in Fig. 5.4 and Extended Data Table 1. The model images have been calculated for a channel width $\Delta v_{\text{ch}} = 0.53 \text{ km s}^{-1}$ (the same as in the observed images), assuming an intrinsic velocity dispersion (thermal+turbulent) $v_T = 2 \text{ km s}^{-1}$ (see Methods). Offsets are relative to the position of VLA 4B (the easternmost of the two components of SVS 13, indicated by white plus signs). The LOS velocity relative to VLA 4B is indicated in the top left corner of each channel image.

5.5 Opacity and ring asymmetry

An outstanding feature of the observed rings is that, in general, they appear brighter in the side closer in projection to the origin. This is reproduced by the bowshock model, and can be understood in terms of opacity and beam filling-factor effects due to the geometry of the bowshock relative to the observer, as illustrated in Extended Data Fig. 8.

As shown in the figure (left and central panels in top row), because of the geometry and orientation of the SVS 13 bowshocks with respect to the observer, the emission at a given LOS velocity (i.e., from a given channel map) appears spread over a wide region in the side of the ring closer in projection to the origin (smaller values of x'). In the opposite side of the ring (larger values of x'), the emission appears projected over a very narrow arcuate region, resulting in a higher intensity (and optical depth) in the emitting pixels (see left panel in the middle row). If the emission was optically thin all over the ring, the flux in each of these two regions would be the same, and the image of the ring would appear symmetric (except for a local effect due to the elongation of the beam; e.g. Osorio et al. 2016) when convolved with a finite beam (see central panel in the middle row), since the decrease in beam filling-factor due to the smaller number of emitting pixels in the narrow emitting region will be fully compensated by the increase in intensity. However, if the effects of optical depth, τ , are taken into account, the intensity toward a given line of sight is lower by a factor of $[1 - \exp(-\tau)]/\tau$ with respect to the optically thin regime. When the emission is convolved with a finite beam an asymmetry is produced because the emission in the extended region fills the beam better than in the part of the ring farthest from the origin where the total flux density is lower and distributed in a narrow region (see left and central panels in the bottom row). The last column in the figure includes noise in the model images (middle and bottom) for a more realistic comparison with the observations (top).

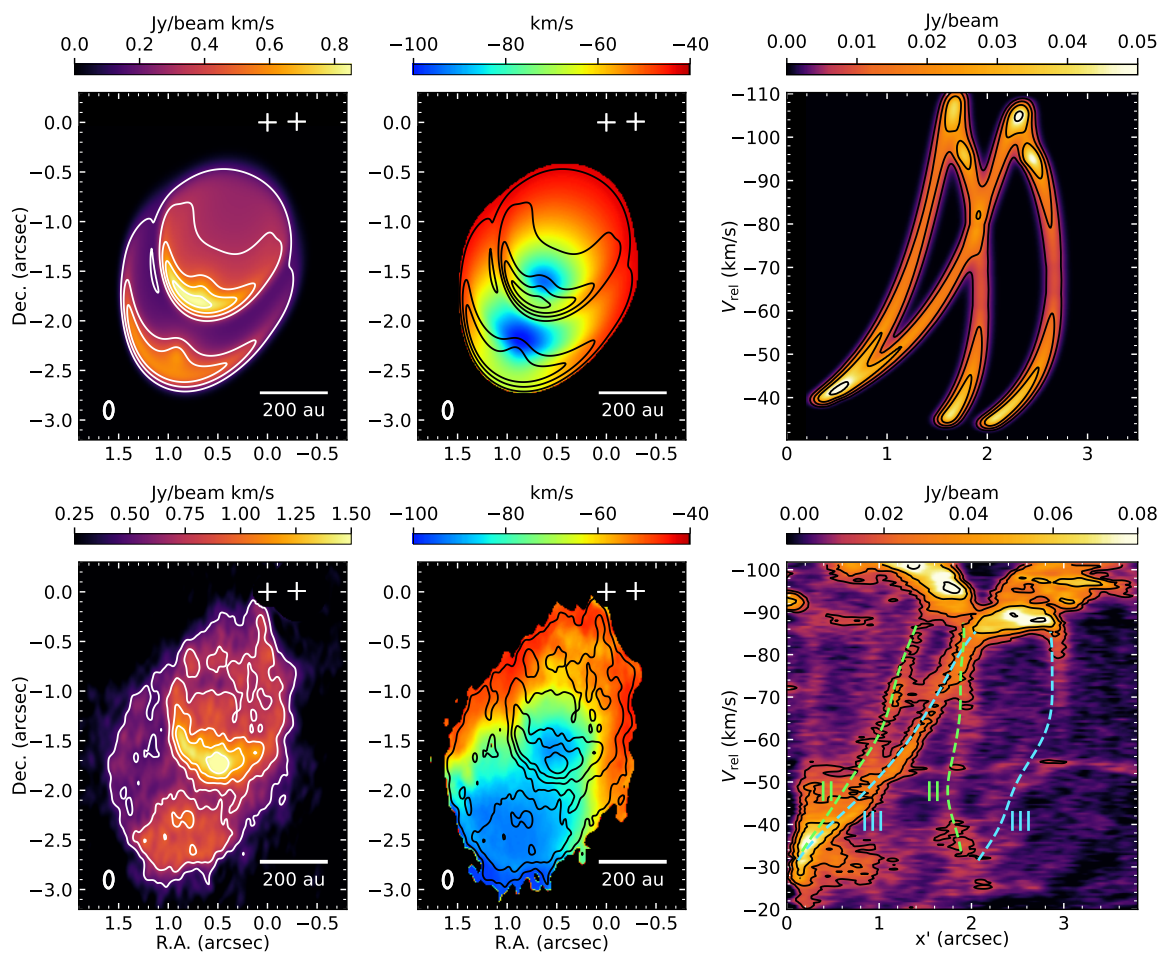
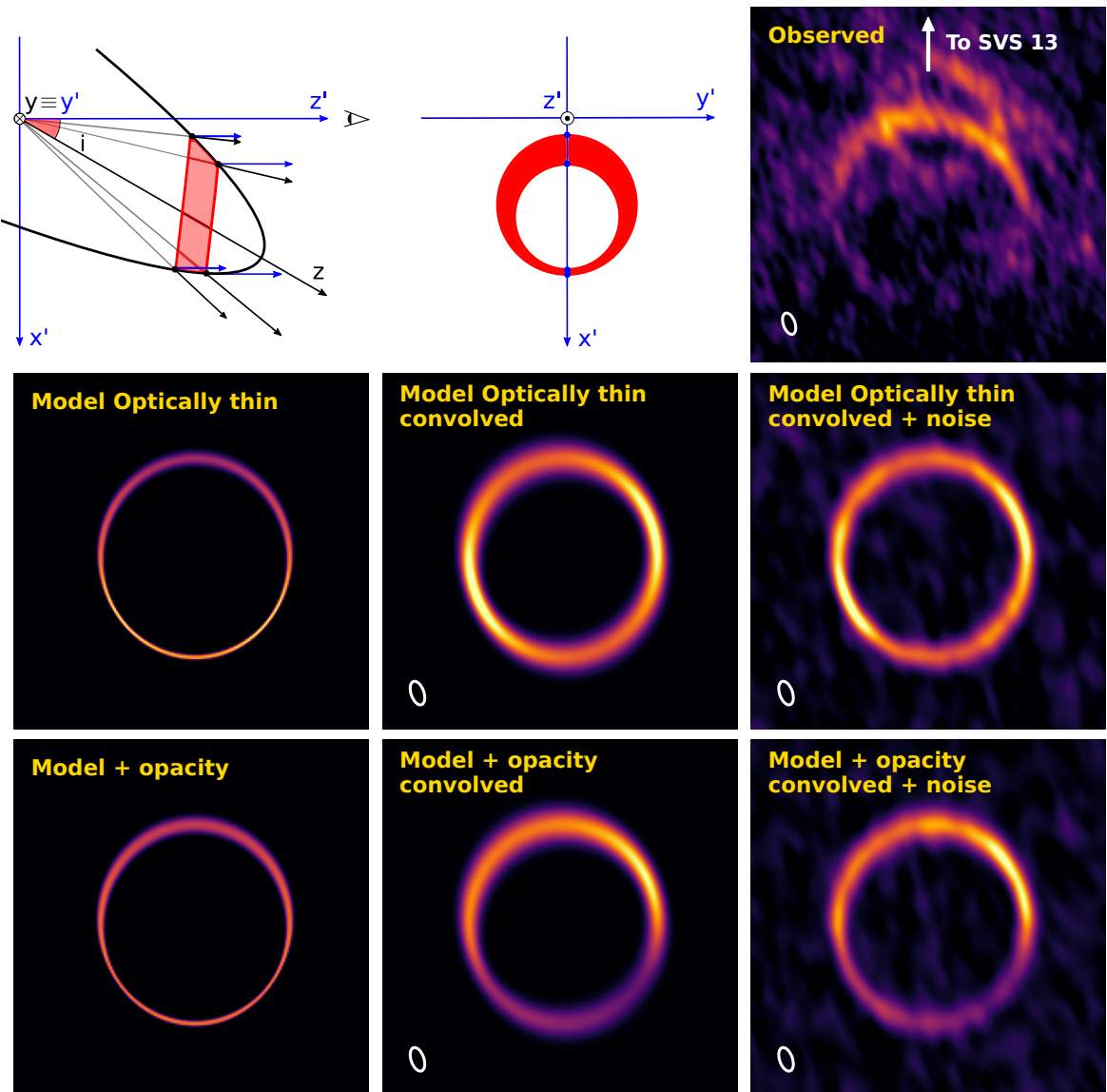


Figure 5.6 Comparison of the bowshock model with the observed moment images and position-velocity diagrams. Comparison of bowshock model (top panels) and observed (bottom panels) zeroth- and first-order moment images, and position-velocity diagrams. The model results correspond to the bowshock model for the families of rings II and III, whose parameters are given in Fig. 5.4 and Extended Data Table 1. The LOS velocity range used for model calculations goes from -41.6 to -112.0 km s^{-1} . The observational results correspond to the LOS velocity range where the emission of these two families is dominant, from -41.6 to -100.8 km s^{-1} relative to VLA 4B. Nevertheless, some emission from family I is present within $0.5''$ southeast from VLA 4B. The disk emission has been masked in the observed moment images. Yet, the observed emission is stronger than that of the model, since the observations cannot completely isolate the emission from families II and III, and it is likely to include emission from other features. Contour levels in the zeroth-order moments are 4, 6, 8, 10, and 12 times $0.12 \text{ Jy beam}^{-1} \text{ km s}^{-1}$ for the observations, and 2, 4, 6, 8, and 10 times $0.08 \text{ Jy beam}^{-1} \text{ km s}^{-1}$ for the model images. The channel width is 0.53 km s^{-1} . The positions of the components of the SVS 13 binary, VLA 4A (west) and VLA 4B (east), are indicated by white plus signs. The contour levels of the position-velocity diagrams ($\text{PA} = 160^\circ$, width = $0.1''$) are 5, 10, 20, and 35 times $2.5 \text{ mJy beam}^{-1}$ for the observations, and 2, 5, 10, and 20 times $2.5 \text{ mJy beam}^{-1}$ for the model. Dashed lines in the observed position-velocity diagram indicate the emission from families II and III.



Extended Data Fig. 8: Effect of the optical depth on the observed emission of the rings. **Top left:** Geometry of the bowshock shell, where the black vectors show the shell velocity, the blue vectors show their projections onto the LOS, and the shaded band outlines the spatial extent of the emission in the velocity range of a given channel map. **Top center:** Sketch of the corresponding image. The finite range of velocities in the channel maps, makes the ring images to appear with a finite width. Because of the geometry and inclination angle, the emission spreads over a wider area in the sky in the half of the ring closer in projection to the star, while the opposite half of the ring (positions with larger projected distance to the origin) appears narrower because the same range of LOS velocities arises from a much smaller projected area with overlapping lines of sight. **Top right:** Observed channel image illustrating the asymmetry of the rings in SVS 13, with the side of the ring closest in projection to the star (top of the image) appearing brighter and wider than the opposite side. The image has been rotated so the upper side faces SVS 13. **Middle row:** Model images of optically thin rings. At low optical depths, in the upper part of the ring (the side closest to SVS 13 in projection) the emission appears spread over a wider range of radii, and with lower intensity, than in the lower part, where the emitting region is narrower but with higher intensity (left). When convolved with the beam (center), the intensity becomes almost uniform throughout the ring, except for a local increase in intensity near the positions where the beam axis is tangent to the ring, which is a well-known effect due to the variation in the beam filling factor when a narrow ring is observed with an elongated beam Osorio et al. (2014). When noise is added (right), no substantial asymmetries are detected. **Bottom row:** Model images of optically thick rings. When the optical depth is high enough (left), the emission at the top of the ring becomes almost as bright, but more extended, than at the bottom, where intensity increases are hindered by opacity saturation. When convolved with the beam (center), the intensity drops in the lower (narrower) part of the ring, where the beam filling factor is smaller, producing an asymmetry similar to that observed. Inclusion of noise in the model (right) results in remarkable agreement with observations (top right). The assumed velocity dispersion (v_T) is 2 km s^{-1} , and the assumed channel width is 0.53 km s^{-1} in all models.

CHAPTER 6

SUMMARY AND CONCLUSIONS

The conclusions are

6.1 Future work

APPENDIX A

SVS 13 CHANNEL MAPS FROM ALMA OBSERVATIONS

APPENDIX B

CALCULATION OF MODEL SPECTRAL CUBES

In this appendix we present the methodology followed in order to compute the spectral cube of a model. This methodology can be applied for any axisymmetric model whose morphology (given by z and $r(z)$), kinematics (given by $v_z(z)$ and $v_r(z)$), and surface density $\sigma(z)$ is known. In the case of the bowshock model, the morphology is given by equation (5.50), its kinematics by equations (5.47) and (5.48), and the surface density by equation (5.65). The model shape should be projected into the plane of the sky $x'y'$ using the equations (5.1), while the velocity onto the line of sight velocity $v_{z'}$ with equation (5.32), assuming an inclination angle i between the line of sight and the z axis.

The first step in order to calculate the spectral cube is to grid the space (both the plane of the sky $x'y'$ and the LOS velocity $v_{z'}$):

$$(x', y', v_{z'}) \rightarrow (x'_i, y'_i, -v_{\text{ch}}) \quad (\text{B.1})$$

taking into account sizes of the cells in $\Delta x'$, $\Delta y'$, and Δv_{ch} . The mass in each cell is given by

$$m(x'_i, y'_i, v_{\text{ch}}) = \int_0^{2\pi} \int_{r_{\text{jet}}}^{r_f} W_{\text{cube}}(x'_i, y'_i, v_{\text{ch}}, r, \phi) \sigma(r) \frac{r dr d\phi}{\sin \alpha(r)} \quad (\text{B.2})$$

where $\alpha(r)$ is the angle between the z axis and the shell surface at r and $W_{\text{cube}}(x'_i, y'_i, v_{\text{ch}}, r, \phi)$ is the weight associated to the cell with spectral cube coordinates $(x'_i, y'_i, v_{\text{ch}})$. W_{cube} can be decompose into the weights of each spectral cube dimension (i.e., $W_{x'}$, $W_{y'}$, and W_{ch}) as:

$$\begin{aligned} W_{\text{cube}}(x', y', v_{\text{ch}}, r_b, \phi) = \\ W_{x'}(x'_i - x'(r_b, \phi)) W_{y'}(y'_i - y'(r_b, \phi)) W_{\text{ch}}(v_{\text{ch}} + v_{z'}(r_b, \phi)) \end{aligned} \quad (\text{B.3})$$

We choose different weightings schemes for the sky coordinates (x' and y' dimensions) and the spectral dimension. For x' and y' dimensions, the weighings W depend on the maximum number of nearest grid points n to which the particle is weighted, and for $n = 2$ we have the often called cloud in cell (CIC) scheme:

$$W_{x'}(x'_i - x'(r_b, \phi)) = \begin{cases} 1 - \frac{|x'_i - x'(r, \phi)|}{\Delta x} & \text{if } |x'_i - x'(r, \phi)| < \Delta x' \\ 0 & \text{if } |x'_i - x'(r, \phi)| \geq \Delta x' \end{cases} \quad (\text{B.4})$$

$$W_{y'}(y'_i - y'(r, \phi)) = \begin{cases} 1 - \frac{|y'_i - y'(r, \phi)|}{\Delta y} & \text{if } |y'_i - y'(r, \phi)| < \Delta y' \\ 0 & \text{if } |y'_i - y'(r, \phi)| \geq \Delta y' \end{cases} \quad (\text{B.5})$$

On the other hand, for the velocity axis, we use the following Gaussian kernel:

$$W_{\text{ch}}(v_{\text{ch}} + v_{z'}(r, \phi)) = e^{-\left(\frac{v_{\text{ch}} + v_{z'}(r, \phi)}{v_{T,z'}}\right)^2} \frac{\Delta v_{\text{ch}}}{\sqrt{\pi} v_{T,z'}}, \quad (\text{B.6})$$

where $v_{T,z'}$ is the one dimensional thermal+turbulent velocity dispersion along the LOS. Once we have the mass in each cell of the spectral cube through equation (B.2), we can calculate its intensity of a line assuming the excitation properties and performing the radiative transfer. For our bowshock model, we assumed LTE conditions to simulate the CO emission and used equations (4.9) and (4.5) for the radiative transfer.

APPENDIX C

DETERMINATION OF FLUX DENSITY AT THE CENTRAL FREQUENCY OF A BAND

Let's suppose that the flux density of a source follows a power law. We measure the flux density of this source using a band with an initial and final frequencies ν_0 and ν_f . The flux density at any frequency, ν , as a function of the central frequency of the band, ν_c , is,

$$S_\nu(\nu) = S_\nu(\nu_c) \left[\frac{\nu}{\nu_c} \right]^\alpha \quad (\text{C.1})$$

The flux density that is measured is the flux density averaged over the whole frequency coverage, $\overline{S}_\nu(\nu)$,

$$\overline{S}_\nu(\nu) = \frac{1}{\nu_f - \nu_0} \int_{\nu_0}^{\nu_f} S_\nu(\nu) d\nu = S(\nu_c) \frac{2^\alpha (\nu_f^{\alpha+1} - \nu_0^{\alpha+1})}{(\nu_f - \nu_0)(\nu_f + \nu_0)^\alpha (\alpha + 1)} \quad (\text{C.2})$$

If $\nu_f = q\nu_0$,

$$\frac{\overline{S}_\nu(\nu)}{S_\nu(\nu_c)} = \left(\frac{2}{q+1} \right)^\alpha \frac{(q^{\alpha+1} - 1)}{(q-1)(\alpha+1)} \quad (\text{C.3})$$

In figure C.1, the ratio of the measured flux density and the flux density at the central frequency of the band is plotted as a function of α , for several values of q . For $\alpha = 0.5$ and $q = 2$, $\overline{S}_\nu(\nu) \approx S_\nu(\nu_c)$, so it is a very good approximation to associate the measured flux density $S_\nu(\nu)$ as the flux density corresponding to the band central frequency ν_c .

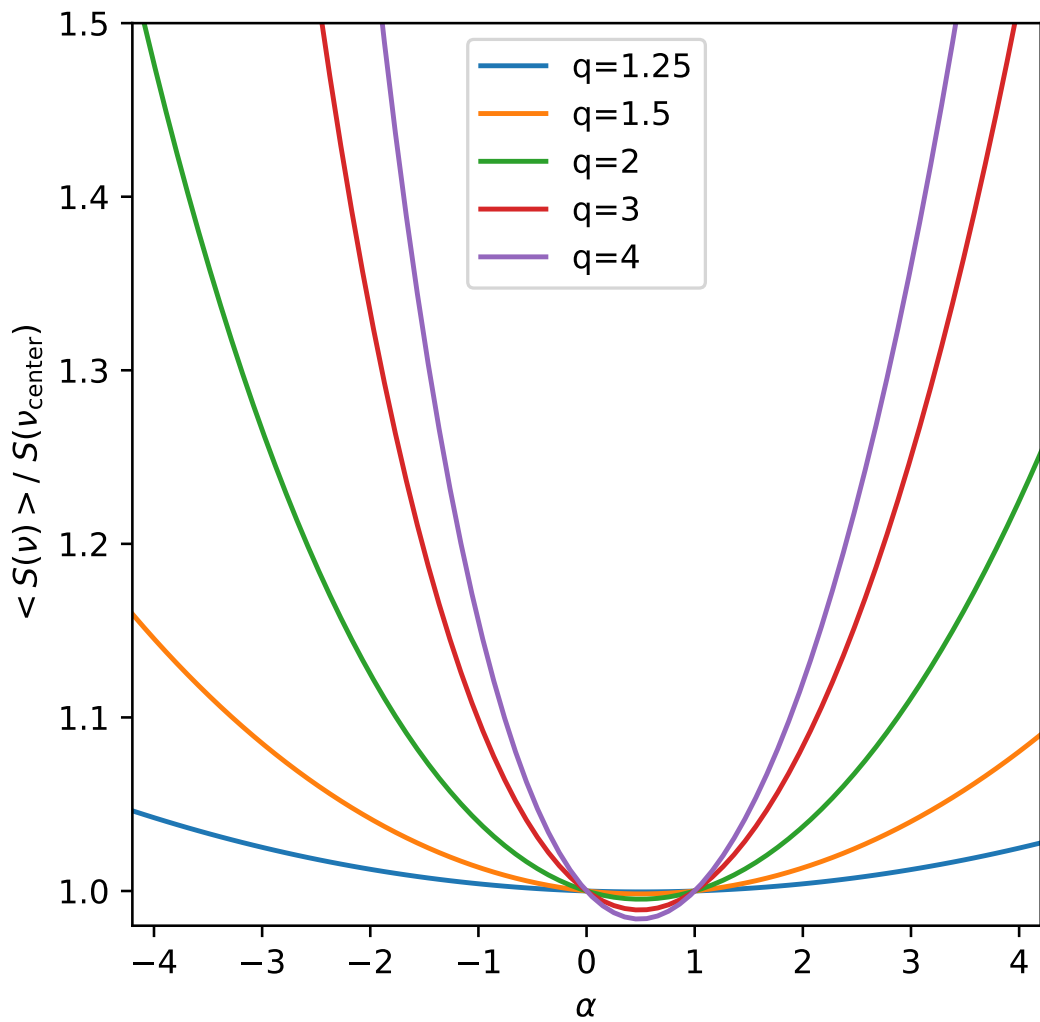


Figure C.1 Ratio of the flux density averaged over the whole frequency coverage of the band (the measured flux density) and the flux density at the center of the band. The flux density is assumed to follow a power law.

LIST OF FIGURES

1.1	NGC 1333 ridge	3
1.2	Outflow and jet scheme	4
1.3	YSO classification	6
1.4	Outflow and jet scheme	8
1.5	Molecular winds	10
1.6	Molecular jets	12
4.1	Spectral setup	19
4.2	SVS 13 outflow	21
4.3	Extended Data Fig. 9: Detection of Bullet 2 with ACA	22
4.4	Figure 1 name	24
4.5	Selection of high resolution channel maps	27
4.6	Selection of high resolution channel maps	28
4.7	Figure 3 name	30
4.8	Observed SO image of Bullet 1	31
5.1	Results of the paraboloidal shell model fitting.	45
5.2	Results of the ballistic deprojection of the observations	50
5.3	Schematic diagram of the thin shell bowshock model	52
5.4	Comparison of the bowshock model results with the elliptical fits to the observations	55
5.5	Velocity as a function of the polar angle for the bowshock model	55
5.6	Comparison of observed and bowshock model spectral channel images	60
5.6	Comparison of the bowshock model with the observed moment images and position-velocity diagrams	63
C.1	Spectral setup	74

LIST OF TABLES

1.1	Young stellar objects with molecular jets.	13
4.1	Compilation of properties of outflow features associated with SVS 13. . . .	38
5.1	Bowshock model parameters for families of Rings II, III, and VI.	59

BIBLIOGRAPHY

- André, P., Di Francesco, J., Ward-Thompson, D., et al. From Filamentary Networks to Dense Cores in Molecular Clouds: Toward a New Paradigm for Star Formation. *Protostars and Planets VI*, 27–51 (2014).
- Andre, P., Ward-Thompson, D., & Barsony, M. From Prestellar Cores to Protostars: the Initial Conditions of Star Formation. *Protostars and Planets IV*, 59 (2000).
- Anglada, G., Rodríguez, L. F., & Carrasco-González, C. Radio jets from young stellar objects. *Astron. Astrophys. Rev.* **26**, 3 (2018).
- Anglada, G., Rodríguez, L. F., & Torrelles, J. M. Discovery of a Subarcsecond Radio Binary Associated with the SVS 13 Star in the HH 7-11 Region. *Astrophys. J. Lett.* **542**, L123 (2000).
- Arce, H. G., Shepherd, D., Gueth, F., et al. Molecular Outflows in Low- and High-Mass Star-forming Regions. *Protostars and Planets V*, 245 (2007).
- Audard, M., Ábrahám, P., Dunham, M. M., et al. Episodic Accretion in Young Stars. *Protostars and Planets VI*, 387–410 (2014).
- Bacciotti, F., Ray, T. P., Mundt, R., Eislöffel, J., & Solf, J. Hubble Space Telescope/STIS Spectroscopy of the Optical Outflow from DG Tauri: Indications for Rotation in the Initial Jet Channel. *Astrophys. J.* **576**, 222 (2002).
- Bachiller, R. Bipolar Molecular Outflows from Young Stars and Protostars. *Ann. Rev. Astron. Astrophys.* **34**, 111 (1996).
- Bachiller, R., Cernicharo, J., Martin-Pintado, J., Tafalla, M., & Lazareff, B. High-velocity molecular bullets in a fast bipolar outflow near L 1448/IRS 3. *Astron. Astrophys.* **231**, 174 (1990).
- Bachiller, R., Gueth, F., Guilloteau, S., Tafalla, M., & Dutrey, A. The origin of the HH 7-11 outflow. *Astron. Astrophys.* **362**, L33 (2000).
- Bally, J. Jets from young stars. *Ap&SS* **311**, 15 (2007).
- Bally, J. Protostellar Outflows. *Ann. Rev. Astron. Astrophys.* **54**, 491 (2016).

- Bally, J., & Lada, C. J. The high-velocity molecular flows near young stellar objects. *Astrophys. J.* **265**, 824 (1983).
- Bate, M. R. Collapse of a Molecular Cloud Core to Stellar Densities: The First Three-dimensional Calculations. *Astrophys. J. Lett.* **508**, L95 (1998).
- Bergin, E. A., & Tafalla, M. Cold Dark Clouds: The Initial Conditions for Star Formation. *Ann. Rev. Astron. Astrophys.* **45**, 339 (2007).
- Bjerkeli, P., van der Wiel, M. H. D., Harsono, D., Ramsey, J. P., & Jørgensen, J. K. Resolved images of a protostellar outflow driven by an extended disk wind. *Nature* **540**, 406 (2016).
- Bjerkeli, P., Ramsey, J. P., Harsono, D., et al. Kinematics around the B335 protostar down to au scales. *Astron. Astrophys.* **631**, A64 (2019).
- Booth, A. S., Tabone, B., Ille, J. D., et al. Molecules with ALMA at Planet-forming Scales (MAPS). XVI. Characterizing the Impact of the Molecular Wind on the Evolution of the HD 163296 System. *Astrophys. J. Suppl.* **257**, 16 (2021).
- Cabrit, S. The accretion-ejection connexion in T Tauri stars: jet models vs. observations. *Star-Disk Interaction in Young Stars*, 203–214 (2007).
- Cabrit, S., Edwards, S., Strom, S. E., & Strom, K. M. Forbidden-Line Emission and Infrared Excesses in T Tauri Stars: Evidence for Accretion-driven Mass Loss? *Astrophys. J.* **354**, 687 (1990).
- Cabrit, S., Raga, A., & Gueth, F. Models of Bipolar Molecular Outflows. *Herbig-Haro Flows and the Birth of Stars*, 163–180 (1997).
- Chen, X., Arce, H. G., Zhang, Q., Launhardt, R., & Henning, T. Rotating Bullets from A Variable Protostar. *Astrophys. J.* **824**, 72 (2016).
- Cheng, Y., Qiu, K., Zhang, Q., et al. Multiline Observations of Molecular Bullets from a High-mass Protostar. *Astrophys. J.* **877**, 112 (2019).
- Chernin, L., Masson, C., Gouveia dal Pino, E. M., & Benz, W. Momentum Transfer by Astrophysical Jets. *Astrophys. J.* **426**, 204 (1994).
- Chevance, M., Krumholz, M. R., McLeod, A. F., et al. The Life and Times of Giant Molecular Clouds. *Protostars and Planets VII*, 1 (2023).
- Ching, T.-C., Lai, S.-P., Zhang, Q., et al. Helical Magnetic Fields in the NGC 1333 IRAS 4A Protostellar Outflows. *Astrophys. J.* **819**, 159 (2016).
- Choi, M., Hodapp, K. W., Hayashi, M., et al. Variability of the NGC 1333 IRAS 4A Outflow: Molecular Hydrogen and Silicon Monoxide Images. *Astrophys. J.* **646**, 1050 (2006).
- Choi, M., Kang, M., & Tatematsu, K. Rotation of the NGC 1333 IRAS 4A2 Protostellar Jet. *Astrophys. J. Lett.* **728**, L34 (2011).

- Choi, M., Tatematsu, K., & Kang, M. Kinematics of the Ammonia Disk Around the Protostar NGC 1333 IRAS 4A2. *Astrophys. J. Lett.* **723**, L34 (2010).
- Codella, C., Maury, A. J., Gueth, F., et al. First results from the CALYPSO IRAM-PdBI survey. III. Monopolar jets driven by a proto-binary system in NGC 1333-IRAS2A. *Astron. Astrophys.* **563**, L3 (2014).
- Codella, C., Cabrit, S., Gueth, F., et al. The ALMA view of the protostellar system HH212. The wind, the cavity, and the disk. *Astron. Astrophys.* **568**, L5 (2014).
- Coffey, D., Bacciotti, F., Ray, T. P., Eisloffel, J., & Woitas, J. Further Indications of Jet Rotation in New Ultraviolet and Optical Hubble Space Telescope STIS Spectra. *Astrophys. J.* **663**, 350 (2007).
- Coffey, D., Rigliaco, E., Bacciotti, F., Ray, T. P., & Eisloffel, J. Jet Rotation Investigated in the Near-ultraviolet with the Hubble Space Telescope Imaging Spectrograph. *Astrophys. J.* **749**, 139 (2012).
- Cudworth, K. M., & Herbig, G. Two large-proper-motion Herbig-Haro objects. *Astron. J.* **84**, 548 (1979).
- de A. Schutzer, A., Rivera-Ortiz, P. R., Lefloch, B., et al. SOLIS. XVI. Mass ejection and time variability in protostellar outflows: Cep E. *Astron. Astrophys.* **662**, A104 (2022).
- de Valon, A., Dougados, C., Cabrit, S., et al. ALMA reveals a large structured disk and nested rotating outflows in DG Tauri B. *Astron. Astrophys.* **634**, L12 (2020).
- de Valon, A., Dougados, C., Cabrit, S., et al. Modeling the CO outflow in DG Tauri B: Swept-up shells versus perturbed MHD disk wind. *Astron. Astrophys.* **668**, A78 (2022).
- Díaz Rodríguez, A. K. (2021), PhD thesis, Institute of Astrophysics of Andalusia.
- Díaz-Rodríguez, A. K., Anglada, G., Blázquez-Calero, G., et al. The Physical Properties of the SVS 13 Protobinary System: Two Circumstellar Disks and a Spiraling Circumbinary Disk in the Making. *Astrophys. J.* **930**, 91 (2022).
- Dobbs, C. L., Krumholz, M. R., Ballesteros-Paredes, J., et al. Formation of Molecular Clouds and Global Conditions for Star Formation. *Protostars and Planets VI*, 3–26 (2014).
- Downes, T. P., & Cabrit, S. Jet-driven molecular outflows from class 0 sources: younger and stronger than they seem? *Astron. Astrophys.* **471**, 873 (2007).
- Downes, T. P., & Ray, T. P. On the transfer of momentum from stellar jets to molecular outflows. *Astron. Astrophys.* **345**, 977 (1999).
- Dunham, M. M., Stutz, A. M., Allen, L. E., et al. The Evolution of Protostars: Insights from Ten Years of Infrared Surveys with Spitzer and Herschel. *Protostars and Planets VI*, 195–218 (2014).

- Dutta, S., Lee, C.-F., Johnstone, D., et al. Episodic Accretion in Protostars – An ALMA Survey of Molecular Jets in the Orion Molecular Cloud. *arXiv e-prints* arXiv:2306.15346 (2023).
- Eisloffel, J., & Mundt, R. Parsec-Scale Jets From Young Stars. *Astron. J.* **114**, 280 (1997).
- Ellerbroek, L. E., Podio, L., Kaper, L., et al. The outflow history of two Herbig-Haro jets in RCW 36: HH 1042 and HH 1043. *Astron. Astrophys.* **551**, A5 (2013).
- Erkal, J., Dougados, C., Coffey, D., et al. Launching the asymmetric bipolar jet of DO Tau. *Astron. Astrophys.* **650**, A46 (2021).
- Estalella, R., & Anglada, G. (2008), Introducción a la física del medio (Publicacions i Edicions de la Universitat de Barcelona).
- Fischer, W. J., Hillenbrand, L. A., Herczeg, G. J., et al. Accretion Variability as a Guide to Stellar Mass Assembly. *Protostars and Planets VII*, 355 (2023).
- Frank, A., Ray, T. P., Cabrit, S., et al. Jets and Outflows from Star to Cloud: Observations Confront Theory. *Protostars and Planets VI*, 451–474 (2014).
- Frerking, M. A., Langer, W. D., & Wilson, R. W. The relationship between carbon monoxide abundance and visual extinction in interstellar clouds. *Astrophys. J.* **262**, 590 (1982).
- Gaia Collaboration, Vallenari, A., Brown, A. G. A., et al. Gaia Data Release 3. Summary of the content and survey properties. *Astron. Astrophys.* **674**, A1 (2023).
- Garufi, A., Podio, L., Codella, C., et al. ALMA chemical survey of disk-outflow sources in Taurus (ALMA-DOT). I. CO, CS, CN, and H₂CO around DG Tau B. *Astron. Astrophys.* **636**, A65 (2020).
- Gómez, G. C., & Vázquez-Semadeni, E. Filaments in Simulations of Molecular Cloud Formation. *Astrophys. J.* **791**, 124 (2014).
- Gómez-Ruiz, A. I., Codella, C., Lefloch, B., et al. The density structure of the L1157 molecular outflow. *MNRAS* **446**, 3346 (2015).
- Gueth, F., & Guilloteau, S. The jet-driven molecular outflow of HH 211. *Astron. Astrophys.* **343**, 571 (1999).
- Hacar, A., Clark, S. E., Heitsch, F., et al. Initial Conditions for Star Formation: a Physical Description of the Filamentary ISM. *Protostars and Planets VII*, 153 (2023).
- Hacar, A., Tafalla, M., & Alves, J. Fibers in the NGC 1333 proto-cluster. *Astron. Astrophys.* **606**, A123 (2017).
- Hara, C., Kawabe, R., Nakamura, F., et al. Misaligned Twin Molecular Outflows from the Class 0 Protostellar Binary System VLA 1623A Unveiled by ALMA. *Astrophys. J.* **912**, 34 (2021).

- Haro, G. Herbig's Nebulous Objects Near NGC 1999. *Astrophys. J.* **115**, 572 (1952).
- Hartigan, P., Edwards, S., & Ghandour, L. Disk Accretion and Mass Loss from Young Stars. *Astrophys. J.* **452**, 736 (1995).
- Hartigan, P., Holcomb, R., & Frank, A. Proper Motions and Shock Wave Dynamics in the HH 7-11 Stellar Jet. *Astrophys. J.* **876**, 147 (2019).
- Hartigan, P., Morse, J. A., & Raymond, J. Mass-Loss Rates, Ionization Fractions, Shock Velocities, and Magnetic Fields of Stellar Jets. *Astrophys. J.* **436**, 125 (1994).
- Hartmann, L., Herczeg, G., & Calvet, N. Accretion onto Pre-Main-Sequence Stars. *Ann. Rev. Astron. Astrophys.* **54**, 135 (2016).
- Hatchell, J., Fuller, G. A., & Ladd, E. F. Hot molecular bullets in HH 111 and CEP E. *Astron. Astrophys.* **346**, 278 (1999).
- Hennebelle, P., & Falgarone, E. Turbulent molecular clouds. *Astron. Astrophys. Rev.* **20**, 55 (2012).
- Herbig, G. H. The Spectra of Two Nebulous Objects Near NGC 1999. *Astrophys. J.* **113**, 697 (1951).
- Herbig, G. H. Emission-line Stars in Galactic Nebulosities. *JRASC* **46**, 222 (1952).
- Herbig, G. H. The light variations of the nuclei in Herbig-Haro object No. 2, 1946-1968. *Communications of the Konkoly Observatory Hungary* **65**, 75 (1969).
- Herbig, G. H., & Jones, B. F. Large proper motions of the Herbig-Haro objects HH 1 and HH 2. *Astron. J.* **86**, 1232 (1981).
- Hirano, N., Ho, P. P. T., Liu, S.-Y., et al. Extreme Active Molecular Jets in L1448C. *Astrophys. J.* **717**, 58 (2010).
- Hirano, N., Liu, S.-Y., Shang, H., et al. SiO J = 5-4 in the HH 211 Protostellar Jet Imaged with the Submillimeter Array. *Astrophys. J. Lett.* **636**, L141 (2006).
- Hirota, T., Machida, M. N., Matsushita, Y., et al. Disk-driven rotating bipolar outflow in Orion Source I. *Nature Astronomy* **1**, 0146 (2017).
- Hodapp, K. W., & Chini, R. The Launch Region of the SVS 13 Outflow and Jet. *Astrophys. J.* **794**, 169 (2014).
- Hollenbach, D. The Physics of Molecular Shocks in YSO Outflows. *Herbig-Haro Flows and the Birth of Stars*, 181–198 (1997).
- Hull, C. L. H., Girart, J. M., Kristensen, L. E., et al. An Extremely High Velocity Molecular Jet Surrounded by an Ionized Cavity in the Protostellar Source Serpens SMM1. *Astrophys. J. Lett.* **823**, L27 (2016).

- Hull, C. L. H., Girart, J. M., Tychoniec, Ł., et al. ALMA Observations of Dust Polarization and Molecular Line Emission from the Class 0 Protostellar Source Serpens SMM1. *Astrophys. J.* **847**, 92 (2017).
- James, T. A., Viti, S., Holdship, J., & Jiménez-Serra, I. Tracing shock type with chemical diagnostics. An application to L1157. *Astron. Astrophys.* **634**, A17 (2020).
- Jeans, J. H. The Stability of a Spherical Nebula. *Philosophical Transactions of the Royal Society of London Series A* **199**, 1 (1902).
- Jhan, K.-S., & Lee, C.-F. A Multi-epoch SMA Study of the HH 211 Protostellar Jet: Jet Motion and Knot Formation. *Astrophys. J.* **816**, 32 (2016).
- Jhan, K.-S., & Lee, C.-F. 25 au Angular Resolution Observations of HH 211 with ALMA: Jet Properties and Shock Structures in SiO, CO, and SO. *Astrophys. J.* **909**, 11 (2021).
- Jones, B. F. Proper motions of Herbig-Haro objects. *Revista Mexicana de Astronomia y Astrofisica* **7**, 71 (1983).
- Kauffmann, J., Bertoldi, F., Bourke, T. L., Evans, N. J., I., & Lee, C. W. MAMBO mapping of Spitzer c2d small clouds and cores. *Astron. Astrophys.* **487**, 993 (2008).
- Kwon, W., Fernández-López, M., Stephens, I. W., & Looney, L. W. Kinematics of the Envelope and Two Bipolar Jets in the Class 0 Protostellar System L1157. *Astrophys. J.* **814**, 43 (2015).
- Lada, C. J. Cold outflows, energetic winds, and enigmatic jets around young stellar objects. *Ann. Rev. Astron. Astrophys.* **23**, 267 (1985).
- Lada, C. J., & Fich, M. The Structure and Energetics of a Highly Collimated Bipolar Outflow: NGC 2264G. *Astrophys. J.* **459**, 638 (1996).
- Larson, R. B. Numerical calculations of the dynamics of collapsing proto-star. *MNRAS* **145**, 271 (1969).
- Larson, R. B. The physics of star formation. *Reports on Progress in Physics* **66**, 1651 (2003).
- Launhardt, R., Pavlyuchenkov, Y., Gueth, F., et al. Rotating molecular outflows: the young T Tauri star in CB 26. *Astron. Astrophys.* **494**, 147 (2009).
- Launhardt, R., Pavlyuchenkov, Y. N., Akimkin, V. V., et al. A resolved rotating disk wind from a young T Tauri star in the Bok globule CB 26. *Astron. Astrophys.* **678**, A135 (2023).
- Lee, C.-F. Molecular jets from low-mass young protostellar objects. *Astron. Astrophys. Rev.* **28**, 1 (2020).
- Lee, C.-F., Hasegawa, T. I., Hirano, N., et al. The Reflection-Symmetric Wiggle of the Young Protostellar Jet HH 211. *Astrophys. J.* **713**, 731 (2010).

- Lee, C.-F., Hirano, N., Palau, A., et al. Rotation and Outflow Motions in the Very Low-Mass Class 0 Protostellar System HH 211 at Subarcsecond Resolution. *Astrophys. J.* **699**, 1584 (2009).
- Lee, C.-F., Hirano, N., Zhang, Q., et al. Jet Motion, Internal Working Surfaces, and Nested Shells in the Protostellar System HH 212. *Astrophys. J.* **805**, 186 (2015).
- Lee, C.-F., Ho, P. T. P., Li, Z.-Y., et al. A rotating protostellar jet launched from the innermost disk of HH 212. *Nature Astronomy* **1**, 0152 (2017).
- Lee, C.-F., Li, Z.-Y., Hirano, N., et al. ALMA Observations of the Very Young Class 0 Protostellar System HH211-mms: A 30 au Dusty Disk with a Disk Wind Traced by SO? *Astrophys. J.* **863**, 94 (2018).
- Lee, C.-F., Mundy, L. G., Reipurth, B., Ostriker, E. C., & Stone, J. M. CO Outflows from Young Stars: Confronting the Jet and Wind Models. *Astrophys. J.* **542**, 925 (2000).
- Lee, C.-F., Stone, J. M., Ostriker, E. C., & Mundy, L. G. Hydrodynamic Simulations of Jet- and Wind-driven Protostellar Outflows. *Astrophys. J.* **557**, 429 (2001).
- Lee, C.-F., Tabone, B., Cabrit, S., et al. First Detection of Interaction between a Magnetic Disk Wind and an Episodic Jet in a Protostellar System. *Astrophys. J. Lett.* **907**, L41 (2021).
- Lee, C.-F., Li, Z.-Y., Codella, C., et al. A 100 au Wide Bipolar Rotating Shell Emanating from the HH 212 Protostellar Disk: A Disk Wind? *Astrophys. J.* **856**, 14 (2018).
- Lefèvre, C., Cabrit, S., Maury, A. J., et al. CALYPSO view of SVS 13A with PdBI: Multiple jet sources. *Astron. Astrophys.* **604**, L1 (2017).
- Lefloch, B., Cernicharo, J., Reipurth, B., Pardo, J. R., & Neri, R. Anatomy of HH 111 from CO Observations: A Bow-Shock-driven Molecular Outflow. *Astrophys. J.* **658**, 498 (2007).
- Lefloch, B., Eisloeffel, J., & Lazareff, B. The remarkable Class 0 source CEP E. *Astron. Astrophys.* **313**, L17 (1996).
- Lefloch, B., Gusdorf, A., Codella, C., et al. The structure of the Cepheus E protostellar outflow: The jet, the bowshock, and the cavity. *Astron. Astrophys.* **581**, A4 (2015).
- Leurini, S., Codella, C., Zapata, L. A., et al. Extremely high velocity gas from the massive young stellar objects in IRAS 17233-3606. *Astron. Astrophys.* **507**, 1443 (2009).
- Li, Z.-Y., & Shu, F. H. Interaction of Wide-Angle MHD Winds with Flared Disks. *Astrophys. J.* **468**, 261 (1996).
- López-Vázquez, J. A., Zapata, L. A., & Lee, C.-F. A Disk Wind Driving the Rotating Molecular Outflow in CB 26. *Astrophys. J.* **944**, 63 (2023).
- López-Vázquez, J. A., Zapata, L. A., Lizano, S., & Cantó, J. ALMA Observations and Modeling of the Rotating Outflow in Orion Source I. *Astrophys. J.* **904**, 158 (2020).

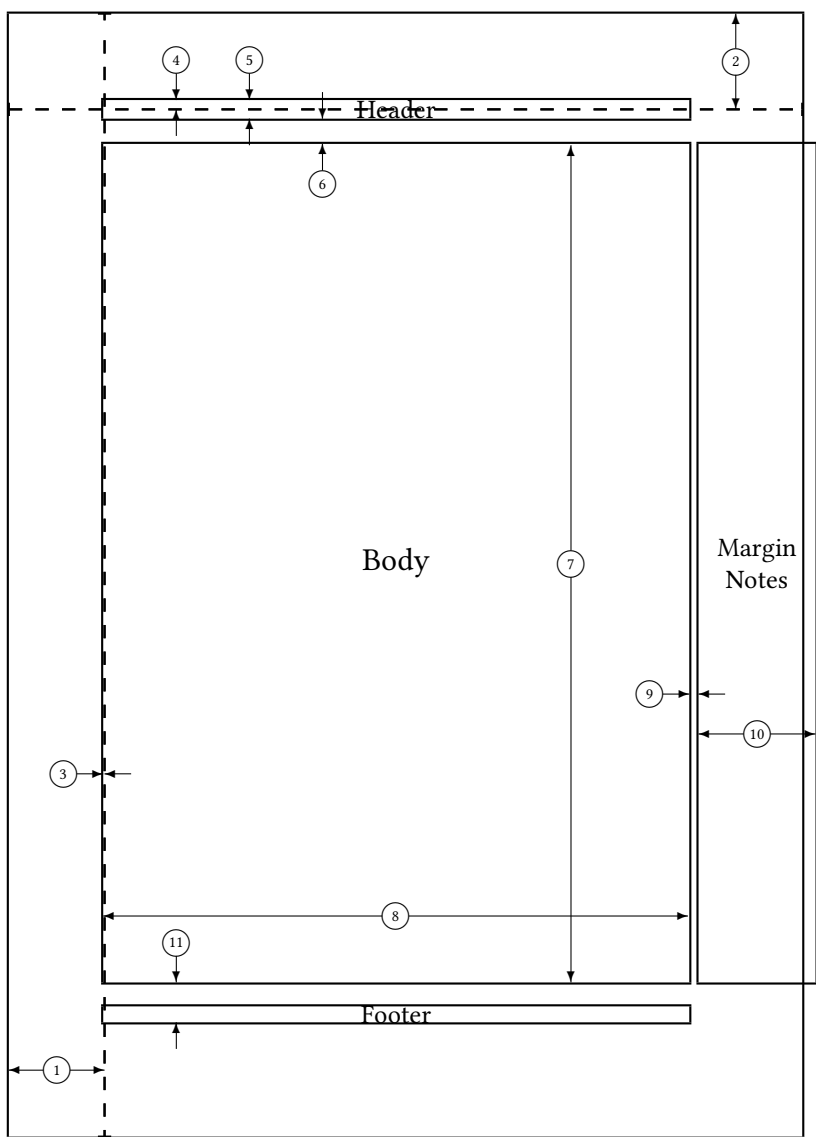
- Louvet, F., Dougados, C., Cabrit, S., et al. The HH30 edge-on T Tauri star. A rotating and precessing monopolar outflow scrutinized by ALMA. *Astron. Astrophys.* **618**, A120 (2018).
- Masson, C. R., & Chernin, L. M. Properties of Jet-driven Molecular Outflows. *Astrophys. J.* **414**, 230 (1993).
- Masson, C. R., Mundy, L. G., & Keene, J. The Extremely High Velocity CO Flow in HH 7–11. *Astrophys. J. Lett.* **357**, L25 (1990).
- Matsushita, Y., Takahashi, S., Ishii, S., et al. Super-fast Rotation in the OMC 2/FIR 6b Jet. *Astrophys. J.* **916**, 23 (2021).
- Matsushita, Y., Takahashi, S., Machida, M. N., & Tomisaka, K. A Very Compact Extremely High Velocity Flow toward MMS 5/OMC-3 Revealed with ALMA. *Astrophys. J.* **871**, 221 (2019).
- Matzner, C. D., & McKee, C. F. Bipolar Molecular Outflows Driven by Hydromagnetic Protostellar Winds. *Astrophys. J. Lett.* **526**, L109 (1999).
- McKee, C. F., & Ostriker, E. C. Theory of Star Formation. *Ann. Rev. Astron. Astrophys.* **45**, 565 (2007).
- Moraghan, A., Lee, C.-F., Huang, P.-S., & Vaidya, B. A study of the wiggle morphology of HH 211 through numerical simulations. *MNRAS* **460**, 1829 (2016).
- Motte, F., Bontemps, S., & Louvet, F. High-Mass Star and Massive Cluster Formation in the Milky Way. *Ann. Rev. Astron. Astrophys.* **56**, 41 (2018).
- Movsessian, T. A., Magakian, T. Y., Amram, P., Boulesteix, J., & Gach, J. L. Scanning Fabry-Pérot observations of the HH 7-11 outflow system. *Astron. Astrophys.* **364**, 293 (2000).
- Mundt, R., & Fried, J. W. Jets from young stars. *Astrophys. J. Lett.* **274**, L83 (1983).
- Natta, A., Testi, L., Alcalá, J. M., et al. X-shooter spectroscopy of young stellar objects. V. Slow winds in T Tauri stars. *Astron. Astrophys.* **569**, A5 (2014).
- Nisini, B., Codella, C., Giannini, T., & Richer, J. S. Observations of high-J SiO emission along the HH211 outflow. *Astron. Astrophys.* **395**, L25 (2002).
- Offner, S. S. R., Clark, P. C., Hennebelle, P., et al. The Origin and Universality of the Stellar Initial Mass Function. *Protostars and Planets VI*, 53–75 (2014).
- Offner, S. S. R., Moe, M., Kratter, K. M., et al. The Origin and Evolution of Multiple Star Systems. *Protostars and Planets VII*, 275 (2023).
- Ortiz-León, G. N., Loinard, L., Dzib, S. A., et al. The Gould’s Belt Distances Survey (GOBELINS). V. Distances and Kinematics of the Perseus Molecular Cloud. *Astrophys. J.* **865**, 73 (2018).

- Osorio, M., Anglada, G., Carrasco-González, C., et al. Imaging the Inner and Outer Gaps of the Pre-transitional Disk of HD 169142 at 7 mm. *Astrophys. J. Lett.* **791**, L36 (2014).
- Osorio, M., Macías, E., Anglada, G., et al. A Dwarf Transitional Protoplanetary Disk around XZ Tau B. *Astrophys. J. Lett.* **825**, L10 (2016).
- Ostriker, E. C., Lee, C.-F., Stone, J. M., & Mundy, L. G. A Ballistic Bow Shock Model for Jet-driven Protostellar Outflow Shells. *Astrophys. J.* **557**, 443 (2001).
- Pascucci, I., Cabrit, S., Edwards, S., et al. The Role of Disk Winds in the Evolution and Dispersal of Protoplanetary Disks. *Protostars and Planets VII*, 567 (2023).
- Pineda, J. E., Arzoumanian, D., Andre, P., et al. From Bubbles and Filaments to Cores and Disks: Gas Gathering and Growth of Structure Leading to the Formation of Stellar Systems. *Protostars and Planets VII*, 233 (2023).
- Plunkett, A. L., Arce, H. G., Corder, S. A., et al. CARMA Observations of Protostellar Outflows in NGC 1333. *Astrophys. J.* **774**, 22 (2013).
- Plunkett, A. L., Arce, H. G., Mardones, D., et al. Episodic molecular outflow in the very young protostellar cluster Serpens South. *Nature* **527**, 70 (2015).
- Podio, L., Tabone, B., Codella, C., et al. The CALYPSO IRAM-PdBI survey of jets from Class 0 protostars. Exploring whether jets are ubiquitous in young stars. *Astron. Astrophys.* **648**, A45 (2021).
- Pudritz, R. E., & Ray, T. P. The Role of Magnetic Fields in Protostellar Outflows and Star Formation. *Frontiers in Astronomy and Space Sciences* **6**, 54 (2019).
- Qiu, K., Wyrowski, F., Menten, K., Zhang, Q., & Güsten, R. CO Multi-line Observations of HH 80-81: A Two-component Molecular Outflow Associated with the Largest Protostellar Jet in Our Galaxy. *Astrophys. J.* **871**, 141 (2019).
- Qiu, K., & Zhang, Q. Discovery of Extremely High Velocity “Molecular Bullets” in the HH 80-81 High-Mass Star-Forming Region. *Astrophys. J. Lett.* **702**, L66 (2009).
- Rabenanahary, M., Cabrit, S., Meliani, Z., & Pineau des Forets, G. Wide-angle protostellar outflows driven by narrow jets in stratified cores. *Astron. Astrophys.* **664**, A118 (2022).
- Raga, A., & Cabrit, S. Molecular outflows entrained by jet bowshocks. *Astron. Astrophys.* **278**, 267 (1993).
- Raga, A. C., Cantó, J., & Rodríguez-González, A. (2021), The physics of the Interstellar Medium (Universidad Nacional Autonoma de Mexico).
- Ray, T. P., & Ferreira, J. Jets from young stars. *New. Astron. Rev.* **93**, 101615 (2021).
- Ray, T. P., McCaughrean, M. J., Caratti o Garatti, A., et al. Outflows from the youngest stars are mostly molecular. *Nature* **622**, 48 (2023).

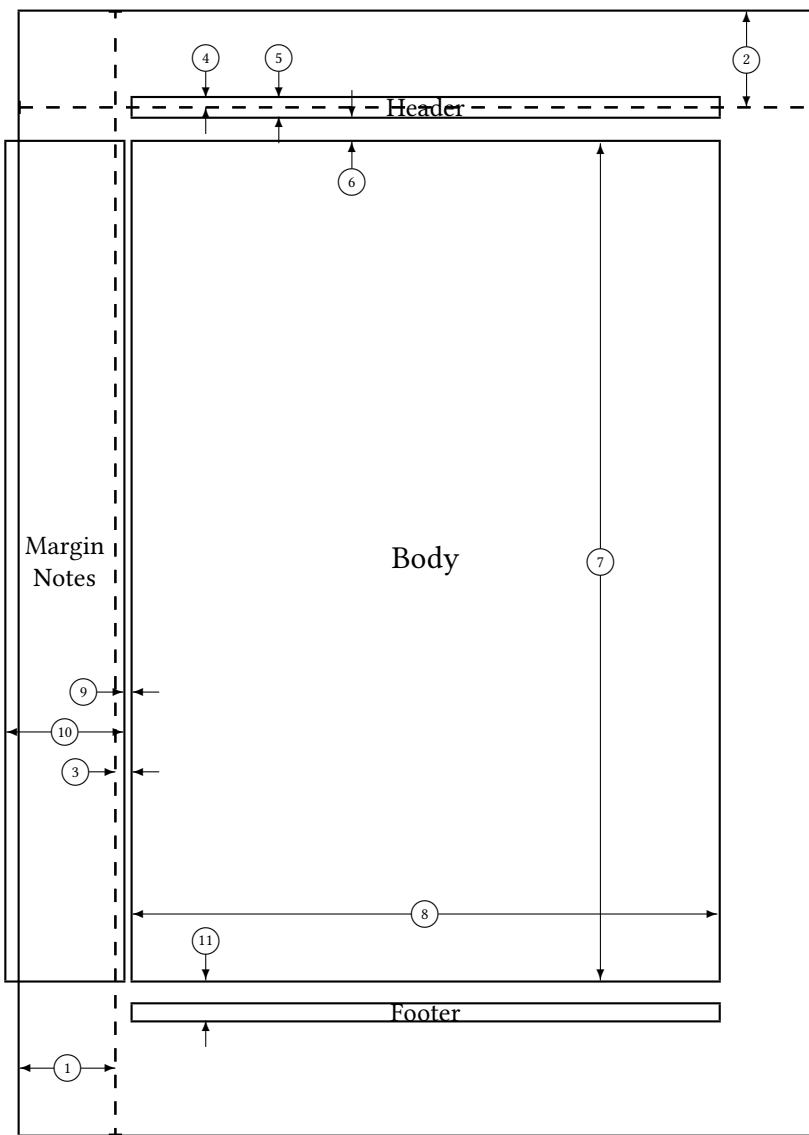
- Reipurth, B., & Bally, J. Herbig-Haro Flows: Probes of Early Stellar Evolution. *Ann. Rev. Astron. Astrophys.* **39**, 403 (2001).
- Reipurth, B., & Heathcote, S. 50 Years of Herbig-Haro Research. From discovery to HST. *Herbig-Haro Flows and the Birth of Stars*, 3–18 (1997).
- Santiago-García, J., Tafalla, M., Johnstone, D., & Bachiller, R. Shells, jets, and internal working surfaces in the molecular outflow from IRAS 04166+2706. *Astron. Astrophys.* **495**, 169 (2009).
- Sato, A., Tokuda, K., Machida, M. N., et al. Secondary outflow driven by the protostar Ser-emb 15 in Serpens. *arXiv e-prints* arXiv:2310.06055 (2023).
- Schulz, N. S. (2012), The Formation and Early Evolution of Stars (Springer), doi: 10.1007/978-3-642-23926-7.
- Schwartz, R. D. T Tauri nebulae and Herbig-Haro nebulae: evidence for excitation by a strong stellar wind. *Astrophys. J.* **195**, 631 (1975).
- Schwartz, R. D. Herbig-haro objects. *Ann. Rev. Astron. Astrophys.* **21**, 209 (1983).
- Shang, H., Allen, A., Li, Z.-Y., et al. A Unified Model for Bipolar Outflows from Young Stars. *Astrophys. J.* **649**, 845 (2006).
- Shang, H., Krasnopolsky, R., Liu, C.-F., & Wang, L.-Y. A Unified Model for Bipolar Outflows from Young Stars: The Interplay of Magnetized Wide-angle Winds and Isothermal Toroids. *Astrophys. J.* **905**, 116 (2020).
- Shang, H., Liu, C.-F., Krasnopolsky, R., & Wang, L.-Y. A Unified Model for Bipolar Outflows from Young Stars: Kinematic Signatures of Jets, Winds, and Their Magnetic Interplay with the Ambient Toroids. *Astrophys. J.* **944**, 230 (2023).
- Shu, F. H., Najita, J. R., Shang, H., & Li, Z. Y. X-Winds Theory and Observations. *Protostars and Planets IV*, 789–814 (2000).
- Shu, F. H., Ruden, S. P., Lada, C. J., & Lizano, S. Star Formation and the Nature of Bipolar Outflows. *Astrophys. J. Lett.* **370**, L31 (1991).
- Smith, M. D., Suttner, G., & Yorke, H. W. Numerical hydrodynamic simulations of jet-driven bipolar outflows. *Astron. Astrophys.* **323**, 223 (1997).
- Snell, R. L., & Edwards, S. High velocity molecular gas near Herbig-Haro objects HH 7-11. *Astrophys. J.* **251**, 103 (1981).
- Snell, R. L., Loren, R. B., & Plambeck, R. L. Observations of CO in L 1551 : evidence for stellar wind driven shocks. *Astrophys. J. Lett.* **239**, L17 (1980).
- Solf, J., & Boehm, K. H. The Velocity Field and Structure of the HH-7–HH-11 Complex. *Astron. J.* **93**, 1172 (1987).

- Steven W. Stahler, Francesco Palla, F. P. (2004), The Formation of Stars (Wiley-VCH).
- Suttner, G., Smith, M. D., Yorke, H. W., & Zinnecker, H. Multi-dimensional numerical simulations of molecular jets. *Astron. Astrophys.* **318**, 595 (1997).
- Tabone, B., Raga, A., Cabrit, S., & Pineau des Forêts, G. Interaction between a pulsating jet and a surrounding disk wind. A hydrodynamical perspective. *Astron. Astrophys.* **614**, A119 (2018).
- Tabone, B., Cabrit, S., Bianchi, E., et al. ALMA discovery of a rotating SO/SO₂ flow in HH212. A possible MHD disk wind? *Astron. Astrophys.* **607**, L6 (2017).
- Tabone, B., Cabrit, S., Pineau des Forêts, G., et al. Constraining MHD disk winds with ALMA. Apparent rotation signatures and application to HH212. *Astron. Astrophys.* **640**, A82 (2020).
- Tafalla, M., Santiago, J., Johnstone, D., & Bachiller, R. A highly collimated, extremely high velocity outflow in Taurus. *Astron. Astrophys.* **423**, L21 (2004).
- Tafalla, M., Santiago-García, J., Hacar, A., & Bachiller, R. A molecular survey of outflow gas: velocity-dependent shock chemistry and the peculiar composition of the EHV gas. *Astron. Astrophys.* **522**, A91 (2010).
- Tafalla, M., Su, Y. N., Shang, H., et al. Anatomy of the internal bow shocks in the IRAS 04166+2706 protostellar jet. *Astron. Astrophys.* **597**, A119 (2017).
- Toledano-Juárez, I., de la Fuente, E., Trinidad, M. A., Tafoya, D., & Nigoche-Netro, A. Collision of molecular outflows in the L1448-C system. *MNRAS* **522**, 1591 (2023).
- Tychoniec, Ł., Hull, C. L. H., Kristensen, L. E., et al. Chemical and kinematic structure of extremely high-velocity molecular jets in the Serpens Main star-forming region. *Astron. Astrophys.* **632**, A101 (2019).
- Vázquez-Semadeni, E., Palau, A., Ballesteros-Paredes, J., Gómez, G. C., & Zamora-Avilés, M. Global hierarchical collapse in molecular clouds. Towards a comprehensive scenario. *MNRAS* **490**, 3061 (2019).
- Wang, L.-Y., Shang, H., & Chiang, T.-Y. Ejection History of the IRAS 04166+2706 Molecular Jet. *Astrophys. J.* **874**, 31 (2019).
- Wang, L.-Y., Shang, H., Su, Y.-N., et al. Molecular Jet of IRAS 04166+2706. *Astrophys. J.* **780**, 49 (2014).
- Williams, J. P., Blitz, L., & McKee, C. F. The Structure and Evolution of Molecular Clouds: from Clumps to Cores to the IMF. *Protostars and Planets IV*, 97 (2000).
- Yen, H.-W., Takakuwa, S., & Ohashi, N. High-Velocity Jets and Slowly Rotating Envelope in B335. *Astrophys. J.* **710**, 1786 (2010).

- Yoon, S.-Y., Herczeg, G. J., Lee, J.-E., et al. Dissecting the Different Components of the Modest Accretion Bursts of the Very Young Protostar HOPS 373. *Astrophys. J.* **929**, 60 (2022).
- Zapata, L. A., Lizano, S., Rodríguez, L. F., et al. Kinematics of the Outflow from the Young Star DG Tau B: Rotation in the Vicinities of an Optical Jet. *Astrophys. J.* **798**, 131 (2015).
- Zhang, Y., Higuchi, A. E., Sakai, N., et al. Rotation in the NGC 1333 IRAS 4C Outflow. *Astrophys. J.* **864**, 76 (2018).



```
1 one inch + \hoffset           2 one inch + \voffset
3 \oddsidemargin = -1pt         4 \topmargin = -7pt
5 \headheight = 14pt            6 \headsep = 19pt
7 \textheight = 631pt           8 \textwidth = 441pt
9 \marginparsep = 7pt           10 \marginparwidth = 88pt
11 \footskip = 30pt             \marginparpush = 7pt (not shown)
\hoffset = 0pt                  \voffset = 0pt
\paperwidth = 597pt             \paperheight = 845pt
```



1 one inch + \hoffset	2 one inch + \voffset
3 \evensidemargin = 13pt	4 \topmargin = -7pt
5 \headheight = 14pt	6 \headsep = 19pt
7 \textheight = 631pt	8 \textwidth = 441pt
9 \marginparsep = 7pt	10 \marginparwidth = 88pt
11 \footskip = 30pt	\marginparpush = 7pt (not shown)
\hoffset = 0pt	\voffset = 0pt
\paperwidth = 597pt	\paperheight = 845pt